Department of Precision and Microsystems Engineering

Design of a novel thermocompression bonding module for high throughput Flex-on-Substrate assembly

Maurits van den Hurk

Report no : 2020.008
Coach : Ing. Sander Dorrestein
Professor : Ir. Jo Spronck
Specialisation : Mechatronic System Design
Type of report : Thesis Report
Date : 20-02-2020

Design of a novel thermocompression bonding module

For high throughput Flex-on-Substrate assembly

Maurits van den Hurk

Faculty of Mechanical, Maritime and Materials Engineering
Department of Precision and Microsystems Engineering
Track Mechatronic System Design

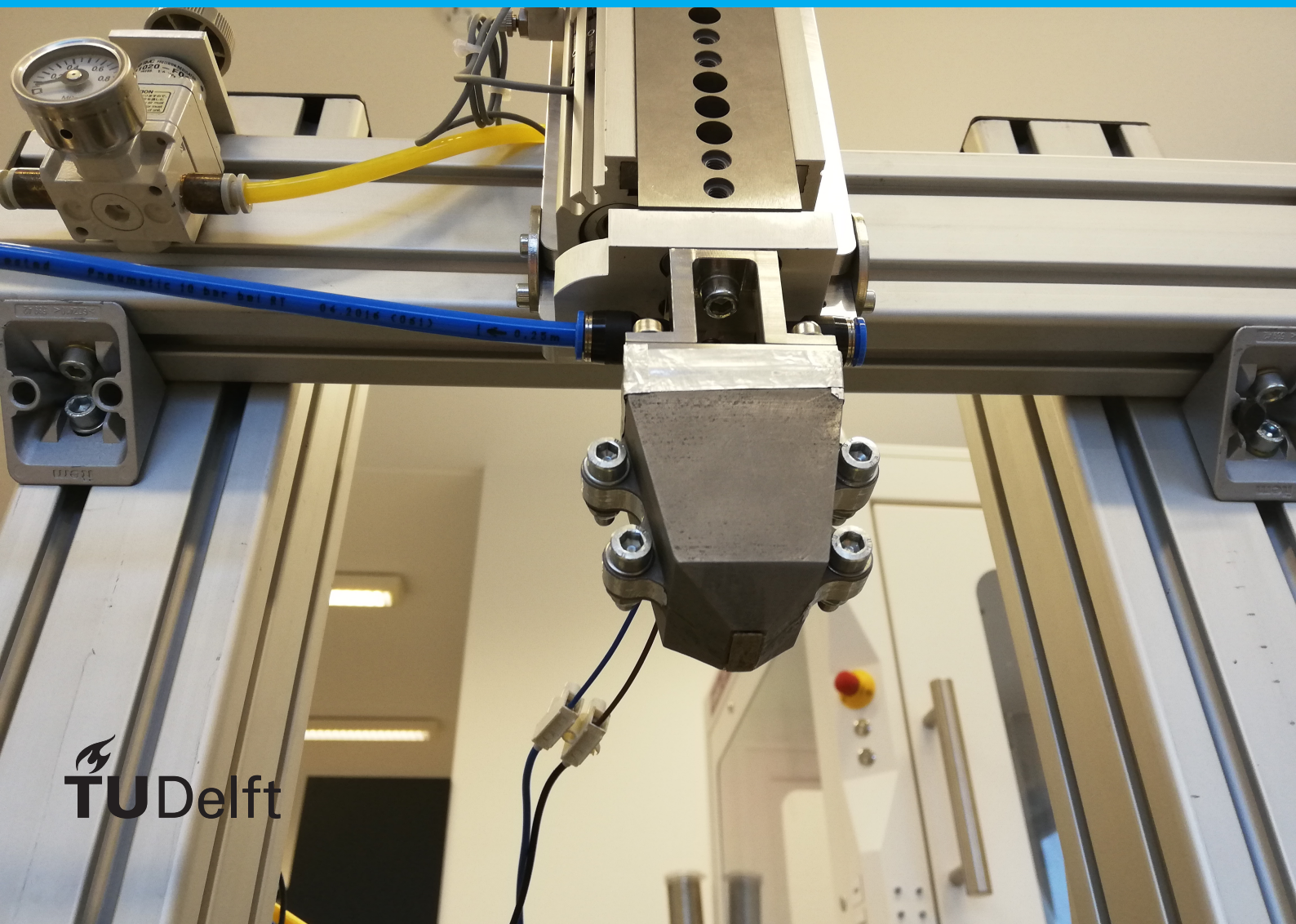

TU Delft

Design of a novel thermocompression bonding module

For high throughput Flex-on-Substrate assembly

by

Maurits van den Hurk

to obtain the degree of Master of Science
at the Delft University of Technology,
to be defended publicly on Thursday February 20, 2020 at 1:45 PM.

Student number: 4304764
Project duration: February 12, 2019 – February 20, 2020
Thesis committee:

Ir. J.W. Spronck,	TU Delft, supervisor
Dr. Ir. M. Langelaar,	TU Delft
Ir. J.P.A. Nijssen, phD,	TU Delft
Ing. S. Dorrestein,	TEGEMA Eindhoven BV

TU Delft

Abstract

Flex-on-substrate assembly is an increasingly popular electronics assembly type that is based on thermocompression bonding: a combination of high temperature and pressure. Currently, up to two-thirds of the cycle time is spent on heating and cooling. To meet the growing demand for flex-on-substrate production in the future, the heating and cooling steps must be more time-efficient. In this thesis, a bonding module is designed that is heated and cooled by using a 150W halogen lamp as a heating source and a staggered-tube heat exchanger with forced airflow as a cooling system (figure 1). The design requires understanding of the bonding process and models containing the governing physics. Therefore, finite element models were made for both heating and cooling which were validated by manufacturing a demonstrator and applying a typical thermocompression bonding temperature profile to the heating element. From the experiment it follows that the concept shows potential for further product development but does not yet perform as required. The reflector surface reflectance,which has an important impact on the energy efficiency, was too low in this demonstrator. Furthermore heat leaks away from the heating element which inhibits a fast temperature rise and the complex cooling system geometry leads to manufacturing errors, which cause leaks in the cooling channel. By improving the design on these points, this concept can decrease the current cycle time by more than 50% and keep up with the growing demand for flex-on-substrate assemblies.

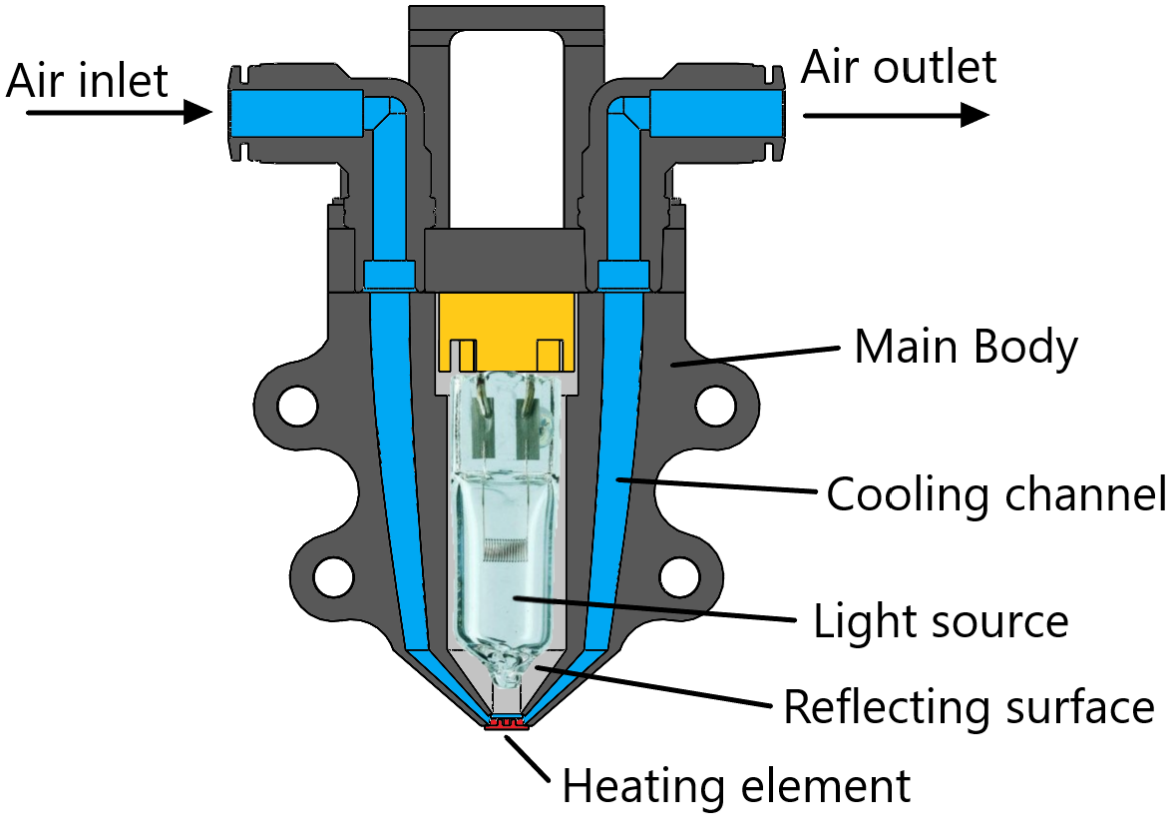

Figure 1: Cross-sectional view of the thermocompression bonding module.

Preface

The subject of this thesis came forth from my interest in designing high-tech machinery and in doing so for an engineering company in Eindhoven. Working for an engineering company has given me the opportunity to become acquainted with the high-tech industry and its way of working and it adds some aspects to the thesis goal. Not only are the university committee members interested in the academic work I deliver, but also TEGEMA would like to know how they can use this work to develop a commercially viable product.

The structure of this project was chosen the same as the other projects at TEGEMA, using a V-model. This is the standard way of working almost everywhere in Eindhoven. For me, it is also an adequate way to check whether I completed all the steps necessary for developing a machine. Working on this module from definition phase up until acceptance phase has been a big motivation.

During the past year I have learned a lot about various subjects: project management, cooperation with different personalities, electronic circuit design and assembly, joining and bonding technologies and many more. This would not have been possible without the great opportunity and freedom that TEGEMA provided me to fulfill this thesis, as well as the materials to build and test the demonstrator.

The difficulties in this project were especially in predicting which parties will influence my planning by how much (for instance adhesive supplier, manufacturing companies), making sure that every square inch of the design is critically reviewed, also every seemingly unimportant one, and estimating the feasibility of key performance requirements. I am satisfied with what I have achieved in the past year, even though my design did not fulfill all requirements. I am glad that I learned these important lessons in this project, so that I will be better prepared in my future career as an engineer.

Furthermore, my appreciation goes out to my supervisors Jo and Sander for their supervision and to everyone who proof-read my report and gave me a advice in numerous different aspects.

Contents

List of abbreviations

ACA ..... Anisotropic Conductive Adhesive

ACF ..... Anisotropic Conductive Film

ACA ..... Anisotropic Conductive Paste

DAI ..... Direct Area Integration

EDM ..... Electric Discharge Machining

FEA ..... Finite Element Analysis

FOS ..... Flex-on-Substrate

FPC ..... Flexible Printed Circuit

FR ..... Functional Requirement

FRS ..... Functional Requirement Specification

IC ..... Integrated Circuit

NIR ..... Near-Infrared Range

PCB ..... Printed Circuit Board

1 Introduction

With the increasing demand for thinner electronics, the use of mechanical connectors becomes more and more inconvenient. A solution that has been investigated and used since the start of the century is flex-on-substrate (FOS) bonding [1]. This is an electrically conductive mechanical bond using solder or adhesive that connects a flexible printed circuit (FPC) with a rigid substrate (e.g. printed circuit board (PCB) or glass). FOS assemblies eliminate the need for connectors and wiring, allowing the total electronic package to become thinner [1]. An example of a flex-on-substrate assembly can be seen in figure 1.1.

The three most important process parameters in FOS bonding are heat, pressure and time: heat to activate the bonding process, pressure to ensure a mechanically and electrically reliable connection, and time to allow the bond to be created [2–4]. One parameter can be reduced by increasing another and for every process parameter there are reasons to reduce them: heat and pressure can be harmful to the electronics and more process time means higher production cost [5, 6]. The ideal set of process parameters is thus one that maximizes heat and pressure up to a point where the output quality is still up to industrial standards and the time is thereby minimized to assure lowest production cost [7].

The bonding method that is best suited for high heat and pressure, while also being compatible with various bonding materials, is thermocompression bonding, see appendix A. In thermocompression bonding, a heating element called a thermode is pressed down against the FOS assembly and is then heated to the process temperature. After completion of the bond formation, the heating system is shut off to let the thermode cool down, after which it can be retracted from the assembly. The process can thus be split up in heating, constant temperature and cooling steps. The constant temperature step is not limited by the bonding machine, as long as it can obtain the required process temperature. The heating and cooling phases, however, are for a large part dependent on the machine performance [6].

A typical application for FOS assemblies is LCD displays, of which smartphone screens are one example [4]. The smartphone industry alone reports a production volume of 1.4 billion units worldwide in the year 2018, equal to 160,000 units per hour [8]. While the demand is high and ever increasing, up to two thirds of the cycle time is spent on heating and cooling of the bonding machine, even though the actual bond formation is the most relevant part of the process [6]. The research goal of this thesis is thus to develop a bonding module that can assemble an FOS assembly with less heating and cooling time, without compromising the mechanical and electrical quality of the joint.

Apart from the industrial value of potentially increasing the throughput of FOS assembly lines, this thesis also has academic relevance. A machine that can heat and cool at faster rates than the currently available machines opens doors for investigating the effect of different rates on the joint quality; currently available literature is mostly focused on low rates compared to industrial standards [7, 9, 10]. While researchers are looking for the highest posible joint quality, this goal conflicts with the industrial need for fast assembly machines that deliver a satisfactory quality level, which is not necessarily the highest possible quality level.

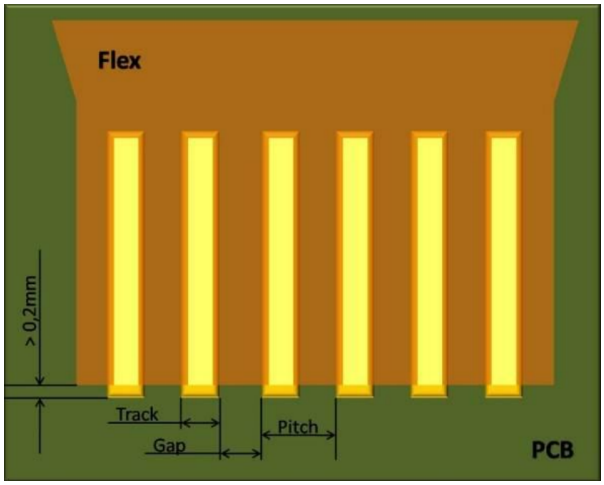

Figure 1.1: Illustration of a flex-on-substrate assembly, in this case flex-on-pcb, provided by Amada Miyachi [11]. The comb layout is common in FOS assemblies, where the electrodes are referred to as tracks.

1.1. Project scope

The development of the novel bonding module in this thesis will focus specifically on the thermoregulatory part of the module, i.e. the heating and cooling systems and the transfer of heat to the FOS assembly. Whilst keeping alignment and the application of pressure in mind, they are not focused on in this thesis.

The thesis is considered successful if the proposed concept for the thermoregulatory system shows potential for improving the FOS bonding machinery state of the art. This is qualified by developing physical models and testing a proof-of-concept demonstrator. The demonstrator should either fulfill the requirements or the limitations must be identified and solvable.

1.2. Thesis structure

This thesis is structured according to the TEGEMA way of working, which uses a V-model, see figure 1.2. This starts with a definition phase, which is discussed in chapter 2. This chapter includes a more detailed discussion of the physics and state-of-the-art of thermocompression bonding, followed by a user requirement specification and functional requirement specification. The next chapter, chapter 3, discusses the architecture phase, where concepts are generated with a morphological chart, out of which one concept is chosen that is worked out in detail in chapter 4, which corresponds to the engineering phase. This chapter includes theoretical models of the heating and cooling processes of the bonding module and FOS assembly. The experimental methods are discussed in chapter 5, which covers the realization and installation phases. The results of the experiments are presented and discussed in chapter 6, the operation phase, and finally, a comprehensive conclusion is drawn in chapter 7 addressing the research goal and other observations, accompanied by a series of recommendations for further work. This is the acceptance phase, completing the v-model trajectory.

1.3. Corporate profile TEGEMA

This thesis is supported by TEGEMA Eindhoven BV in knowledge, materials and financing. TEGEMA is an engineering company in the Brainport region, that focuses on system integration in the field of customised precision mechanics and mechatronics, with the end goal of improving the client's production performance. TEGEMA want to use their expert knowledge on joining and bonding to develop a high-throughput bonding module for their newly developed configurable machine platform that they can use in various applications, one of which is Flex-on-Substrate bonding. This thesis will be the basis for this module.

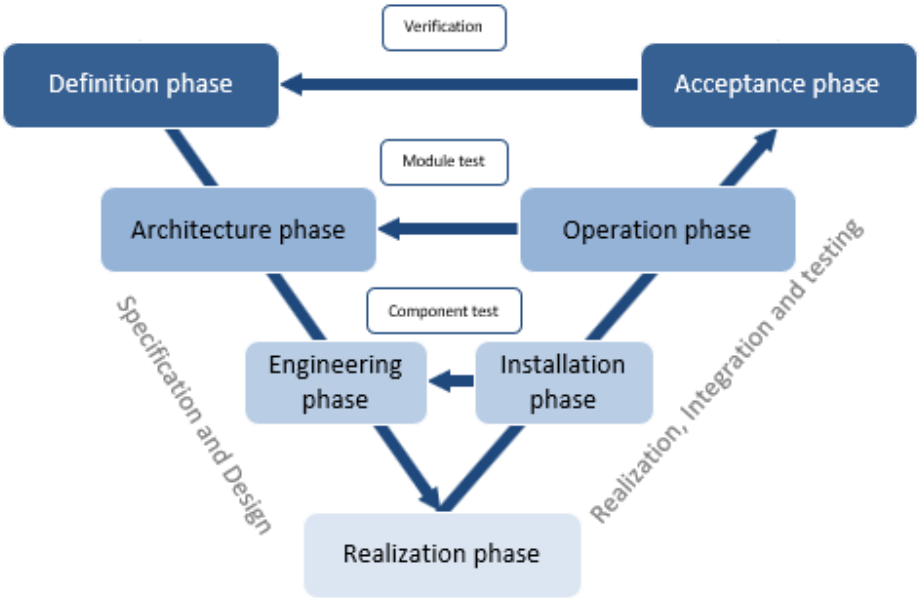

Figure 1.2: V-model describing the thesis structure. Chapter 2 corresponds to the definition phase, chapter 3 corresponds to the architecture phase, chapter 4 cover the design phase, chapter 5 the realization and installation phase, chapter 6 the operation phase and lastly, chapter 7 concludes the V-model with the acceptance phase.

2

Project Definition

In this chapter, the physics behind solder bonding and anisotropic conductive adhesive bonding are discussed in more detail, with special focus on the influence of heating and cooling rate on the quality. A short state-of-the-art overview is given, on which user requirements and functional requirements can be based. The results of this chapter form the starting point for the architecture phase, chapter 3.

2.1. Bonding process

To design a thermocompression bonding module, it is important to understand the bonding processes. As mentioned in the project scope in section 1.1, this module must be able to create solder bonds and anisotropic conductive adhesive bonds. In this section, both bonding methods are discussed in detail, as well as the possibilities and limitations for improving the heating and cooling rates.

2.1.1. Solder bonding

Solder bonding is a well-known method of creating an electrically conductive mechanical connection, which uses an alloy that is molten between the contact points and then solidified. The result is a strong metal connection with high electrical conductivity. The solder is usually applied to the electrode in the form of solder paste, which also contains solder flux. This is a substance that removes oxide layers from the electrode, prevents further oxidation and improves wetting of the solder, the most important condition for a proper solder joint [12]. The two main downsides of solder bonding are the high process temperature and the pitch limitations due to the deposition method [13, 14]. The process temperature depends on the liquidus temperature of the solder alloy, the temperature above which all components become liquid. This is around 180 °C for tin-rich alloys, so the process temperature is generally chosen between 220 and 280 °C [11]. Electrical components tend to be vulnerable to such high temperatures, which poses limitations for the integrated circuit design and material selection. Solder is deposited onto the electrode by stencil printing. The stencil is a metal plate with a cut out pattern through which the solder is dispensed [15]. The manufacturing and dispensing tolerance are two limitations for the pitch, but when the pitch becomes smaller, solder balls also tend to form a bridge between adjacent electrodes, causing a short circuit [13]. Since information density increases over time, pitch size will decrease and there might be a physical limit for the application of solder [16].

Solder bonding starts with a pre-heating step. This raises the temperature to around 100 °C – 150 °C, where the flux is activated [10]. This takes a few seconds, after which the temperature is increased to the maximum process temperature. Finally the joint is cooled down below the solidus temperature, where all components of the solder alloy are solid again and a strong solder joint is formed [11].

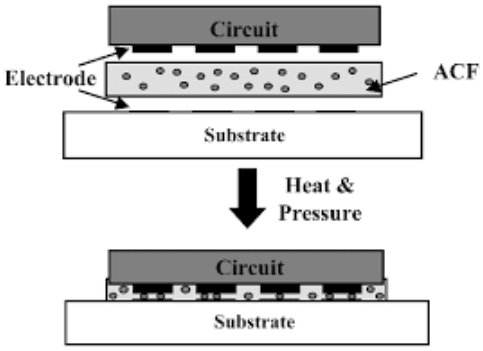

Figure 2.1: Illustration of anisotropic conductive adhesive and its thermocompression bonding process [17]. ACF stands for Anisotropic Conductive Film, which is a type of ACA (Anisotropic Conductive Adhesive)

2.1.2. Anisotropic conductive adhesive bonding

A bonding type that is better suitable for small pitch is adhesive bonding, more specifically anisotropic conductive adhesive (ACA). This is an adhesive with small conductive particles that are trapped between two opposite contact points, see figure 2.1. If the particles are small enough, they will not touch each other and therefore electricity is only conducted between the two opposite contact points [4, 18]. ACAs appear in two forms, film (ACF) and paste (ACP), and two types of polymer, thermosetting and thermoplastic polymers. Thermosetting adhesives (thermosets) are cured by an exothermic reaction that forms 3D networks of polymer chains [19, 20]. Thermoplastic adhesives (thermoplastics) are simply melted and solidified in the desired shape. This is a reversible process, contrary to thermoset curing, which makes it reworkable: if the connection breaks, it can be melted and reattached. This also limits the maximum operating temperature to below this melting temperature. Thermosets generally have a higher maximum operating temperature, since the curing process is irreversible and the thermoset will remain solid at higher temperature. For this reason, thermosets are more common in electronically conductive adhesives than thermoplastics [21].

Thermoset curing is initiated when the temperature passes the so-called 'glass transition temperature'. This is the average of the temperature range in which the material properties start to change, which is generally between 100 and 130 °C [18, 22, 23]. When the glass transition temperature is crossed, the adhesive turns into a rubbery material. The temperature is increased to well above the glass transition temperature, around 150 to 200 °C, to fully cure [7, 18, 23, 24]. When the degree of cure is about 90%, the curing is terminated since further curing makes the joint brittle [25]. Now the adhesive is still above the glass transition temperature and has a rubbery texture, which would mean that the particles can push the adhesive apart if pressure is released. This is unwanted since the contact area of the conductive particles should be as high as possible. This is made sure of by cooling below the glass transition temperature while still maintaining pressure, so that the adhesive turns into a glassy polymer that is rigid enough to maintain the conductive particles in a flat shape [26].

	Solder	**ACA**
Heating	Oxidation can be reduced, but thermal shock leads to cracks in solder joint [12, 27].	Higher coefficient of thermal expansion, lower Young's modulus and T_g [7], increased void formation [28].
Cooling	Finer microstructure, higher microhardness and tensile strength [10, 29–31].	T_g decreases by approximately 2 °C per decade [32].

Table 2.1: Effect of higher heating and cooling rates on solder and ACA bond quality

2.1.3. Temperature rate of change

Both solder bonding and adhesive curing processes can be divided into material-limited steps and machine-limited steps. For solder bonding, material-limited steps are the flux activation and solder melting. For adhesive curing the material-limited step is the curing. No feature of the bonding machine can be improved to speed up these steps, because they fully depending on the bonding material properties. However, the heating and cooling steps can be sped up with a more potent bonding machine. Opinions are divided on whether faster heating and cooling is beneficial for resulting joint, mainly between researchers looking at the actual joint quality and industrial developers considering the package level consequences [5–7, 10, 27–34].

In table 2.1, an overview is given of the influence of faster heating or cooling on solder and ACA joint quality. It can be seen that only for solder cooling, researchers see a better result upon increase. This is reported to be caused by a finer microstructure which results in higher microhardness and tensile strength, making it better resistant to mechanical shock [10, 29–31]. On the other hand, faster cooling does not positively influence ACA joint mechanical properties. Instead, the glass transition temperature (T_g) decreases by 2 °C per 10 °C/s increase in cooling [32]. A lower T_g means that the joint loses mechanical strength at lower temperature. Fast heating is thought to be harmful to both solder bonding and ACA bonding. In solder bonding this is mainly because of thermal shock, an effect associated with the large temperature gradient within the solder, which leads to high internal stresses and ultimately cracks in the solder joint [12]. On the other hand, fast heating gives the solder less opportunity to oxidize, which is beneficial for the joint quality [27]. In ACA bonding, faster heating leads to a higher coefficient of thermal expansion, lower stiffness and again a lower T_g, as well as stimulating void formation due to the decreased mobility of the adhesive [7, 28].

R&D departments of companies involved in thermocompression bonding have also published research papers on the effects of faster heating and cooling [5, 6, 33, 34]. The focus of their research is different in that they consider the specific application of thermocompression bonding for high throughput and they focus on the process-wide influence, rather than the material consequences [5, 34]. For instance, it is reported that faster heating and cooling is a requirement in stacked-die assemblies, using the high temperature gradient to prevent heat from propagating towards lower stacks and unintentionally reflowing earlier completed bonds [33]. The same is valid for heat penetrating the substrate in the case of FOS assembly, which might contain other electronic components that should not be exposed to high temperature [5]. This means that even though faster heating and cooling is not necessarily beneficial for the joint quality, other advantages may be more important and a compromise can be made between joint quality and the other advantages like cycle time and peripheral thermal damage.

2.1.4. State of the Art

Six companies have been selected as a representation of the state of the art of thermocompression bondings machines: Amada Miyachi, Nordson DIMA, Kulicke & Soffa, ASM Amicra, BESI Datacon and Toddco [5, 34–40]. The available performance numbers are bundled in table 2.2.

Company	Heating rate	Cooling rate
Amada Miyachi [35]	200 °C/s	-
ASM Amicra [5, 36]	100 °C/s	50 °C/s
BESI Datacon [37]	200 °C/s	100 °C/s
Kulicke & Soffa [34, 38]	350 °C/s	100 °C/s
Nordson DIMA [39]	200 °C/s	-
Toddco [40]	150 °C/s	-

Table 2.2: Overview of market leading thermocompression bonding machine developers with maximum heating and cooling rates if available.

Kulicke & Soffa offer the fastest heating thermocompression bonder, at 350 °C/s [34, 38]. The other companies offer more similar heating rates between 100 and 200°C/s. It makes sense that K&S is also the company with the highest amount of research papers published, although none of them shed any light on the techniques they use to achieve such a high heating rate, except that Joule heating is used [34].

Not all companies present numbers for cooling rates. This could be because not every machine features a cooling system. The three companies that do have a machine with a cooling system are Kulicke & Soffa, ASM Amicra and BESI Datacon with cooling rates of 100 °C/s, 50 °C/s and 100 °C/s, respectively [34, 36–38]. This is significantly lower than the heating rates, which could be due to multiple reasons. As far as the companies provide information on their machine layout, the cooling system is always on top of the heating system, so it takes longer for the cooling power to influence the relevant area around the assembly than for the heating power [5]. Also, the focus in thermocompression bonding is on heating, so more effort will logically be spent on development of the heating system. Lastly, designing a cooling system is usually more difficult than a heating system, due to the fact that heat is more easily generated than removed [34].

2.2. Requirement specification

Requirements have been determined for the demonstrator based on the process parameters reported in literature and data sheets from bonding machine manufacturers [5, 34–40]. A distinction is made between design targets and technical requirements and so two tables are made.

2.2.1. Design targets

Table 2.3 contains the design targets: cost, weight, size, integration, throughput, modularity and maintenance. These are requirements that can not be quantified, but can be seen as pillars that design decisions are based on. Cost is the only target that is quantified, but it fits better in this category than in the technical requirement specification.

The cost limit (requirement 1.1) is based on the market trend: similar systems cost around €5000, based on TEGEMA's market knowleddge, which means that with a profit margin of 30%, the manufacturing costs must stay below €3500. For weight (requirement 1.2) and size (requirement 1.3) there is no strict limitation. The gantry cell has a footprint of 900x900 mm and has an open top. For bonding a relatively small electronic package it is unnecessary to exceed those dimensions and therefore the requirements are stated as minimizers. Reduced size usually reduces cost and reduced weight usually improves performance. The module should be integrable with TEGEMA's configurable machine platform (requirement 1.4), which also means that anything required for the bonding process that is not present on the machine platform should be in the module. The throughput (requirement 1.5), defined as the number of completed assemblies per unit time, is the parameter that the design proposed in this thesis

No.	Parameter	Description
1.1	Cost	The system should not cost more than €3500 to manufacture.
1.2	Weight	The system should be as light as possible.
1.3	Size	The system should be as compact as possible.
1.4	Integration	The system should be compatible with TEGEMA's configurable machine platform and should contain all necessary subsystems that are not present in the configurable machine platform.
1.5	Throughput	The system should minimize cycle time by decreasing heating and cooling duration.
1.6	Modularity	The system should be built up in a modular way, so that the user can conveniently choose a press surface size for their application.
1.7	Maintenance	The system should be easily maintainable, without the need for complete disassembly.

Table 2.3: Design target specification

	Lower limit	Upper limit	Unit
Dimensions			
Bond area length	-	3	mm
Bond area width	-	15	mm
Heating element			
Maximum heating rate	300	-	°C/s
Maximum cooling rate	150	-	°C/s
Maximum temperature	250	-	°C
Planar temperature variation	−5	5	°C

Table 2.4: Technical Requirement Specification

is expected to improve on. The module should also be applicable to a range of bond sizes. To reduce cost, it is therefore beneficial to create a modular design (requirement 1.6), so that only part of the module must be replaced according to the bond size. Lastly, maintenance is an expensive aspect of production, since the system is down as long as the maintenance lasts (requirement 1.7). Therefore it should not be difficult to reach and replace wearable parts. The general user requirements are not contributing to system's functionality but rather are constraining the design space.

2.2.2. Technical requirements

The technical requirement specification contains performance targets that are important to successfully prove the proposed concept (table 2.4). The first group of requirements are the dimensions of the bond area, i.e. the area in which electrodes to be bonded are located (see figure 1.1 for the bond layout). The length is the length of an electrode, the width is the distance between the outer edges of the outer electrodes.

The second group of requirements in table 2.4 are the performance requirements. The heating and cooling rates are based on what is currently available on the market, but also on what is realistic. Considering the state-of-the-art heating and cooling rates stated in section 2.1.4, the requirements are set as 300 °C/s heating and −150 °C/s cooling. These are the maximum rates that the module should reach, not the average rates over the entire heating and cooling steps. For instance: the heating rate will be higher at low temperature, the cooling rate at high temperature. It is decided that the demonstrator is designed to perform an ACA bonding process, which requires a process temperature of 180 °C. The maximum temperature that the heating element can withstand should be at least 250 °C; it must be warmer than the assembly itself due to intermediate heat loss and thermal inertia. Lastly, the temperature variation across the press surface must be less than ±5 °C, similar to what Kulicke & Soffa and BESI Datacon report [6, 37]. This is only required for the constant temperature step, not during heating and cooling.

2.3. Functional requirement specification

From the user requirement specification discussed in section 2.2, functional requirements (FRs) can be determined. FRs are the functions that the design must fulfill in order to satisfy the user requirements.

In this section an overview of the functional requirements is given in the following form:
FR → Strategy → Sub-strategy → Solutions → Sub-solutions
The functional requirements are arranged according to the MoSCoW method, which states which functions the machine "Must have", "Should have", "Could have" and "Won't have" [41].

2.3.1. The functional requirements

The list of functional requirements and their MoSCoW qualification can be seen in table 2.5. The qualification is based on how important each functional requirement is for demonstrating the heating and cooling concepts' performance.

No.	Function	MoSCoW
1	Heat press surface	Must have
2	Cool press surface	Should have
3	Uniform temperature distribution	Should have
4	Measure press surface temperature	Should have
5	Uniform pressure distribution	Could have
6	Manage contamination	Could have
7	Measure vertical force	Could have
8	Control collision impact	Could have
9	Measure vertical displacement	Won't have
10	Replace press	Won't have

Table 2.5: Functional Requirement Specification

There is one *must have* in the FRS: the module must be able to quickly heat the assembly. The reason that heating is most important is that it is a necessity for the bonding process, as opposed to for instance cooling, which merely accelerates the process.

The next three functions can be classified as *should haves*, as they are functions that enhance the performance and are not strictly necessary for a working concept: quick cooling, temperature uniformity and sensing press surface temperature. Quick cooling is the most important should have, as it is expected that this is part of the distinguishing feature of this design. The temperature should be spread evenly over the press surface to ensure a uniform quality level in terms of electrical resistance and mechanical strength over different electrodes. Temperature measurement is also not strictly required for a functional bonding machine, but accurate control of the temperature profile will lead to better joint quality and enables evaluation of joint quality with respect to temperature profile. Temperature measurement is also necessary to validate the theoretical models and characterize the demonstrator performance.

There are four *could haves* in this system: uniform pressure distribution, managing contamination, sensing vertical force and impact collision mitigation. None of them is crucial for a working demonstrator, but they are all important for a commercial product. Uniform pressure distribution enhances the uniformity of the bond height and therefore the overall performance quality of the bonding machine. Contamination management, keeping the press surface clean from adhesive contamination, becomes interesting when a high number of bonds is performed, significantly more than needed in this project. Measuring vertical force can be helpful in analyzing process parameters of a completed bond and relating them to joint quality. Lastly, the collision impact between the press and the assembly can be controlled to prevent components on the assembly to break.

Finally, the two *won't haves* are vertical displacement measurement and press replacement. They show negligible contribution to the bonding process for their own reasons. Measuring vertical displacement is only relevant for solder bonding, not for ACA bonding. This is because the ACA film height is determined by the conductive particles and the bonding pressure. Press replacement gives a choice of bond area. This is important for the commercial product, but not for the proof-of-concept demonstrator that is designed for one bond size.

2.3.2. From functions to solutions

Every function can be fulfilled with different strategies. All those strategies have several solutions (at least more than one). Strategies and solutions must always be mutually exclusive, i.e. one strategy cannot be related to another strategy. For instance, 'moving' and 'rolling' are not mutually exclusive because rolling is form of moving, but 'rolling' and 'sliding' are mutually exclusive. This structural method of finding solutions ensures that the entire design space is filled. It also creates an extensive table with strategies, sub-strategies, solutions and sub-solutions, which can be found in Appendix B.

3

System Architecture

In this chapter, the global concept for the module design is created. A morphological chart is used to generate concepts, by matching one or multiple solutions of each function with solutions from other functions. The three most promising concepts are investigated on feasibility. Finally, the most feasible concept is selected for the detailed design in chapter 4.

3.1. Morphological Chart

The morphological chart aims to organize all found solutions for each function for a complete overview of possible concepts. In some cases multiple solutions for one function can be integrated. Only the *must have* and *should have* functions are entered in the morphological chart, because the *could haves* could be combined with any concept, with up to 19 individual solutions. This is too extensive to evaluate every possible concept, so the chart must be refined. In the first refinement all solutions are evaluated on feasibility. The second refinement is the likelihood of a solution reaching the corresponding requirements. These two refinements narrow the chart down to about 50% of the initial chart. Lastly a decision matrix is made where a number of criteria with varying weight are graded for each solution. This is a matrix with nine criteria on the horizontal axis that give a comprehensive indication of the performance and all solutions to be graded on the vertical axis. The criteria with their corresponding weight factors between parentheses are the following:

- P = Performance (10), indicating the expected performance in terms of requirements it must achieve, speed and accuracy.
- I = Integration (9), indicating how easily the solution can be integrated into the full system.
- Cx = Complexity (7), indicating how complex the design and development of the solution will be.
- C = Cost(6), indicating the cost of manufacturing.
- Ct = Controllability (6), indicating how well the system can be controlled.
- E = Energy efficiency (4), indicating how much of the input energy is converted to useful energy by the solution.
- D = Durability (3), indicating how often the system (or part of the system) must be maintenanced or replaced.
- F = Flexibility (2), indicating how well the system can be adjusted to serve other conditions such as different assembly size.
- N = Novelty (1), indicating how innovative the solution is compared to existing solutions.

Function	Solution 1	Solution 2	Solution 3
Fast heating	Joule heating	Incandescent lamp	Heat exchanger
Fast cooling	Radiative cooling	Heat exchanger	Cooling fins
Distribute temperature	Uniform heat flux	Maximize diffusivity	Minimize volume
Measure bottom temperature	Thermocouple	RTD	Thermographic camera
Distribute pressure	Active rotational alignment	Universal joint	Elastic pressure surface
Contamination management	Disposable film	No extra layer	Clean off
Measure vertical force	Strain gauge	Piezo sensor	Capacitive load cell
Control collision impact	Copmliant press surface	Low speed z-movement	Velocity profile

Figure 3.1: Refined morphological chart with three solutions per function. The red cell is a must have, orange are should haves and green are could haves.

The weighted grades are summed to form a total score. Dividing this by the sum of all weight factors gives the final grade. The three highest graded solutions are selected for the morphological chart and the result is a clear, refined chart with which concepts are generated (figure 3.1).

3.2. Concept Generation

Theoretically, 3^8 concepts can be generated with this chart. Therefore, it is decided to focus on the fast heating and cooling functions, assuming that the temperature distribution and temperature measurement functions can be chosen based on whichever fits best. The could haves can be referred to for a final design. The morphological chart for heating and cooling can be seen in table 3.1. The possible combinations are:

- Joule heating + radiative cooling
- Joule heating + heat exchanger
- Joule heating + cooling fins
- Halogen + radiative cooling
- Halogen + heat exchanger
- Halogen + cooling fins
- Heat exchanger + radiative cooling
- Bidirectional heat exchanger
- Heat exchanger + cooling fins

The three most promising concepts are chosen and worked out in more detail. This includes discussing their working principle, making general calculations on performance and stating advantages and disadvantages. The three concepts are ”Joule Heating + Heat Exchanger”, ”Halogen + Heat Exchanger” and ”Bidirectional Heat Exchanger”.

Function	Solution 1	Solution 2	Solution 3
Heating	Joule heating	Halogen	Heat exchanger
Cooling	Radiative cooling	Heat exchanger	Cooling fins

Table 3.1: Morphological chart for heating element

3.2.1. Concept 1: Joule Heating + Heat Exchanger

This concept consists of a thin electrically conductive metal or ceramic track across which a voltage is applied so that electrical power is dissipated (figure 3.2). This track is in contact with the heating element, which transfers the heat to the press. The small heat transfer path length makes for small losses and fast response. A heat exchanger is placed on top of the heating system, through which a cold fluid flows. The (relatively) cold fluid takes up heat from the heating element and carries it away through the outlet. The use of air, which is available in the environment, eliminates the need for a closed system and therefore cooling of the fluid itself. Some advantages and disadvantages of this concept compared to the others are stated below.

Advantages

- Compact heating system
- Efficient heating system

Disadvantages

- Expensive heating system fabrication
- Heating system dependent on press surface size
- Electrical insulation required around heating system

The power that is dissipated by the heating system is approximately equal to the heat absorbed by the heating element. In the equation below, the required heating power is calculated, together with the heating system electrical resistance that follows, and an estimation of the electrical resistivity that the conducting material should have. All variables and their values can be found in table 3.2.

$$Q_{heating} \approx (\rho c)_m V \left(\frac{\partial T}{\partial t}\right)_h = 24\,\mathrm{W} = U^2/R, \qquad R = 24\,\Omega = \rho_e \frac{l}{A_{cs,h}} \rightarrow \rho_e \approx 0.75 \cdot 10^{-6}\,\Omega\,\mathrm{m} \tag{3.1}$$

This is at least $0.75 \cdot 10^{-6}\,\Omega\,\mathrm{m}$, which corresponds to stainless steel. This is not a conventional material to make such small features, but by improving the geometry it might be possible to use some other material.

In a similar fashion, the required cooling power is calculated in the equation below, leading to a mass flow requirement in the case of ambient air as the cooling fluid, from which a flow velocity can be calculated. All variables and their values can be found in table 3.2.

$$Q_{cooling} \approx (\rho c)_m V \left(\frac{\partial T}{\partial t}\right)_c = 12\,\mathrm{W} = \dot{m}_a c_a \Delta T_{HX} \rightarrow \dot{m}_a \approx 2.4 \cdot 10^{-4} kg/s \rightarrow u = \frac{\dot{m}}{\rho A_{cs,c}} = 25 m/s \tag{3.2}$$

The resulting flow velocity of $25\,\mathrm{m/s}$ is a realistic value, but using the expression for the heat transfer coefficient provided by Copeland, it shows that it is not sufficient to just have straight channels, see equation below [42]. Several solutions exist to make the flow more turbulent and therefore increase the cooling power, which must be investigated to fulfill the cooling requirement.

$$h_c = \frac{k_a}{D_H}\left[2.22^3\left(\mathrm{Re}\,\mathrm{Pr}\frac{D_H}{L_a}\right) + (8.31G - 0.02)^3\right]^{1/3} = 483\,\mathrm{W/(m^2K)} \rightarrow Q_{cooling} = h_c A_c \Delta T = 5.0\,\mathrm{W} \tag{3.3}$$

Lastly, the thermal resistance is calculated, which is a common measure for the heat exchanger performance. The higher this value, the higher the thermal gradient needed to achieved a certain cooling power.

$$R_{th} = \frac{\Delta T}{Q_{cooling}} = 36\,\mathrm{K/W} \tag{3.4}$$

Variable	Value	Unit	Description
$(\rho c)_m$	$2.5 \cdot 10^6$	J/ (m^3K)	Typical volumetric heat capcity of metal
V	$32 \cdot 10^{-9}$	m^3	Heating element volume
$\left(\frac{\partial T}{\partial t}\right)_h$	300	°C/s	Max heating rate
$\left(\frac{\partial T}{\partial t}\right)_c$	150	°C/s	Max cooling rate
U	24	V	Voltage across heating system
l	0.08	m	Total conducting length of heating system
$A_{cs,h}$	$2.5 \cdot 10^{-9}$	m^2	Heating system cross-sectional area
$A_{cs,c}$	$12 \cdot 10^{-6}$	m^2	Cooling system cross-sectional area
c_a	1000	J/ (kgK)	Specific heat capacity air [43]
k_a	0.026	W/ (mK)	Thermal conductivity air [43]
mu_a	$1.85 \cdot 10^{-5}$	Pa s	Dynamic viscosity air [43]
Re	811	-	Reynolds number air based on calculated velocity
Pr	0.707	-	Prandtl number air at room temperature [43]
D_H	0.5	mm	Hydraulic diameter cooling channel
L_a	4	4 mm	Cooling channel length
G	1/2	-	Parameter related to channel aspect ratio
A_c	$64 \cdot 10^{-6}$	m^2	Cooling surface area
ΔT	180	°C	Temperature gradient

Table 3.2: List of variables required for back of the envelope calculations on concept 1.

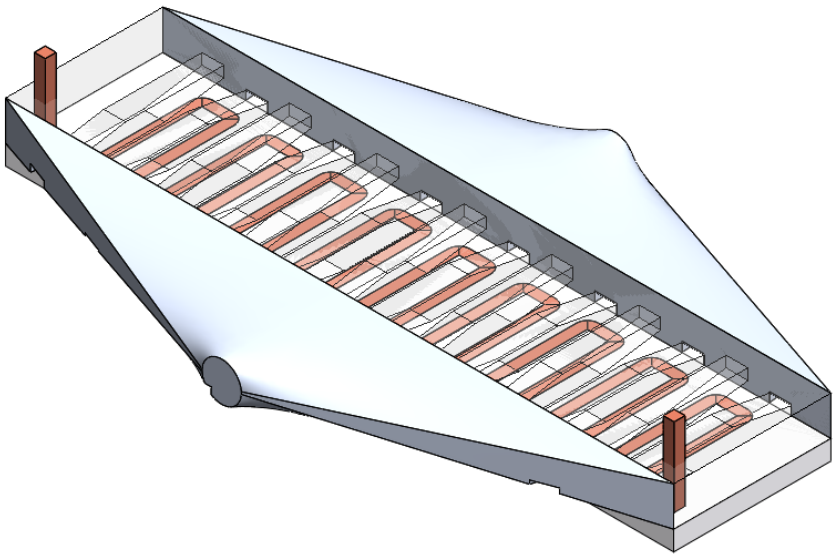

Figure 3.2: Concept 1: Joule Heating + Heat Exchanger. The bottom block is heated by applying a voltage over the conductive track (orange). Compressed air is blown through the cross-flow microchannel heat exchanger to cool the block down. The microchannels are transparent for illustration purposes.

3.2.2. Concept 2: Halogen Light Source + Heat Exchanger

In the second concept radiative heating is combined with the heat exchanger as explained in concept 1 (figure 3.3). The halogen light source irradiates a small collector surface on top of the press surface that is a good absorber of light with a specific wavelength, mostly visible and near-infrared in case of a halogen lamp. Absorbing radiation means conversion to heat and so the heating element heats up. Some advantages and disadvantages of this concept compared to the others are stated below.

Advantages

- Low cost off-the-shelf heat source
- Good controllability of heater
- High power capabilities of heater
- Similar temperature distribution for heating and cooling

Disadvantages

- Non-uniform heating
- Medium energy efficiency of heating system

Performance estimations for the heater are calculated below based on a 150 W halogen bulb modeled as a point source with the values in table 3.3. First the view factors between the three bodies (light source, reflecting surface and collector) are calculated below. The view factor from light source (L) to collector (c) is calculated by assuming that the light shines towards the lower semi-sphere (which has 180° in two orthogonal directions) and calculating the fractions of each semicircle that irradiates the collector. The rest of the light reaches the reflecting surface. Because the light source is modeled as a point source, it receives no radiation and 100% of the light leaving the collector reaches the reflecting surface. This also means that the ratio of surface areas equals the amount of light leaving the reflecting surface that reaches the collector surface. The remainder is self-irradiation of the reflecting surface.

$$F_{Lc} = \left(\frac{\arctan\left[(W/2)/H\right]}{180}\right)\left(\frac{\arctan\left[(L/2)/H\right]}{180}\right) = 0.0027 \rightarrow F_{Lr} = 1 - F_{Lc} = 0.9973 \tag{3.5}$$

$$F_{cr} = 1 \rightarrow F_{rc} = \frac{WL}{A_r}F_{cr} = 0.03 \rightarrow F_{rr} = 1 - F_{rL} - F_{rc} = 0.97 \tag{3.6}$$

With all view factors known, the net heat flux reaching the collector surface can be calculated. This is done by first calculating the radiosity towards the collector surface, due to the othe two surfaces, and then subtracting the emissivity and multiplying by the surface resistance.

$$J_i = \varepsilon_i \sigma T_i^4 + (1 - \varepsilon_i)\sum_{n=1}^{j} F_{ij}J_j \tag{3.7}$$

$$Q_c = (J_c - \sigma T_c^4)\frac{\varepsilon_c WL}{1 - \varepsilon_c} = 25\,\text{W} \tag{3.8}$$

It complies well with the required heating power found in equation 3.1 which means that this concept is capable of reaching the heating requirement.

Variable	Value	Unit	Description
W	0.015	m	Heating element width
L	0.003	m	Heating element length
h	0.020	m	Light source height w.r.t. collector surface
A_r	0.0015	m^2	Light source radiating surface
σ	$5.67 \cdot 10^{-8}$	$W/(K^4 m^2)$	Boltzmann constant [44]
ε_c	0.9	-	Collector surface emissivity
ε_r	0.1	-	Reflecting surface emissivity
ε_L	0.4	-	Light source surface emissivity
T_c, T_r	293	K	Collector and reflector initial temperature
T_L	3450	K	Light source initial temperature [45]

Table 3.3: List of variables required for back of the envelope calculations on concept 2.

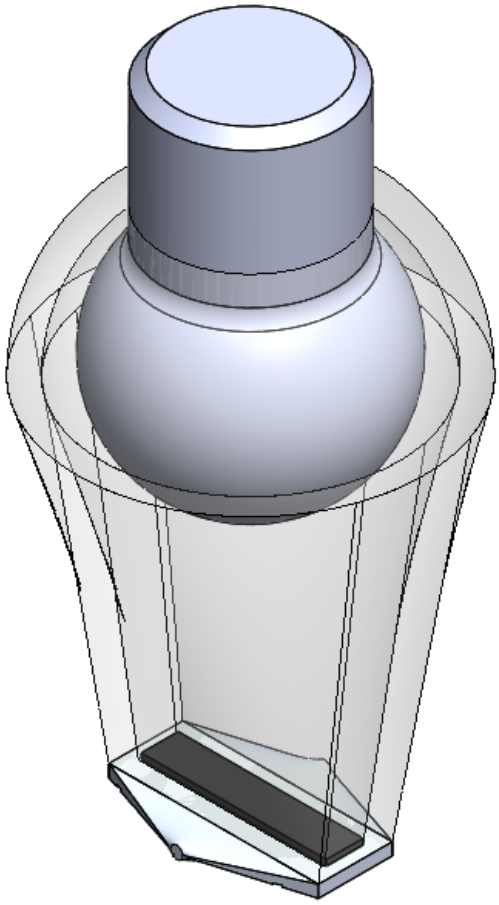

Figure 3.3: Concept 2: Radiative Heating + Heat Exchanger. In this concept, the block is heated by irradiating an infrared absorbing surface. The cooling system is the same as in concept 1. The radiation cavity is transparent for illustration purposes

3.2.3. Concept 3: Bidirectional Heat Exchanger

In the last concept the heat exchanger is used for both heating and cooling, which is referred to as a bidirectional heat exchanger (figure 3.4). The flow enters from above, at the center of the heating surface, and is forced to flow towards the long edges; this is the shortest path and thus ensures the most uniform temperature distribution. This concept is less complex and easier to integrate than the other concepts. To achieve a high fluid temperature for heating, there must be either a large tank with heated fluid or a powerful heating device must be installed somewhere along the channel. In the first case there will be energy losses due to the imperfect insulation of the tank and the transport along the channel, and it will be virtually impossible to cool down the tank with fluid at the required rate when cooling is required. Therefore, the second case is more realistic. Some advantages and disadvantages of this concept compared to the others are stated below.

Advantages

- Integrated heating and cooling
- Same temperature distribution for heating and cooling

Disadvantages

- Ineffective heating system
- Extra heat exchanger required for heating the fluid
- High temperature resistance required around fluid heater

Since the heating system must be twice as powerful as the cooling system, the temperature difference must be twice as large by approximation. Using the thermal resistance found in equation 3.4, the fluid must be around $8.7 \cdot 10^2$°C to fulfill the requirement. This requires $2.1 \cdot 10^2$W to be transferred to the fluid (in the case of air), as calculated below, using the values from table 3.4.

$$T_f = T_e + R_{th}Q_{heating} = 20 + 36 \cdot 24 = 8.7 \cdot 10^2\text{°C} \rightarrow Q = \dot{m}c\left(T_f - T_e\right) = 2.1 \cdot 10^2\text{W} \quad (3.9)$$

In practice, the heater must be even hotter than $8.7 \cdot 10^2$°C because the fluid needs to reach this temperature quickly. Also it needs to cool down in time for the cooling action. Apart from the losses in heating and transporting the fluid, only about 10% of this energy is transferred to the press surface, the rest is blown into the surrounding air.

Variable	Value	Unit	Description
T_e	20	°C	Environment temperature
R_{th}	36	K/W	Thermal resistance of heat exchanger
$Q_{heating}$	24	W	Required heating power
$\dot{m}$	$2.4 \cdot 10^{-4}$	kg/s	Calculated mass flow
c	1000	J/ (kgK)	Specific heat capacity air [43]

Table 3.4: List of variables required for back of the envelope calculations on concept 3.

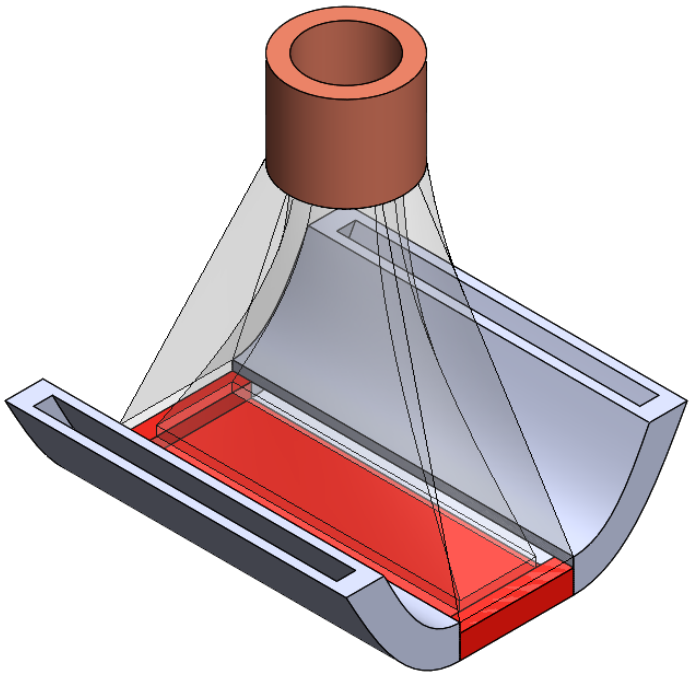

Figure 3.4: Concept 3: Bidirectional Heat Exchanger. Both heating and cooling occurs in a forced convection heat exchanger. A heating element (copper tube) is placed upstream of the heat exchanger (red) to heat the air to the required temperature. The fluid channel is transparent for illustration purposes.

3.3. Concept Selection

To select the most promising concept, a decision matrix is made (figure 3.5). The concepts are graded on performance, integration, complexity, cost, controllability, energy efficiency, durability, flexibility and novelty with descending weight. All grades are weighted and added up for a total score. Despite having different pros and cons, concept 1 and 3 score nearly the same amount of points, but concept 2 is clearly the most promising concept, due to its good performance potential, simplicity, controllability and novelty. In the next chapter this concept is worked out in detail.

Weight	10	9	7	6	6	4	3	2	1		
Criterion	P	I	Cx	C	Ct	E	D	F	N	Total	Weighted score
Concept 1	10	9	7	6	8	9	10	7	6	400	8,3
Concept 2	10	8	8	9	9	8	7	8	10	415	8,6
Concept 3	7	10	8	10	8	6	9	8	8	399	8,3

Figure 3.5: Decision matrix of the final concept selection. The labels on the x-axis are respectively: (P)erformance, (I)ntegration, (C)omple(x)ity, (C)ost, (C)on(t)rollability, (E)nergy efficiency, (D)urability, (F)lexibility and (N)ovelty. The y-axis contains three concepts, respectively: joule heating + heat exchanger, halogen light source + heat exchanger and bidirectional heat exchanger.

4

Detailed Design

This chapter describes the detailed design of the bonding module. After an explanation of the system layout, the design is described from a functional point of view, starting with heating, then cooling and finally the complete system, supported by analytical and numerical models for performance characterization. The analytical and numerical performance characterization includes the FOS assembly, which consists of a flex circuit, ACA layer and FR-4 PCB.

4.1. System layout

The most important part of the system is the press surface. This is the surface that applies pressure and heat to the FOS assembly and has predefined minimal dimensions as stated in chapter 2. The press surface is sized slightly bigger than the actual bonding area to allow a small error margin for alignment: 4x16mm. The design takes into account that the press surface dimensions should be adjustable, so the system is built up step by step: first the heating element is added to the press surface. This is the component that regulates the press surface temperature by either absorbing energy from the heating system or releasing energy to the cooling system. The heating system is placed on top of the heating element and the cooling system along the sides, while the actual heat transfer of both systems takes place on the heating element. This reduces the distance between the heated/cooled surface and the press surface. A schematic overview of the system layout is given in figure 4.1.

4.2. Heating system design

The heating element is heated by a halogen light source. The path that the energy travels is thus:
Current: electrical energy → Dissipation in filament: heat → Hot filament starts glowing: thermal radiation → Absorption by heating element: heat
This means that the design of the heating system requires understanding of three physical processes: incandescence, radiative heat transfer and the absorption of radiation (and thereby conversion to heat).

4.2.1. Incandescence

Every surface emits radiation in a spectrum of wavelengths as a result of temperature; the higher the temperature, the smaller the wavelength of the peak intensity [44]. This is called incandescence. A halogen light bulb filament has a temperature higher than 3000 K and its emission spectrum can be seen in figure 4.2 [46]. The high temperature is beneficial for radiative heat transfer, because it scales to the power four: $q_{rad} \propto \sigma T^4$. For the same reason, halogen lamps are deemed inefficient for producing visible light: only 20% of the emission is in the visible spectrum at this temperature, see the dotted lines in figure 4.2.

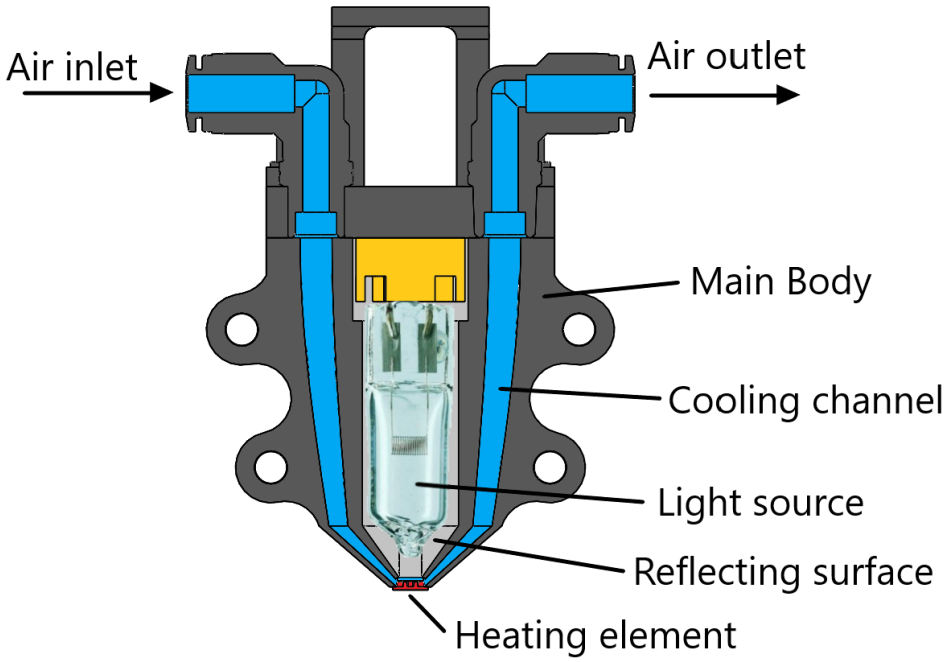

Figure 4.1: A schematic overview of the full system layout.

4.2.2. Radiative heat transfer

Since radiation travels in all directions equally, there must be some mechanism to direct all radiation energy towards the heating element. There are several ways to focus radiation.

The most conventional are semi-elliptic and parabolic reflectors, used in most commercial lighting systems [46]. When the light source is in the focal point of the reflector, the radiation will be collimated in a parabolic reflector or focused on a second focal point in a semi-elliptic reflector. The implementation of such reflectors is challenging in this specific application, since the irradiated surface is small compared to the quartz envelope of the lamp. The reflector is behind the light source, but reflected rays must still have a clear path towards the heating element. The result is a large system which is difficult to package with the cooling system. The manufacturing tolerances of the glass are low, making it difficult to position the light source exactly in the focal point with a fixed lamp holder. When the source is not exactly in the focal point, the radiation scatters off the reflector surface and the focusing effect is lost. Proper optical design is necessary to manage the manufacturing uncertainty.

Instead of focusing the light, it can also be merely reflected. This does not require the radiation source to be in a certain point and can be much more compact, reducing the reflecting surface and thus the losses due to imperfection of the reflecting surface, i.e. emissivity higher than zero. This method of radiation redirection is used in this demonstrator design because of its manufacturing feasibility and integratability into the system. The most suitable coatings for this application are protected silver and protected gold, with reflectance values up to 95% [47].

4.2.3. Radiation absorption

Radiation is best absorbed by a black body radiator. This is a body that absorbs and emits 100% of the incoming radiation, no reflection and transmission. Even though perfect black bodies do not exist, a carefully selected surface coating can make a body 90-95% radiation absorbing [48]. The requirements for this coating emerge from the spectral distribution of the emitted light, see figure 4.2. It can be seen that the maximum intensity occurs around 900 nm, which is in the near-infrared (NIR) spectrum. The most energy is emitted at wavelengths

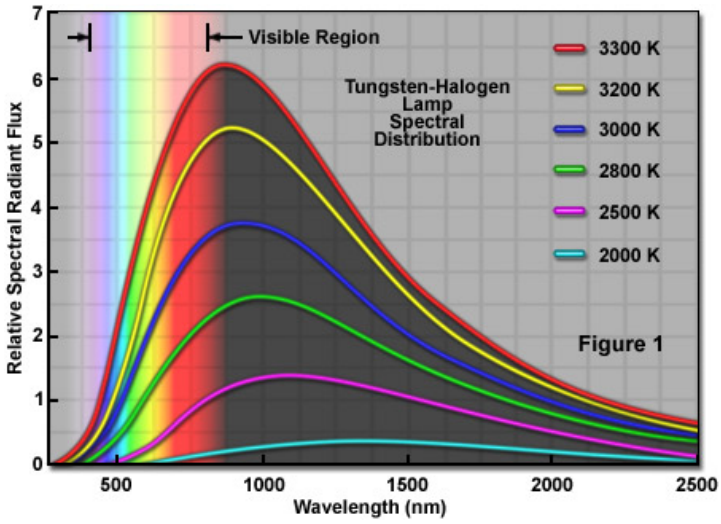

Figure 4.2: Emission spectrum in visible (between dotted lines) and near-infrared range at different temperatures [46].

between visible (390 nm) and short-wavelength infrared (2.5 µm). Therefore a coating must be used that absorbs radiation well in this entire range.

Acrylic paints are available in high-temperature editions and are known to be an excellent infrared radiation absorbing material. The colour can positively influence the absorbed energy in the visible spectrum without affecting the infrared absorption. Therefore a black acrylic paint is chosen, which absorbs well also in the visible spectrum. Matt black spray paint is used, which has a general emissivity of 0.95 [48]. A drawback of using paint as the absorbing coating is its low thermal conductivity: almost 1000 times as low as aluminium [49]. This means that its thermal resistance is equivalent to that of an aluminium sheet that is 1000 times as thick. The result is a significant temperature drop over the paint, calculated for 20 µm thickness (provided by paint manufacturer Electrolube, equation 4.1) and 50 µm thickness (when applied too excessively, equation 4.2). A heating power of 24 W and a surface of 64 mm^2 equals a heat flux of 375 kW/m^2 towards the heating element. The paint must be 60 °C to 146 °C warmer than the required press surface temperature.

$$L_{paint} = 20\,\mu m \rightarrow R_{th} = \frac{L_{paint}}{k_{paint}} + \frac{L_{Al}}{k_{Al}} = \frac{20 \cdot 10^{-6}}{0.13} + \frac{5 \cdot 10^{-4}}{119} = 1.6 \cdot 10^{-4} \quad (4.1)$$

$$L_{paint} = 50\,\mu m \rightarrow R_{th} = \frac{50 \cdot 10^{-6}}{0.13} + \frac{5 \cdot 10^{-4}}{119} = 3.9 \cdot 10^{-4} \quad (4.2)$$

4.2.4. Halogen lamps and life time

Halogen lamps expire when the tungsten filament snaps. This happens because the filament gets so hot that the material partially evaporates. The halogen cycle helps to condensate this material back onto the filament. However, the evaporation will take place in the smallest cross-section of the filament, but the condensation can take place anywhere on the filament, most likely not at the same location. This makes the filament narrower and narrower at that specific location, until there is no material left and the filament is split in two [46].

It is reported that the relation between life time and applied voltage (relative to the recommended voltage) is according to equation 4.3 [46, 50]. This means that a 5% decrease in operating voltage already doubles the life time, equation 4.4. Looking at a typical thermocompression temperature profile, the rated voltage is applied to the lamp during the entire heating step (by approximation), a lower voltage is applied during the bonding itself, and no voltage during cooling.

Assuming a heating rate of 300 °C/s as required, the heating will take place in no longer than 1.5 s. The life time reduction during the bonding step is so little compared to the heating step, that this can be neglected in the life time approximation, see equation 4.5. This means that the life time can be approximated by 1.5 s at rated voltage per cycle. The used lamp

has a 50% failure time of 40h [45], so the total number of cycles before 50% of the lamps fail is $96 \cdot 10^3$. The failure distribution is not reported, so it is advised to replace the lamp after $50 \cdot 10^3$ cycles. The cost per assembly due to lamp failure is thus 0.5% of 1 cent when the lamp costs €2.5. Another factor influencing the life time is called inrush current, this is discussed in section 5.3.2.

$$t_{life} \propto V^{-14} \tag{4.3}$$

$$\frac{t_{95\%}}{t_{100\%}} = \left(\frac{V_{95\%}}{V_{100\%}}\right)^{-14} = 2.05 \tag{4.4}$$

$$\frac{t_{50\%}}{t_{100\%}} = \left(\frac{V_{50\%}}{V_{100\%}}\right)^{-14} = 1.6 \cdot 10^3 \tag{4.5}$$

4.3. Cooling system design

The cooling system uses a forced air flow across the heating element surface that takes up as much heat as possible and carries it away from the heating element. The choice of using ambient air as the cooling fluid means that no closed system or fluid reservoir is necessary and no fluid needs to be cooled. The system contains an inlet, a diffuser channel to change the cross-section and the heat exchanger where the cooling takes place. In this section, the diffuser and heat exchanger are described, clarified by an explanation of the physics involved: convection and thermal boundary layer formation.

4.3.1. Air channel

From the inlet to the cooling surface, the air flows through a diffuser and a bend. The diffuser must be there, because the inlet cross section (5mm circular) is different from the outlet cross section (0.75x16mm). When the transition is a sudden expansion, the flow will separate from the wall and the flow at the sides of the outlet will be close to stationary or even reversed [51]. By introducing the diffuser, whose cross-section gradually changes over length, the flow can follow the channel walls better and the velocity distribution at the outlet is more uniform [51]. Downstream of the heat exchanger, the channel is symmetric with the inlet to facilitate fabrication.

4.3.2. Convection

In order to be able to increase the convection coefficient h_c, the physical process of convection must be understood. Convection is the heat transport through a fluid as a result of movement of the fluid. When a fluid flows along a hot surface, heat is conducted from the hot surface to the fluid [44]. As the cooling fluid exits the heat exchanger, it carries away the excess heat, thus cooling the hot surface. In the case of turbulent flow, mixing is promoted by the vortices, so the fluid has a more uniform temperature. A uniform temperature means it is lower at the hot surface than without mixing and so the temperature difference is higher. Therefore, turbulent flows generally give better cooling performance than laminar flows in heat exchangers.

4.3.3. Thermal boundary layer

Another key influence on heat exchanging performance is the thermal boundary layer. When a fluid enters a channel with hot walls, heat is transferred from the walls to the fluid. As the fluid advances through the channel, the hot temperature penetrates further into the fluid, until it reaches the center. The region until this point is called the thermal entrance region, the region after this point is the fully developed region [44]. The thermal boundary layer is the part of the fluid where the temperature starts to increase towards the hot wall. This layer grows as a function of channel length. Because the temperature difference between the wall and the fluid is higher in the entrance region than in the fully developed region, the Nusselt number is also higher, which is proportional to the convective heat transfer coefficient. By continuously reintroducing the entrance region, the convection coefficient can be higher than in a fully developed flow. The thermal boundary layer is illustrated in figure 4.5 [44].

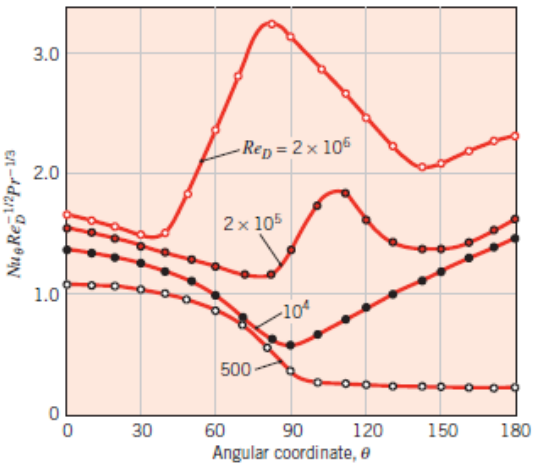

Figure 4.3: Local Nusselt number of cylinder in cross-flow [44]. At low Reynolds number, convection is high at the forward and backward stagnation points ($\theta = 0°$ and $\theta = 180°$) and low at the separation point ($\theta = 90°$).

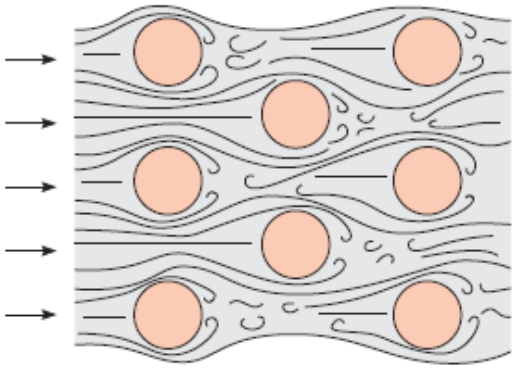

Figure 4.4: Flow condition for staggered tubes [44]. The flow zigzags around the tubes, which promotes mixing and therefore temperature uniformity.

4.3.4. Heat exchanger

Turbulence can be created by disturbing the flow along its path, for instance by placing vertical tubes [44]. A stagnation point is created in front of the tube, where convection is highest. As the fluid flows along the sides, a boundary layer is developed which decreases convection. The bottom limit is at the separation point, where the fluid loses contact with the cylinder. Now the flows becomes turbulent and vortices appear, which reduce the boundary layer again and thus increase the convection coefficient. A visual representation of this can be seen in figure 4.3 at $Re_D = 10^4$.

To effectively implement cylinder forced convection in a heat exchanger, an array of tubes is designed and characterized by Zukauskas et al. [52]. The configuration of the tubes can be either aligned or staggered (figure 4.6). Staggered configurations are believed to be more efficient in tight spaces because there is no free path for the fluid to cross the heat exchanger and so it must zigzag around the tubes (figure 4.4) [44, 52]. The tubes also act as cooling fins, increasing the cooling surface.

A plate is added on top of the tubes that forms a boundary for the air, but is transparent to visible and near-infrared light. Few materials are known that are highly transparent in this region, which is important for the energy efficiency of the system. Although quartz and fused silica are technically the most suitable option with a transmittance of more than 95% upon vertical irradiance, they are expensive [53]. Borosilicate glass has a transmittance

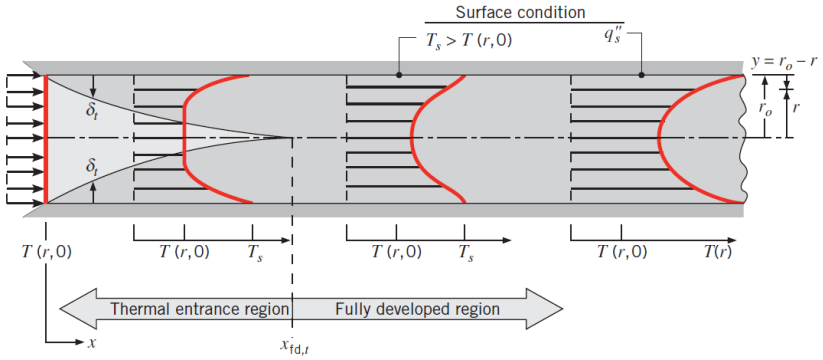

Figure 4.5: Thermal boundary layer development in a circular tube with a hot wall [44].

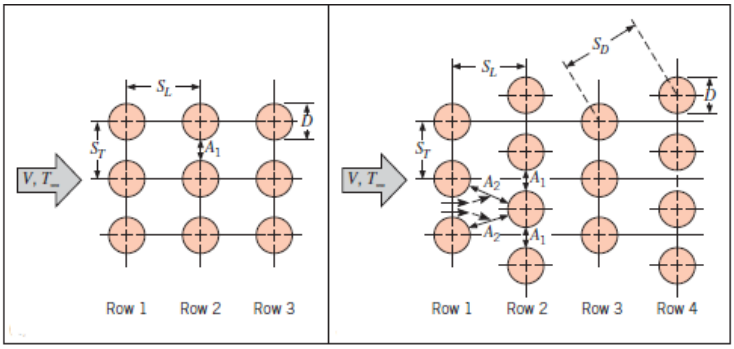

Figure 4.6: Heat exchanger tube arrangements [44]. Left: Aligned. Right: Staggered.

of more than 90% upon vertical irradiance and is affordable. It is therefore chosen as the most suitable material for this demonstrator. The chosen material is called D 263 T and is developed by Schott [54].

Although the vertical tranmission of the chosen material is 90%, many rays will reach the glass plate from a different angle. The higher the angle of incidence, the higher the reflectance and the lower the transmission. Using the Fresnel equations, it has been calculated that when taking into account all angles between 0 and 90 ° (symmetric) of equal intensity, the overall transmission is 80% [55]. This is a worst case value, since few rays will have an angle of incidence close to 0°.

The choice of flow direction can influence the performance of the heat exchanger because the fluid temperature rises as it flows over the hot heating element, making the temperature difference lower downstream; lower temperature difference means lower heat flux. By choosing the smallest press surface dimension (the width of 4 mm) as the flow direction, the fluid temperature has less opportunity to rise. Apart from a higher average cooling power, this also makes the temperature profile on the press surface more uniform.

4.4. Heating element design

The heating element has three important functions: it must heat up and cool down as quickly as possible and the temperature profile on the bottom surface must fulfill the uniformity requirement. This is all summarized in equation 4.6 and the design is illustrated in figure 4.7. The maximum potential temperature rate of change is affected by several material properties and several geometric parameters.

$$\rho c \frac{\partial T}{\partial t} = k \Delta T \tag{4.6}$$

4.4.1. Material properties

To maximize the temperature rate of change, the heat capacity must be as low as possible so that less input power is required and less heat must be carried away by the cooling system. The heat capacity consists of specific heat capacity, density and volume.

High thermal conductivity is desired because heat must be conducted from the heating surface (top) to the press surface (bottom) and vice versa. High thermal conductivity results in a more uniform temperature distribution in the heating element, which is also a requirement. All together the heating element material should have high thermal conductivity and low volumetric heat capacity, which is the same as having a high thermal diffusivity. From a database of common materials in CES EduPack, aluminium has the best combination of diffusivity, machinability and cost and can withstand temperatures up to 300 °C [56].

4.4.2. Geometric parameters

The right side of equation 4.6 contains geometric information: ΔT is the second spatial derivative of temperature. Since the volume must be minimized to minimize the heat capacity, the

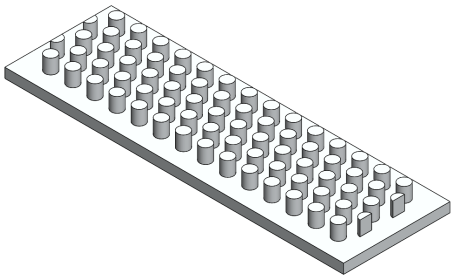

Figure 4.7: Illustration of the heating element. The pillars enhance cooling and the low thickness promotes temperature uniformity.

surface area in the horizontal plane is chosen as small as possible, which is the same size as the press surface: 4x16mm. This makes that heat only travels vertically by approximation, making the horizontal temperature gradients negligible (note that the radiation projection is nonuniform and therefore there is a small horizontal temperature gradient). With the assumption that there is only a vertical temperature gradient, the temperature distribution is given below.

$$\frac{T(z,t)-T_\infty}{T_0-T_\infty}=\sum_{n=1}^{\infty}A_n e^{-\lambda_n^2\tau}\sin\left(\lambda_n\frac{z}{L}\right) \tag{4.7}$$

When this function is differentiated twice with respect to z, a factor $-\left(\frac{\lambda_n}{L}\right)^2$ appears. A smaller L (thickness) gives a higher gradient, so the bottom surface heats up quicker with a thinner element. Apart from this, the heat enters through a surface and heats up a volume, so the highest rate of change is achieved with the highest surface to volume ratio, which is at small thickness in this case. Reducing the volume not only increases temperature rate of change, it also improves the efficiency, since the energy used to heat up the heating element will never go into the electronic assembly but is carried away by the cooling system. A thickness of 0.5 mm is chosen. The result is a 90% reduction in energy loss, compared to a hotbar bonding machine from Amada Miyachi or Nordson DIMA [35, 39]. This number is based on the heated volume difference and heat capacity at a process temperature of 200 °C.

4.5. Analytical performance evaluation

In this section the performance of the heating and cooling systems is evaluated using analytical models. The FOS assembly is also analyzed at a certain temperature input to investigate the temperature distribution in a 1D unsteady heat transfer model.

4.5.1. Heating system

The analytical radiation problem consists of three surface elements: lamp filament, reflector and absorbing surface. Such a problem with few surfaces is often represented by an electric circuit, where thermal resistance is analogous to electrical resistance, voltage to radiosity and current to heat flux. The result is similar to an electrical circuit with three voltages and six resistances, see figure 4.8 [44]. Each body has a surface resistance and each pair of bodies has a spatial resistance. Surface resistance is influenced by emissivity and surface area, spatial resistance is influenced by surface area and view factor.

Although it gives insight in the physics of the problem, the electrical analogy is not the most efficient way of solving the problem. Alternatively, the fluxes can be calculated via equation 4.8, where heat flux is equal to the difference between radiosity and black-body emissivity, divided by the surface resistance. Equation 4.9 describes the radiosity of surface element i. It is equal to its black body radiation times the emissivity plus the irradiance on surface element i from all other surface elements.

$$Q_i=\frac{J_i-E_{bi}}{R_i} \tag{4.8}$$

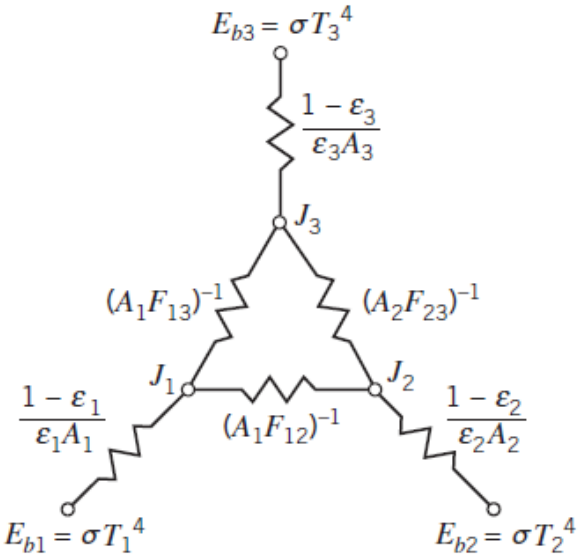

Figure 4.8: Electrical resistance scheme analogy for solving radiative heat transfer problems [44]

$$J_i = \varepsilon_i \sigma T_i^4 + (1-\varepsilon_i) \sum_{j=1}^{n} F_{ij} J_j \tag{4.9}$$

There are several assumptions made in this model:

- Emissivity is independent of temperature, angle of incidence and wavelength
- Emissivity is equal to absorptivity (due to wavelength independence)
- All transmission coefficients are equal to zero
- Air does not contribute as a radiation medium
- All surfaces emit only diffusely; there is no specular component
- All surfaces have a perfectly uniform temperature distribution
- All materials are isotropic and homogeneous
- All walls are perfectly insulated
- The collector and reflector surface form a closed chamber, encapsulating the filament
- Shadowing effects are neglected
- 95% of the electrical power is radiated to the reflector and collector [57]
- The glass plate is not considered as a physical object in the calculations, but a transmission of 80% is integrated in the power output of the filament. This inherently assumes that radiation passes through the glass plate only once.

Combining the three equations for radiosity leads to the following matrix equation, which is solved with MATLAB.

$$\begin{bmatrix} 1-(1-\varepsilon_1)F_{11} & -(1-\varepsilon_1)F_{12} & -(1-\varepsilon_1)F_{13} \\ -(1-\varepsilon_2)F_{21} & 1-(1-\varepsilon_2)F_{22} & -(1-\varepsilon_2)F_{23} \\ -(1-\varepsilon_3)F_{31} & -(1-\varepsilon_3)F_{32} & 1-(1-\varepsilon_3)F_{33} \end{bmatrix} \cdot \begin{bmatrix} J_1 \\ J_2 \\ J_3 \end{bmatrix} = \begin{bmatrix} \varepsilon_1 E_{b1} \\ \varepsilon_2 E_{b2} \\ \varepsilon_3 E_{b3} \end{bmatrix}$$

The view factor from the collector surface to the filament is calculated using equations from Ehlert and Smith and the rest can be derived using the following identities [58]:

$$R_{ij} = 1/A_i F_{ij} = 1/A_j F_{ji} = R_{ji} \tag{4.10}$$

$$\sum_{j=1}^{n} F_{ij} = 1 \tag{4.11}$$

For the analytical model, the staggered tubes are first neglected, because the self-vision view factor is difficult to compute. In the end the analytical model is used to verify the numerical model, which will then also have a flat collector surface at first. All dimensions are taken from the CAD model and the halogen lamp data sheet provided by Philips [45]. For the collector and reflector emissivities the following values were assumed:

$$\varepsilon_c = 0.90, \quad \varepsilon_r = 0.05$$

The resulting heat flux from the filament to the collector is 34 W. This is about 23% of the input power of 150 W. The desired performance of the heating system is focused on the temperature rate of change of the heating element. This means that the obtained heat flux is not sufficient to estimate performance. The heat equation must be used again, this time with an added component: radiation. It is shown in equation 4.12 [59]. The material properties of AlSi10Mg for the following calculations are taken from GPIprototype [60].

$$\rho c_p \frac{\partial T}{\partial t} - k\Delta T = \nabla q_r \tag{4.12}$$

Since the thickness of the heating element is so small, the temperature reaches the bottom almost instantly, according to:

$$t = \frac{d^2}{4\alpha} = \frac{(5 \cdot 10^{-4})^2}{4 \times 4.6 \cdot 10^{-5}} = 1.3\,\text{ms}$$

Therefore, for this particular case the heat equation can be approximated by equation 4.13.

$$\rho c_p V \frac{\partial T}{\partial t} = Q_r \tag{4.13}$$

where V denotes the volume of the heating element and Q_r is the heat flux calculated above. Now the temperature rate of change at time instant zero can be estimated:

$$\frac{\partial T}{\partial t} = \frac{Q_r}{\rho c_p V} = \frac{34}{2600 \times 910 \times 48.13 \cdot 10^{-9}} = 3.0 \cdot 10^2 \text{K/s}$$

4.5.2. Cooling system

There are two performance indicators linked to the cooling system. One is the cooling power (heat transfer) and the other is the pressure drop over the air channel (fluid mechanics). First, the cooling power is analyzed. This leads to the required flow velocity, which is inserted in the pressure drop formula.

Zukauskas has researched the characteristics of staggered-tube cross flow heat exchangers [52]. His research provides governing equations for the Nusselt number, with which the heat transfer coefficient and cooling power can be calculated, and the pressure drop, for which he provides look up tables for the minor loss coefficient and friction coefficient as a function of Reynolds number.

The expression for the average Nusselt number can be seen in equation 4.14. S_T, S_L, C_1, C_2 and m are the design variables and Pr and Pr_s are fluid properties. The convective heat transfer coefficient can then be calculated according to equation 4.15. All fluid properties are evaluated at film temperature. The Reynolds number that appears in equation 4.14 is based on the maximum velocity that the air flow will experience, which is at the narrowest passage.

It can be geometrically derived which passage is the narrowest as shown in equation 4.16, where subscript T denotes transverse (cross-wise) and subscript D denotes diagonal.

$$\overline{Nu}_D = 1.13 C_1 C_2 Re^m Pr^{0.33} \tag{4.14}$$

$$\overline{h} = \overline{Nu}_D \frac{k}{D} \tag{4.15}$$

$$V_{max} = \begin{cases} \frac{S_T}{S_T - D} V, & \text{if } S_D \geq \frac{S_T + D}{2} \\ \frac{S_T}{2(S_D - D)} V, & \text{otherwise} \end{cases} \tag{4.16}$$

The first consideration in the design of the heat exchanger is the configuration. According to Zukauskas' findings, the effectiveness increases substantially when the number of stream-wise (longitudinal) rows of tubes goes from 1 to 5, and then gradually saturates. Therefore, 5 rows give a good balance between this effectiveness factor (C_2 in equation 4.14), tube size for manufacturability and the fact that more tubes have a higher effective cooling surface area. This gives room for 14 tubes in the transverse direction. C_1 is a constant related to the efficiency at different Reynolds numbers and is equal to 0.482 for the range that is applicable to this heat exchanger [52].

When the average heat transfer coefficient is known, the cooling power can be calculated. In a basic heat flux equation this is done by multiplying the heat transfer coefficient by the temperature difference. However, in a heat exchanger the temperature difference varies over the longitudinal direction. Therefore, a log-mean temperature difference is used which is calculated as follows [44]:

$$\Delta T_{lm} = \frac{(T_s - T_i) - (T_s - T_o)}{log\left(\frac{T_s - T_i}{T_s - T_o}\right)} \tag{4.17}$$

For this expression, the outlet temperature is required, which is calculated in equation 4.18 by realizing that the amount of heat taken up by the air is $\dot{Q} = \dot{m} c_p \Delta T$ where ΔT is the temperature difference between the inlet and outlet.

$$log\left(\frac{T_s - T_i}{T_s - T_o}\right) = \frac{\pi D N \overline{h}}{\rho V N_T S_T c_p} \tag{4.18}$$

By setting this equal to the cooling power equation, the outlet temperature is the only unknown because the unknown heat flux values are cancelled out. This is summarized the following two equations.

$$\dot{Q}/L = N(\overline{h} \pi D \Delta T_{lm}) \tag{4.19}$$

$$\dot{Q} = \dot{m} c_p (T_o - T_i) \rightarrow \dot{Q}/L = \rho V N_T S_T c_p (T_o - T_i) = N(\overline{h} \pi D \Delta T_{lm})$$
$$\rightarrow \frac{N(\overline{h} \pi D)}{\rho V N_T S_T c_p} = \frac{T_o - T_i}{\frac{T_o - T_i}{log\left(\frac{T_s - T_i}{T_s - T_o}\right)}} = log\left(\frac{T_s - T_i}{T_s - T_o}\right) \tag{4.20}$$

The required cooling power is approximately 22 W, based on equation 4.21. The velocity needed to achieve this power is found to be 30 m/s.

$$Q = \rho c V \frac{\partial T}{\partial t} = 2600 \cdot 910 \cdot 62.88 \cdot 10^{-9} \cdot 150 = 22.3\,\text{W} \tag{4.21}$$

The pressure drop is the result of minor losses, such as bends, diffusers and obstacles, like the ones used to make the flow turbulent, and major losses, caused by wall effects. Normally, knowing the pressure drop is necessary for the selection of a pump. In this case there already is a pump, but the pressure drop is still needed to know the velocity for a certain input

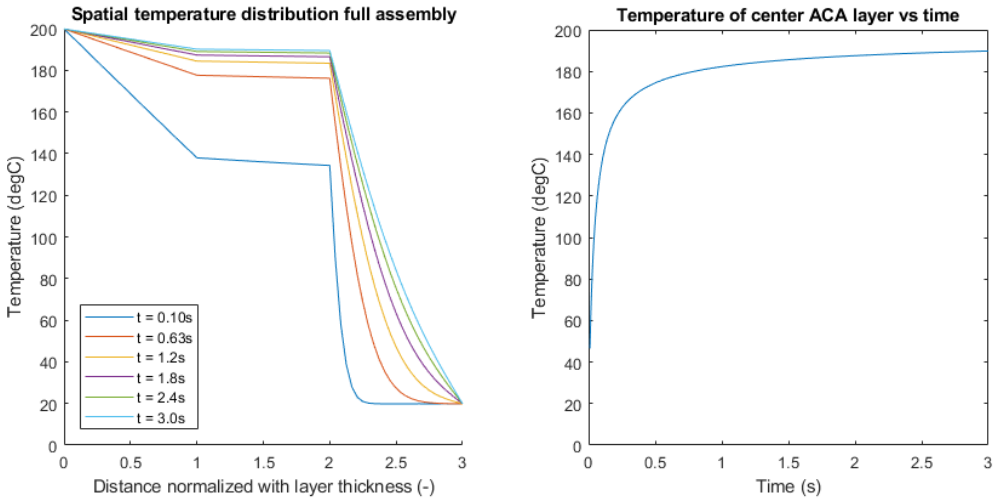

Figure 4.9: Temperature response in the FOS assembly at various time points (left) and center ACA temperature vs time (right) when exposed to a 200 °C step input.

pressure and therefore the cooling power at that pressure. Minor loss coefficient values are found in "Fluid Mechanics" by Frank White [51].
To calculate the overall pressure drop, the air channel is divided into multiple sections: inlet, diffuser, bend to horizontal and heat exchanger. Everything except the heat exchanger is exactly mirrored on the downstream side, but since flow direction matters for the loss coefficients, they have to be calculated separately. The total pressure drop is found by adding all segmented pressure drops.

$$\Delta p_{total} = \Delta p_{inlet} + \Delta p_{outlet} + \Delta p_{diff,inlet} + \Delta p_{diff,outlet} + \Delta p_{elbow} + \Delta p_{cooling}$$
$$= 81 + 77 + 51 + 11 + 3.6 \cdot 10^2 + 6.6 \cdot 10^3 = 7.2 \cdot 10^3 \text{Pa} \quad (4.22)$$

All elements except the heat exchanger only contribute to 8% of the overall pressure drop. This is the desired outcome, since the overall pressure drop should be as low as possible to save pumping power, but a high pressure drop over the heat exchanger indicates a highly interrupted air flow, creating turbulence and thereby increasing the heat transfer coefficient.

4.5.3. Flex-on-substrate assembly

Now that the heating element temperature can be controlled, it is investigated how the temperature propegates through the FOS assembly. This is done using the unsteady thermodynamic model developed by Sun et al. [61]. It is implemented in MATLAB for an assembly consisting of a Kapton flex circuit, an ACA adhesive layer and an FR-4 PCB. An overview of the material properties is given in table 4.1. There are Dirichlet boundary conditions on the top and bottom of the assembly: 200 °C on the top of the Kapton layer and 20 °C at the bottom of the PCB. There is also a Neumann boundary condition of zero flux at the bottom of the PCB, assuming that the PCB has enough heat capacity so that the bottom never changes temperature. In figure 4.9 the resulting temperature response is shown, along with the temporal response at the center of the ACA layer, which is the most relevant temperature in the curing process. In the right graph it can be seen that the ACA center temperature reaches 90% of its final value (195 °C) after approximately 0.25 seconds. This shows that a temperature of 200 °C is enough for the ACA layer to reach the required curing temperature of 180 °C quickly. In the left graph it can be noted that the temperature distribution over the ACA layer has a maximum difference of 1.4% of the average layer temperature, which means that the degree of cure will also be uniform over the height. After reaching 90% of the final temperature, the temperature difference between the top and bottom of the ACA layer is 2.3 °C and will be even lower when a profile is applied where the temperature increases from room temperature to 200 °C. An elaborate derivation of the model can be found in appendix C.

Material	Thermal conductivity (W/mK)	Density (kg/m^3)	Specific heat capacity (J/kgK)
Flex [62]	0.12	1420	1090
ACA [63]	3.6	2300	1400
PCB [64]	0.29	1900	1150

Table 4.1: Material properties of the three layers of an FOS assembly

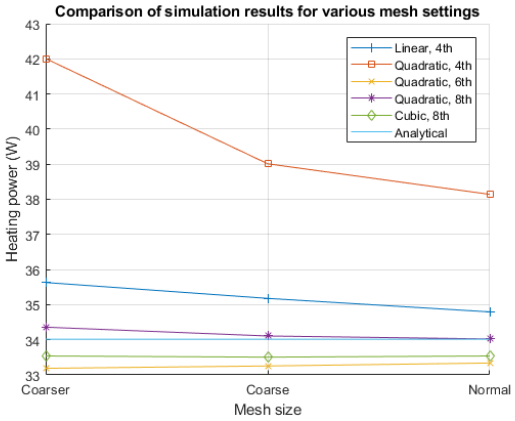

Figure 4.10: Results of the heating power per mesh size, element order and direct area integration order. It can be seen that the result converges close to the analytical result.

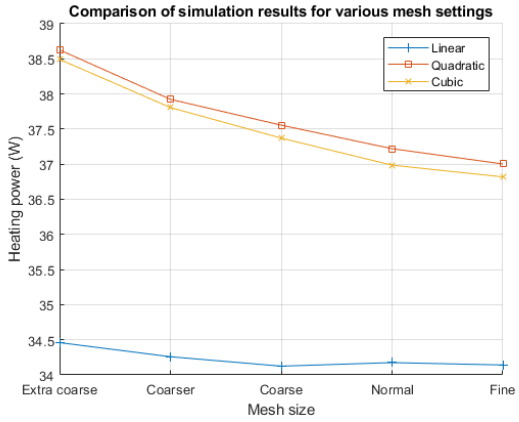

Figure 4.11: Results of the heating power per mesh size. It can be seen that the result converges close to the asmyptote and a normal mesh size with quadratic elements gives reliable results.

4.6. Finite element performance evaluation

For more accurate models of the heating and cooling processes, some assumptions must be eliminated which goes beyond the power of analytical models. Therefore, finite element analysis (FEA) is used to which the analytical models provide a means of verification. The models are created in COMSOL Multiphysics 5.5.

4.6.1. Heating

The difficulty of the heating model is mainly in the heat transfer inside the heating element and the calculation of view factors. Solving the heat equation analytically in three dimensions is a time consuming process if at all possible. Therefore, it was previously approximated by a linear representation (section 4.5.1). In COMSOL the nonlinear temperature progression and complex geometries are taken into account, giving a more detailed result. View factors can be derived from lookup tables and various analogies, but when more than one surface in a group of surfaces has a complex geometry, it is difficult to properly apply those rules and analogies to find the right view factor. Moreover, taking shadowing effects into account is difficult without the use of numerical tools.

To verify the COMSOL model, the analytical model is first replicated. This predominantly means that the cylindrical features are omitted so that a flat heating element surface remains. This is done by creating a new geometry, which consists only of the cavity, the flat heating element surface and a top lid to prevent radiation from escaping the cavity. This lid has the same emissivity as the reflecting side walls. The filament is modeled as a solid block floating in the cavity. All materials are the same as in the analytical model, as well as the temperature of the filament. By default, the view factors are computed according to the hemicube method, which analyzes the view factor of projections in 5 different directions (it cannot 'see' backwards) [65]. The main advantage of this method is the inclusion of so-called 'shadowing effects', where a component blocks the projection between two surfaces, e.g. the filament partially blocks the projection from the collector to the top lid and vice versa. The other available method is direct area integration (DAI) [65]. This is known for its lower computational cost, at the cost of not accounting for the shadowing effects. Shadowing effects

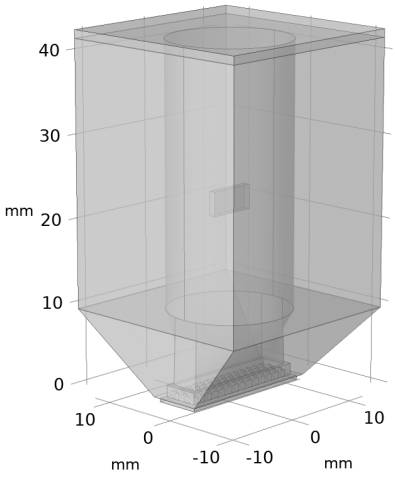

Figure 4.12: 3D finite element model of the heating system.

were neglected in the analytical model because they are virtually impossible to take into account, so in this case the direct area integration method is desired. Since the shadowing by the filament and pillars influences the heat transfer, it is decided to use the hemicube method for the final model.

An important part of the verification of the COMSOL model is the convergence analysis. There are various parameters that can lead to an increase in accuracy of the result at the cost of computational power, so a proper combination must be found that minimizes the error whilst maintaining the lowest possible computing power. The adjustable parameters are: element size, element order and direct area integration order. Normally the temperature element order can also be an influential parameter in heat transfer problems, but this problem is governed by radiation and it is verified that temperature element order does not contribute in the mesh convergence. The results for each mesh size and for various integration orders are plotted in figure 4.10, which shows a converging nature of the mesh refinement. The finest mesh in this graph returns a 1.4% offset from the analytical value.

After the verification step, the COMSOL model can be expanded to simulate the actual module in more detail. This entails the addition of the convection tubes to the heating element. The new model is illustrated in figure 4.12. As mentioned before, the expanded model uses the hemicube method instead of the DAI method to calculate view factors. Because of this different method and the fact that some geometries have become more complex, a new convergence analysis is necessary. In the hemicube model, the refinable parameter is radiation resolution. The default is 256, which means that the sphere around the node is split up into 256 segments. It can be increased or decreased by a factor 2 per step. It has been found that this resolution has a negligible influence on the result. The other parameters remain the same. Again, a convergence analysis is performed, this time to make sure the used settings give accurate results with minimum computing time. The results can be seen in figure 4.11. A normal mesh with quadratic elements is from here on used to present performance results, which has a 1-2% error compared to the cubic result, but a lower computation time.

In figure 4.13, the temperature over the diagonal between opposite corners of the press surface is plotted as a function of time. As temperature rises, the distribution becomes more non-uniform, up to the point where it is almost 15 °C at 200 °C. However, when the lamp power is reduced after 0.7 seconds, the temperature quickly spreads out to achieve a uniform distribution. The temperature non-uniformity is within the required boundaries after 0.3 seconds. The maximum cooling rate is $2.5 \cdot 10^2$ °C/s. This is lower than expected, because the time it takes for the temperature to reach the press surface had not been taken into ac-

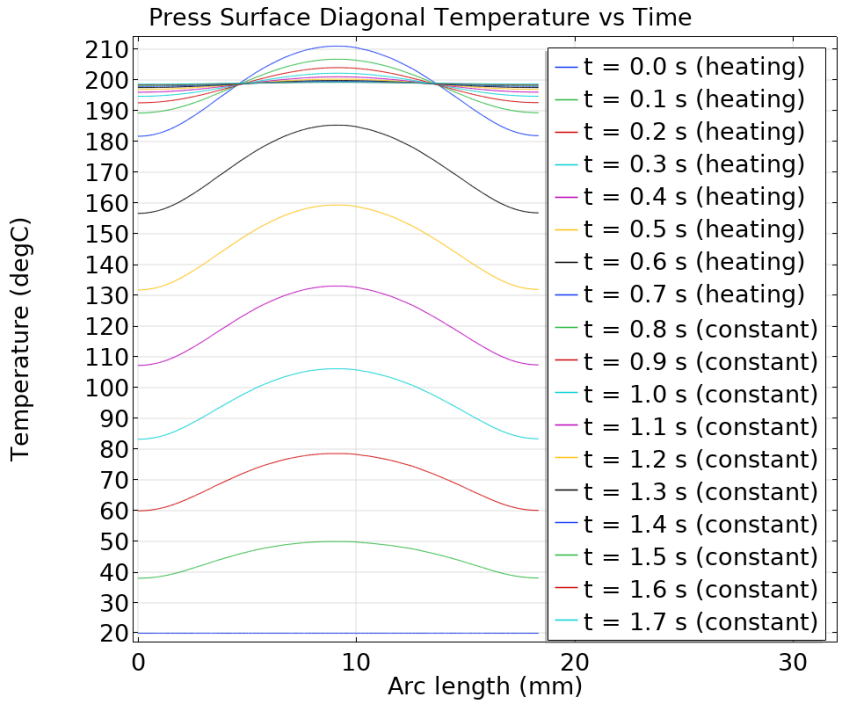

Figure 4.13: Temperature over the diagonal between opposite corners of the press surface as a function of time while heating for 0.7 seconds and then maintaining a constant temperature for 1 second.

count previously. This rate is below the requirement of 300 °C/s, but forms a good starting point for the demonstrator.

The performance of the heating system has been evaluated with a 3D finite element model. It shows good similarity with the analytical model. The heating rate of $2.5 \cdot 10^2$ °C/s is below the requirement, but forms a good starting point for the demonstrator. The maximum temperature variation is 15 °C, which quickly recovers when the constant temperature step initiates. It is expected that this will have minor influence on the cure uniformity.

4.6.2. Cooling system

The challenging part of the cooling model is mainly in the fluid mechanics and the local heat transfer information. Analytical models for fluid mechanics problems are mostly based on empirical relations that are valid under certain conditions, e.g. a range of Reynolds numbers. Even though the geometry in this cooling system is similar to the ones documented in literature, FEA will give more specific information about this system. The empirical relations make it more challenging to verify the analytical calculations, because the model cannot be built up step by step; the analytical model describes a turbulent flow so comparing it with a finite element model of a laminar flow will only provide a baseline.
To save computational cost, the COMSOL model consists of the smallest possible segment of the heat exchanger while still being representative of the real situation. This segment is cut off at the center of two adjacent rows of cylinders over the full flow length, see figure 4.14.

From the analytical model it follows that a flow velocity of 30 m/s is required to reach the cooling power requirement. This corresponds to a pressure drop of 6.6 kPa over the heat exchanger, which is entered in COMSOL. The turbulence model is chosen based on information from COMSOL [66]. It is decided that k-ω is the most suitable model considering both accuracy and computational cost.

In computational fluid dynamics, the element order can be adjusted for velocity and pressure, e.g. P1+P1 means linear velocity and linear pressure, P2+P1 means quadratic velocity

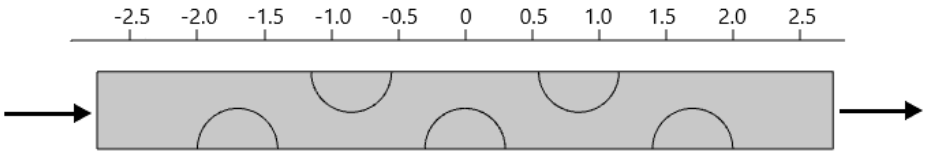

Figure 4.14: 2D model of the heat exchanger, represented by the smallest possible segment. The arrows indicate the flow direction.

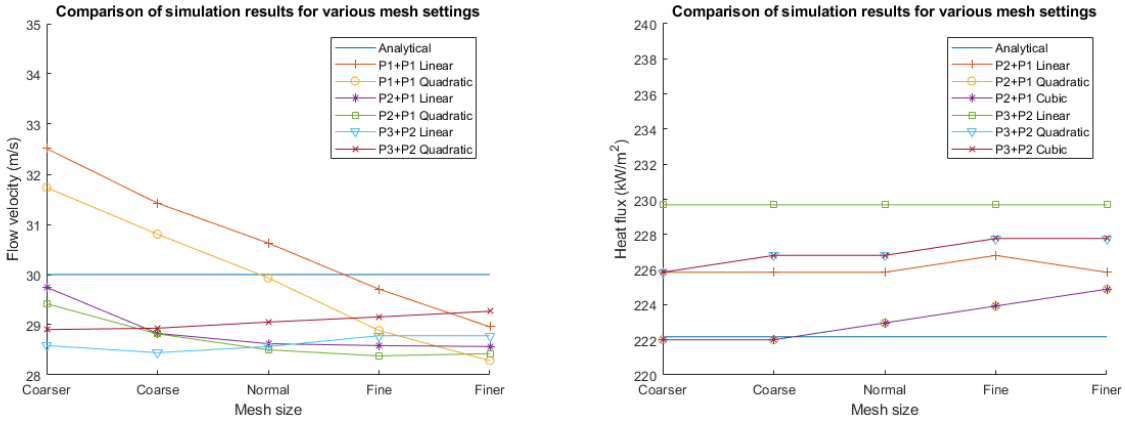

(a) (b)

Figure 4.15: Convergence analysis of the average velocity (a) and heat flux (b) for various combinations of mesh settings.

and linear pressure [67]. In heat transfer, the element size can also be linear, quadratic and cubic. The investigated mesh sizes are coarser, coarse, normal, fine and finer. For flow velocity it appeared that quadratic and cubic temperature elements give the same results, so only linear and quadratic elements are evaluated for each mesh size. For heat flux it appeared that all element orders are relevant and are therefore taken into consideration. In general, the pressure element order is less influential and therefore only P1+P1, P2+P1 and P3+P2 are investigated. The results of separate convergence analyses for each parameter are shown in figure 4.15.

In figure 4.15a it can be seen that the simulated flow rate of $29\,\mathrm{m/s}$ is slightly lower than the analytically designed flow rate of $30\,\mathrm{m/s}$. The remarkable difference in the analytical model with the pressure drop calculation and the heat transfer calculation is the correction factor in the Nusselt number expression due to the fact that the flow is strongly influenced by the first 5 to 10 rows of tubes [52]. This would suggests that the pressure drop is also not linearly dependent on the number of tubes rows, when the number of rows is below 10. Reasoning that the pressure drop should be relatively higher after the first few tubes because the flow is more severely disturbed upon entrance, this hypothesis is verified by dividing the pressure drop by the correction factor C2. The result can be seen in figure 4.16, which shows that the analytical value is now much closer to the simulated results. The corrected pressure drop over the heat exchanger is $7.2\,\mathrm{kPa}$ and the pressure drop over the full cooling system is $7.7\,\mathrm{kPa}$.

In figure 4.15b the results of the average heat flux over all tubes are compared with the analytical result. It can be seen that the simulation results converge to $2.3 \cdot 10^2 \mathrm{kW/m^2}$, whereas the analytical result is $2.2 \cdot 10^2 \mathrm{kW/m^2}$. This difference of $\sim 1.7\%$ is equal to the difference in flow velocity and is most likely due to the turbulence modeling, in which various parameters are estimated by COMSOL.

The 2D model does not provide information on the temperature distribution over the heating element and the temperature profile over time. Modeling turbulent flow in 3D is a computa-

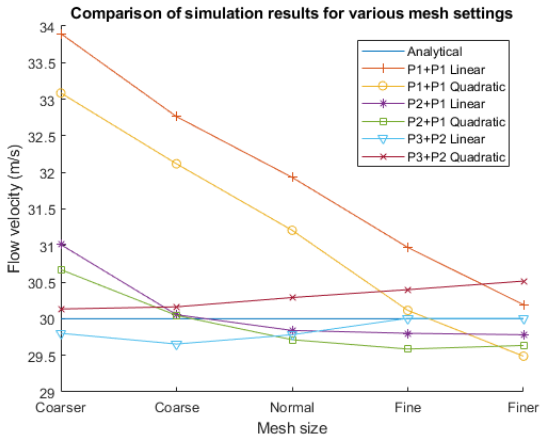

Figure 4.16: Convergence analysis of the average velocity with updated pressure drop value due to adjustments in the analytical model.

tionally expensive task. The combination of 3 dimensions, conjugate heat transfer, multiple physics and turbulence drives up the computational cost more than what is possible with the available computers. A 3D model of the turbulent convective heat transfer has therefore not been successfully analyzed and it is advised to develop this model in future work to obtain information about the temperature response of the heating element during cooling.

Instead, a 3D model is made with only heat transfer in solids and standard equations for convective heat flux over a cylinder in cross flow and a flat plate. The temperature around each tube is taken from the result of the 2D model and the average heat flux of all tubes is the same as in the 2D model. An illustration of the 3D model can be seen in figure 4.17. A transient analysis is performed from 0 to 1.5 seconds and all results with an average temperature above $100\,°C$ are considered. The temperature crosses $100\,°C$ after 1.1 seconds. In figure 4.18 the temperature distribution over a diagonal line on the bottom surface (press surface) is plotted. The asymmetry is due to the asymmetric tube configuration. It can be seen that the temperature variation is low, at most $1\,°C$ after 1.1 seconds. Since the maximum cooling rate is $1.4 \cdot 10^2 °C/s$, this means that the real temperature variation of the heating element during cooling at $150\,°C/s$ will not exceed the requirement of $5\,°C$.

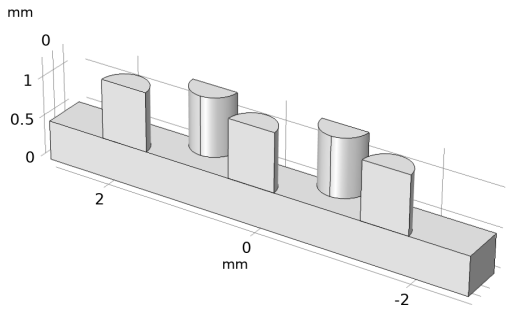

Figure 4.17: Illustration of the 3D cooling system model.

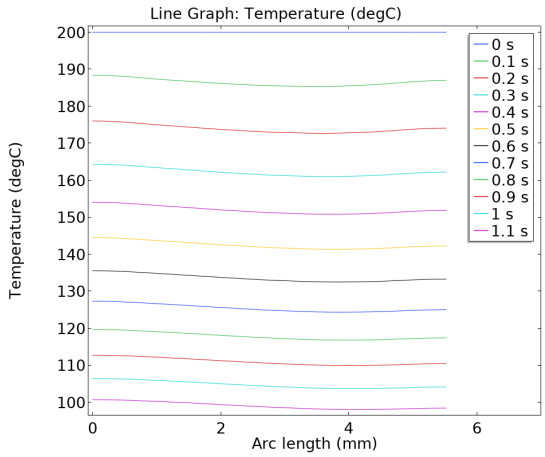

Figure 4.18: Temperature distribution over the press surface vs time. The distribution has a non-uniformity of less than $1\,°C$ at all times, which is within the requirement.

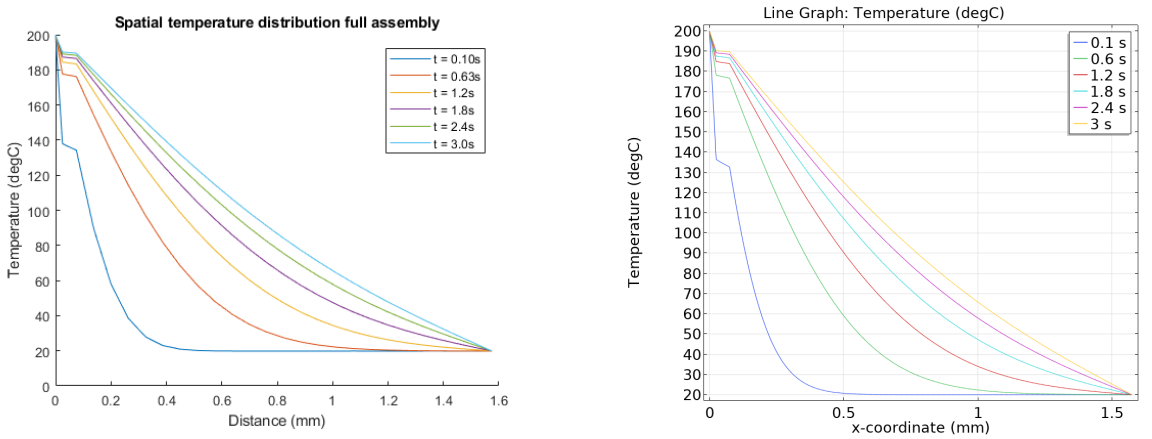

Figure 4.19: Analytical (a) and numerical (b) results for the temperature distribution over the FOS assembly at various points in time. Both graphs are identical, thus verifying the numerical model.

The cooling system performance has been evaluated with a 2D and 3D finite element model. Although a successful 3D simulation of the turbulent convection has yet to be made, a coarser model with estimated heat transfer coefficients is simulated to get an idea of the temperature distribution over the press surface. The maximum cooling rate is $1.4 \cdot 10^2 °C/s$, which is below the requirement. However, it is expected that the real system will perform better by taking turbulence into account, an important mechanism in this cooling system.

4.6.3. Flex-on-substrate assembly

In section 4.5.3 a temperature profile was plotted for the flex-on-substrate assembly consisting of a Kapton flex circuit, ACA layer and FR-4 PCB. The material properties of the ACA layer were obtained by combining the epoxy material and the conductive particles in their relative volume fracture. In reality, the particles float freely in the adhesive and there are electrodes that conduct heat better than the epoxy. To compute this, an FEA model is created.

First, a model similar to the analytical model is made. This consists of a 1D line segment as described above with the material properties and boundary conditions from section 4.5.3. The comparison with the analytical results in figure 4.19 shows that they are exactly identical, which was achieved thanks to the simplicity of the finite element model. However, to obtain meaningful results from the analysis, it has to be expanded to 2D.

The 2D model incorporates the gold and copper electrodes and the conductive particles as separate bodies, which creates low and high thermally conductive paths through the ACA. The 2D model is shown in figure 4.20. It should be noted that the PCB layer is partially cut off for clear illustration purposes, but is in fact 1.5 mm thick.

The conductive particles are distributed randomly over the ACA, but the amount is based on a particle density reported by Hitachi Chemical, which is then converted to an amount of condcutive particles per unit width [68]. The top electrode, belonging to the flex circuit, is made of gold and the bottom electrode, belonging to the PCB, is made of copper. The electrodes in combination with the conductive particles create a path that conducts heat well. Another path, which crosses no metal body and thus only epoxy, has a lower conductivity.

In this analysis, the top temperature is a ramp function that goes from 20 °C to 200 °C with a slope of 300 °C/s, in 0.60 s. When the temperature of 200 °C is reached, it stays constant. The bottom temperature is undefined, as it does not necessarily remain at room temperature. However, in reality the PCB is much larger than the FOS joint, so the bottom temperature might not be affected during assembly.

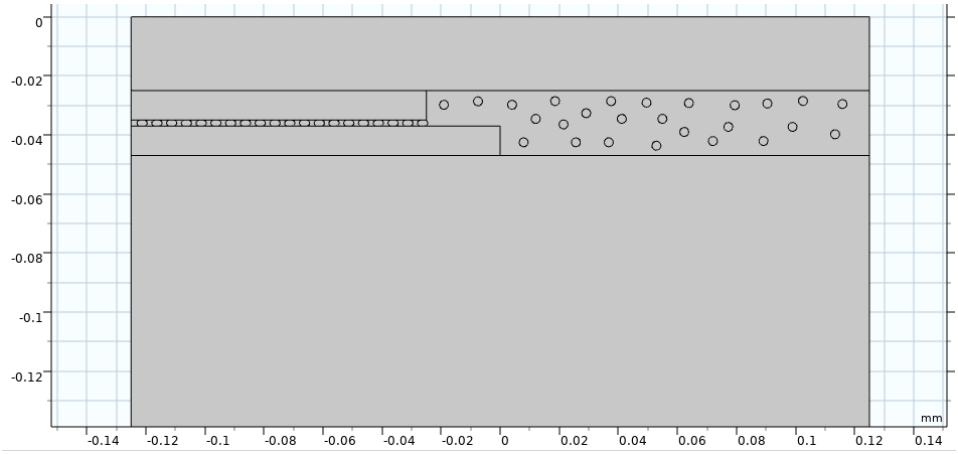

Figure 4.20: Illustration of the FOS assembly geometry in 2D. The top layer is made of Kapton. The middle layer, the ACA, consists of the epoxy adhesive itself, a gold electrode at the left top, a copper electrode at the left bottom and nickel conductive particles, some of which are trapped between the electrodes. The PCB layer is partially cut off to be able to show the ACA structure, but is in fact 1.5 mm thick.

The temperature distribution over the high conductivity (through the electrodes) and low conductivity (through the adhesive) paths is plotted in figure 4.21. The first thing to be noted is the fact that the temperature in the Kapton layer drops quicker in the high conductivity path. Since heat is more easily extracted from the Kapton layer via the electrodes, this gives the Kapton layer less opportunity to heat up. In the low conductivity path, heat is better isolated in the Kapton layer, giving it more opportunity to heat up.

In the ACA layer itself, it can be seen that the temperature drops more in the low conductivity path, which is conform the expectations. The temperature drop is higher than in the 1D simulation, because the 1D ACA layer is a mix of epoxy and metals, thus having a higher thermal conductivity. The temperature drop is approximately 7 °C over the low conductivity path. This means that the top of the ACA layer, which has roughly the same temperature as the top of the Kapton layer, must be 7 °C higher than the required curing temperature. Also, the ACA will be cured faster at the top than at the bottom, at least for the brief moment until the lower part has reached the same temperature. In the horizontal direction, the temperature difference is approximately 6 °C at the bottom and 1 °C at the top. At an absolute temperature of 180 °C, the non-uniformity in any direction is thus always lower than 2%.

This analysis gives an idea of how the temperature propagates into the FOS assembly. With this information, the process temperature of the bonding module can be determined. The analysis also provides information on the horizontal and vertical variance in the degree of cure, based on the temperature non-uniformity. The non-uniformity is better than 2%, which will likely not give severe discrepancies in the local joint quality.

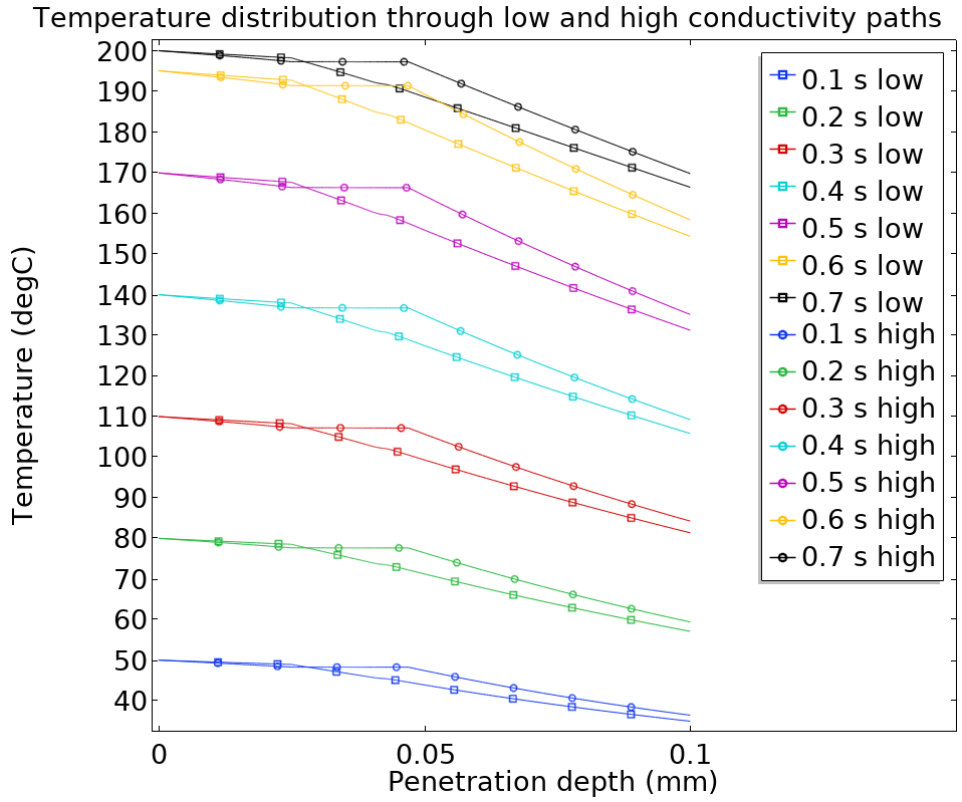

Figure 4.21: Temperature distribution in the FOS assembly through a path of high thermal conductivity and a path of low thermal conductivity. In the low conductivity path, the top and bottom temperature of the ACA layer (between 0.025 and 0.05mm) are approximately 10 °C apart, meaning that the ACA will cure asymmetrically.

5

Experimental methods

To validate the models presented in chapter 4, a proof-of-principle demonstrator is fabricated and the heating and cooling systems are characterized. First, the fabrication of the test setup is discussed. This consists of manufacturing and assembly of the bonding module. Consequently, the calibration of the temperature sensor is reported. Lastly, the experiment procedure is described in detail.

5.1. Demonstrator

The demonstrator consists of the bonding module, the electrical wiring and a pneumatic system to supply pressurized air to the cooling system. Fabrication, assembly and measurements are discussed in this section.

5.1.1. Fabrication

The module consists of multiple parts that have different manufacturing methods, due to their different levels of complexity and requirements. The main body, the stainless steel block that holds the radiation cavity and cooling channels, is split into two halves, to be able to properly fabricate the cooling channels. They are bolted together with four M5 bolts, two on each side. Due to the complex shapes and small features, it was decided that metal 3D printing is the most suitable manufacturing method for this component. The chosen material is Stainless Steel 316L, which has a tolerance of $\pm 0.2\,\mathrm{mm}$. The heating element is also 3D printed, because it is too small to be cost-efficient for electric discharge machining (EDM). It is made of AlSi10Mg, an aluminium alloy well known to be used in 3D printing, that is resistant to temperatures of up to $300\,^{\circ}\mathrm{C}$ [60]. With higher production numbers, EDM might be a better option because of higher tolerance and more freedom of material choice. The top plate and bracket that connect the module with the portal are milled out of Stainless Steel 304 and the D263T glass plate is cut to size by the distributor.

The assembly starts with the preparation of the main body. The reflector surface is coated with Tesa 60670 aluminium tape, that is specifically meant for radiation reflection and can withstand temperatures of $160\,^{\circ}\mathrm{C}$ max [69]. It has a reflectance of 80%, which is lower than the designed reflectance [48]. However, for this demonstrator it was unfeasible to polish the reflecting surface and coat it with silver or gold to reach the target 95%. The aluminium tape is expected to give an insight into the performance of the heating system, which can then be extrapolated to a better reflecting surface.
After coating, the two halves are bolted together to form the full main body. The glass plate is cleaned with isopropyl alcohol to make sure that skin grease and other infrared-absorbing contaminants are removed, and then inserted into the main body with a pair of tweezers. The glass plate is form-closed with slight play, but it is allowed to slide around as long as it does not let air escape into the radiation cavity. The heating element is bonded to the main body with a low viscosity adhesive called Epo-Tek 353ND-T. It is dispensed with a syringe and

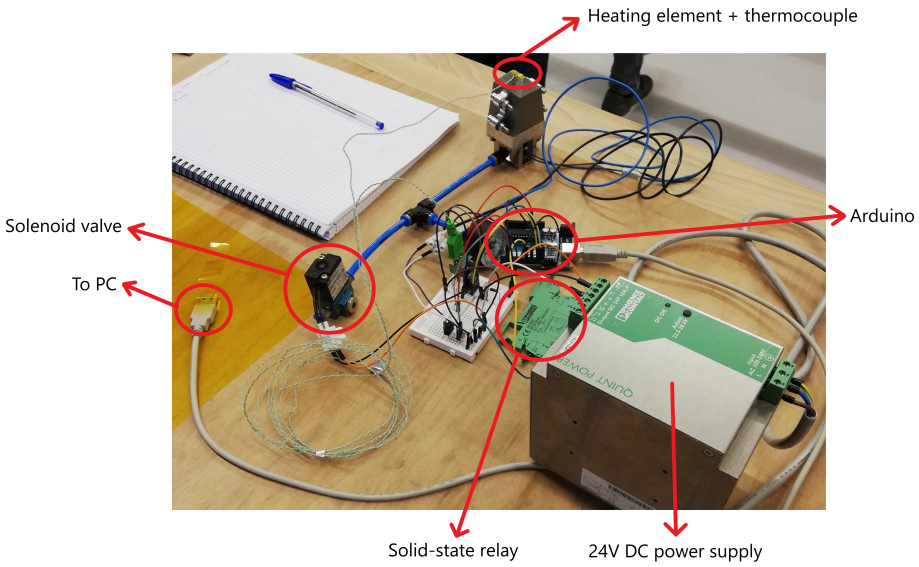

Figure 5.1: Bonding module experimental setup with component descriptions.

needle to make sure it is only applied where desired, and then cured in an oven for 1 hour at 150 °C. The choice for a low-viscosity adhesive is to prevent adhesive to flow into the cooling channels or heat exchanger array and obstruct the air flow. After the epoxy is cured, the top plate with pre-assembled pneumatic push-in connectors, lamp holder and light bulb is put in place with the interface bracket on top. Lastly the module is connected to the electronic circuit and the pneumatic system. It is decided to not install it into the portal during testing for better accessibility. A photograph of the experimental setup is shown in figure 5.1.

5.1.2. Temperature sensor calibration

A thermocouple is chosen for the temperature measurement of the heating element for its small size (fast response time and attachment benefit) and good usability. However, thermocouples also tend to have a higher measurement uncertainty than other temperature sensors due to the large amplification in combination with small electromagnetic noise. Therefore, the thermocouple is calibrated using a IKA RCT basic heating plate and a FLIR E4 thermographic camera. A patch of Kapton tape is stuck to the heating plate surface to increase its emissivity to 0.77, which is necessary for reliable measurements of the thermographic camera [48]. The thermocouple is also held in place with Kapton tape, which has the advantage of being stable at high temperature [62].

The range of interest is between 20 and 200 °C, which is divided into steps of approximately 25 °C. The temperature is measured by both the thermographic camera and the thermocouple for 5 seconds for each temperature step, in five independent calibration procedures. The independence is realized by allowing the heating plate to cool down for 2 hours. From each calibration procedure, the mean and standard deviation are taken. The mean is then compared to the value measured on the thermographic camera, which has an uncertainty of ±1%. Since the thermocouple has a linear voltage-temperature relation, the comparison with the thermographic camera leads to a sensitivity error and a systematic error.
The average standard deviation is $\sigma = 0.45\,°C$, so the accuracy with 95% confidence is $s_T = 2\sigma = 0.90\,°C$. The average error due to noise is 1.56 °C and the resolution is 0.32 °C/bit. The total uncertainty is thus $u_T = \sqrt{0.45^2 + 1.56^2 + 0.32^2 + 1^2} = 2.0\,°C$.

The thermocouple also has a delay in its response to a temperature change. This is partially due to the thermal inertia but it mostly depends on how well the thermocouple makes contact with the surface of interest. The appropriate time constant τ is calculated as in equa-

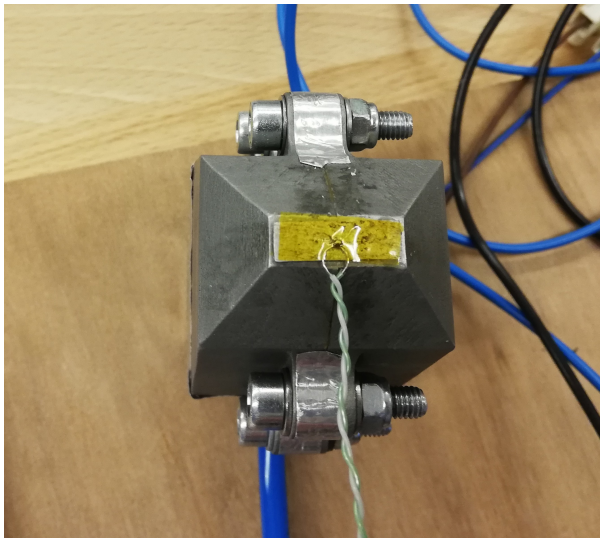

Figure 5.2: The thermocouple is attached to the heating element with Kapton tape.

tion 5.1, where R_c is the thermal contact resistance, m is the thermocouple mass and c is the thermocouple specific heat capacity. All three of these values are difficult to measure, so instead the time constant is determined directly. This is done by heating the heating plate to 200 °C and applying the thermocouple to its surface until settled (~ 3 seconds). After 10 measurements, the average temperature profile is calculated and the time constant is calculated by equation 5.2, where n denotes the ratio between the current temperature and the equilibrium temperature and rise time to 50% and 90% of the final value are chosen for the calculation to eliminate the electrical transience at startup. The measured time constant is 0.40 ± 0.04s. This is later used to estimate the real temperature profile from the measurements.

$$\tau = mcR_c \tag{5.1}$$

$$\begin{aligned} t_n &= -\tau \log\left((1-n)\frac{T_0}{T_0 - T_\infty}\right) \\ \rightarrow t_{0.9} - t_{0.5} &= -\tau\left(\log\left((1-0.9)\frac{T_0}{T_0 - T_\infty}\right) - \log\left((1-0.5)\frac{T_0}{T_0 - T_\infty}\right)\right) = \tau \log\left(\frac{0.5}{0.1}\right) \\ \rightarrow \tau &= \frac{t_{0.9} - t_{0.5}}{\log(5)} \end{aligned} \tag{5.2}$$

5.1.3. Air flow measurements

The pressurized air is supplied from the wall supply in the lab. This is 6 bar and has a analogue pressure regulator. As calculated in section 4.5.2 and 4.6.2 the pressure drop over the cooling system should be 7.2 kPa. However, minor losses are also present in the solenoid valve and pressure regulator, which are unknown. These minor losses can be measured by letting air flow through the system and measuring the volume flow rate, for instance by measuring the outlet velocity and cross-sectional area.

Flow velocity can be measured in various ways, including coriolis, ultrasonic, vortex generator and positive displacement measuring devices. Unfortunately, most flow meters are expensive and sometimes even custom made. It is therefore decided to use a vane anemometer, which bases the flow velocity on the rotational speed of a turbine. This measurement device is generally used for measuring air flows over a large area, e.g. wind speed. Since the cooling system outlet is much smaller than the turbine, this complicates the measurement. A conversion factor is calculated based on the ratio between the cooling system outlet

area and the turbine area, and their influence on the measured velocity, which is stated in equation 5.3 [51]. Subscript m here stands for measured, subscript r stands for real.

$$P = \frac{1}{2}\rho A V^3 \rightarrow V \propto A^{-1/3} \rightarrow \frac{V_r}{V_m} \propto \left(\frac{A_m}{A_r}\right)^{1/3} \tag{5.3}$$

Furthermore, the position of the anemometer with respect to the air flow is important for correct velocity measurement. Since the device is handheld, a perfect alignment of the turbine with the flow direction cannot be guaranteed. A 10° alignment error, which manual alignment can certainly achieve, gives a 1.5% velocity error. Crosswise location of the turbine with respect to the air flow is important for correction measurement, because the turbine has a spanwise variation of the lift coefficient. In other words, on the perimeter, the lift coefficient is different from closer to the center. Aligning the flow axis with the turbine axis is desired, but the shaft itself is comparable in size with the air flow, which means that all air would be blocked. Therefore, the flow is shifted to the side of the turbine. The spanwise variation of velocity has been found to be approximately 30% of the velocity between the center and perimeter at the same streamwise location. The measured mean velocity was 5.6 m/s, which corresponds to 30 m/s real velocity according to equation 5.3. A 30% variation means that the velocity measurement can only be an indication for the proof-of-concept, and a better flow measurement device should be used in further investigations.

This flow measurement method did not lead to a successful characterization of the minor losses in the pneumatic system, most likely because there are many more sources of pressure loss than those two main sources. Therefore, it is decided to directly measure the outlet airflow from the cooling system and adjusting the pressure regulation knob until the desired velocity is reached. The supply pressure is regulated such that the cooling system outlet velocity induces a mean measured velocity of 5.6 ± 1.7 m/s, the equivalent of 30 m/s real velocity.

5.2. Experiment procedure

The goal of the experiment is to validate the models made for heating and cooling of the heating element. The heating model simulates a radiation source irradiating the heating element and the cooling model simulates a forced airflow flowing across the heat exchanger. In both cases, the heating element is free in the environment. It is assumed that natural convection and radiation to the environment can be neglected, so that heat only flows from the radiation source to the heating element, as shown in equation 5.4, and from the heating element to the cooling fluid.

$$\begin{aligned} A &= 0.5 \cdot 10^{-3} \cdot 2\left(17.5 \cdot 10^{-3} + 5.5 \cdot 10^{-3}\right) = 23\,\text{mm}^2 \\ Q_{convection} &= h_c A_c \Delta T < 5 \cdot 23 \cdot 10^{-6} \cdot (200 - 20) = 0.021\,\text{W} \\ Q_{radiation} &= \sigma A_r \left(T_{he}^4 - T_e^4\right) < 5.67 \cdot 10^{-8} \cdot 23 \cdot 10^{-6} \cdot \left(473^4 - 293^4\right) = 0.056\,\text{W} \\ Q_{loss,total} &= Q_{convection} + Q_{radiation} < 0.021 + 0.056 = 0.077\,\text{W} \\ \frac{Q_{loss,total}}{Q_{heating}} &< \frac{0.077}{34} \times 100\% = 0.23\% \end{aligned} \tag{5.4}$$

The thermocouple is attached to the press surface, which is the surface of interest. It is secured with Kapton tape like in the calibration, see figure 5.2. The temperature is fed back to the controller and is logged for later analysis. The temperature reference is a typical ACA bonding temperature profile: heating to 200 °C, 5 seconds at peak temperature to simulate curing and then cooling until below 100 °C [26]. The 5 second constant temperature period starts after the surface has reached the correct temperature, not when the heating process starts. This profile is illustrated in figure 5.3. Note that the real system has a longer cycle time because it takes longer to reach the initiation temperature and cool down afterwards.

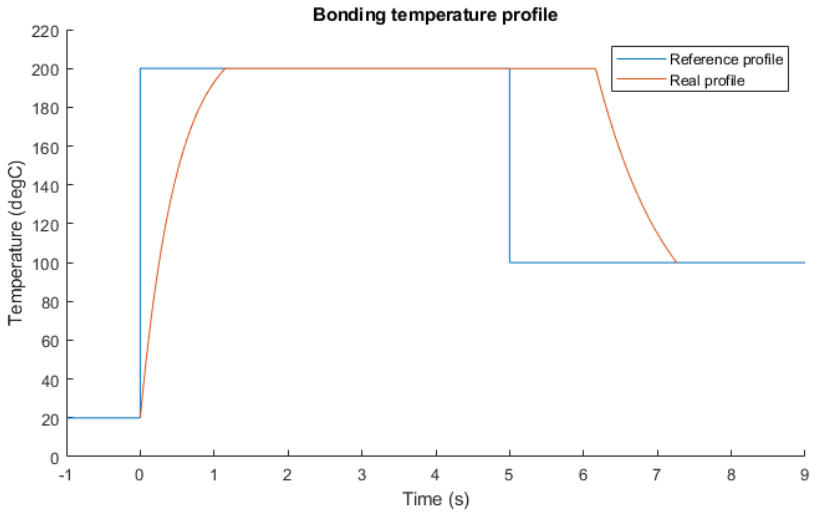

Figure 5.3: Temperature profile used for the experiment and estimated system response. Heating at maximum power to 200 °C, 5 seconds at peak temperature, cooling to below 100 °C [26]. The real cycle time is longer due to the heating and cooling steps, while the constant temperature period must still be 5 seconds.

5.3. Arduino controller

To control the module and make sure the temperature reference is followed, an Arduino controller is designed, as well as an electric circuit that connects the electronic components to one another. A flow chart of the Arduino control sequence is depicted in figure 5.4. The Arduino used is an Arduino Uno.

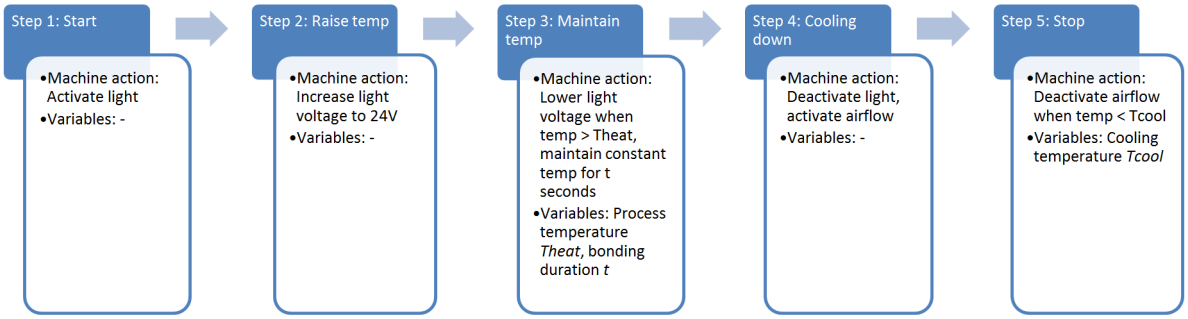

Figure 5.4: Flow chart of Arduino control sequence. Blue blocks contain the bonding process steps, white blocks contain actions required from machine and the variables of interest for this step

5.3.1. Electrical design

Several subsystems can be identified in the electrical circuit. There is a heating system, with the halogen lamp as actuator, a cooling system, with a solenoid valve as actuator and a thermocouple to measure the temperature in both cases. A circuit diagram is available in appendix D

The halogen bulb is a 150W 24V Philips 7158XHP and is connected to an external power supply. The voltage must controllable, for when the heating element temperature is high enough and less heating power is required. There are several ways to dim a halogen lamp. MOSFETs or other transistors can be used to create a pulse width modulated (PWM) signal. This means that the transistor gate is switched such that it is open only for a certain period of time every cycle, therefore reducing the average voltage across the gate depending on the time it is open. This is called the duty cycle, e.g. a duty cycle of 30% is open for 30% of the time and results in 30% of the maximum power, so 45W in this case. A STP55NF06L logic MOSFET was chosen for this circuit based on the requirements for gate voltage, maximum

source current and maximum source voltage. The PWM control will be further discussed in section 5.3.2.

The solenoid valve used to control the airflow, a MAC 35A-AAA-DDAA-1BA, also requires a 24V source. The control of this actuator is more clear because it only needs to switch on and off once per cycle. For this reason, together with the fact that it only consumes 5.4 W when active, it is controlled with a Phoenix Contact 2967989 solid-state relay. The switching voltage is 5V so the relay can be controlled from the Arduino itself.

The last subsystem is the thermocouple. Since thermocouples generate a tiny voltage output (order of mV), an amplifier is needed to convert the thermocouple output to a more convenient voltage to work with. This is done with an Ardafruit MAX6675, for which much documentation is available for implementation and programming. It has a resolution of about 0.25 °C, depending on how it is calibrated. This amplifier also works on 5V and thus can be powered by the Arduino itself.

5.3.2. Code sequence

The assembly process will start with a controlled activation of the light bulb. Since the resistance of tungsten (the filament material) increases with increasing temperature, it is relatively low at room temperature compared to nominal operating temperature, which is 3450 K. The resistance is about 20 times as low at room temperature, so the current is 20 times as high. This high initial current is called an inrush current [46]. This damages the filament, especially so when it is switched on and off repeatedly like in this system.
It is decided to let Arduino control the current so that no extra equipment is needed. This is done by splitting the ”switching-on action” into two equal parts. This means that the inrush currents of the two smaller parts must be equal:

$$I_1 = U_1 \cdot R_{300K} = D \cdot U_2 \cdot R_{300K}$$
$$I_2 = U_2 \cdot R_{Tt} = U_2 \cdot R_{300K} \cdot \frac{R_{Tt}}{R_{300K}}$$
$$I_1 = I_2 \longrightarrow D = \frac{R_{Tt}}{R_{300K}}$$

Here Tt denotes the transition temperature, which is the temperature of the filament between step 1 and 2. Both the current and consumed power at Tt are also known, assuming that power is proportional to T^4 and UI:

$$I_3 = DU \cdot R_{300K} / \frac{R_{Tt}}{R_{300K}} = D^2 U \cdot R_{300K} = P_3 = \frac{150 \cdot \frac{(T_t - 300)^4}{(3450-300)^4}}{DU}$$

$$\text{insert} \quad D = \frac{R_{300K}}{R_{Tt}} \longrightarrow (Tt - 300)^4 \cdot (R_{Tt}/R300K)^3 = \frac{R_{300K} \cdot (3450 - 300)^4}{150} U^2 \approx 1.9 \cdot 10^{14}$$

The electrical resistivity values of tungsten are obtained from the CRC Handbook of Chemistry and Physics[70]. The value in the equation above matches when entering 1700K and its corresponding $\frac{R_{Tt}}{R_{300K}} = 8.28$ which means that the best duty cycle is approximately 12%.

The light bulb is now fully switched on and the thermocouple measures the heating element temperature. Controlled with a PID, the PWM duty cycle decreases as the temperature approaches the desired minimum bonding temperature of 200 °C. The reference temperature is set to 220 °C to make sure it never goes below 200 °C. Also, the center temperature is measured, which is higher than the corner temperature. As soon as the minimum bonding temperature is exceeded, Arduino starts counting to 5 seconds, the simulated bonding duration. When the bonding is completed, the lamp is switched off and the valve is opened to initiate cooling. With the thermocouple still sensing temperature, the valve closes after the heating element temperature is below the cooling temperature. A blinking LED indicates that the process is complete.

6

Results and discussion

In this section, the results from the experiment are presented. A short discussion leads to insights that require another experiment. The results of the second experiment are also presented and discussed. Lastly, the experimental results are compared to the model simulations.

6.1. First measurement

The temperature profile and temperature rate of change are presented in figure 6.1 as a function of time. As expected, the profile resembles the estimated shape in figure 5.3 and the temperature rate of change is highest at low temperature, when heating starts, and lowest at high temperature, when cooling starts. There is a clear distinction between two sets of measurements: seven measurements have a cycle time between 15 and 20 seconds and three measurements between 20 and 25 seconds. Since all conditions were similar in terms of environment, starting temperature (between 30 and 50 °C) and control settings, it is likely the thermal contact between the thermocouple and heating element that was flawed in the three slower cycles and it took more time for the thermocouple to reach the actual heating element temperature. This was solved in the next measurements by applying slight pressure on the thermocouple. Although the three measurements are meaningful in the sense that they show a consistent temperature path, they are marked as incorrect measurements and are not taken into account in statistical calculations, i.e. average heating and cooling rate, standard deviation and average temperature profile.

The average temperature profile is calculated by taking averaging the temperature at each time point. This gives a good result in the heating area, but as soon as the fastest cycle starts cooling, it becomes less meaningful since it calculates the average of six high temperatures and one low temperature. More insight is therefore gained by calculating the maximum heating and cooling rates and averaging those values.
The temperature rate of change is calculated as follows.

$$\frac{\partial T}{\partial t} = \frac{T_{i+1} - T_{i-1}}{2\Delta t} \pm \sqrt{\left(\frac{u_T}{\Delta t}\right)^2 + s_T^2} \tag{6.1}$$

u_T is the temperature measurement uncertainty from chapter 5 and s_T is the standard deviation of the calculated maximum rates at 95% confidence. The maximum heating rate is on average 34 ± 9.9°C/s and the cooling rate $-1.2 \cdot 10^2 \pm 7.7$°C/s.

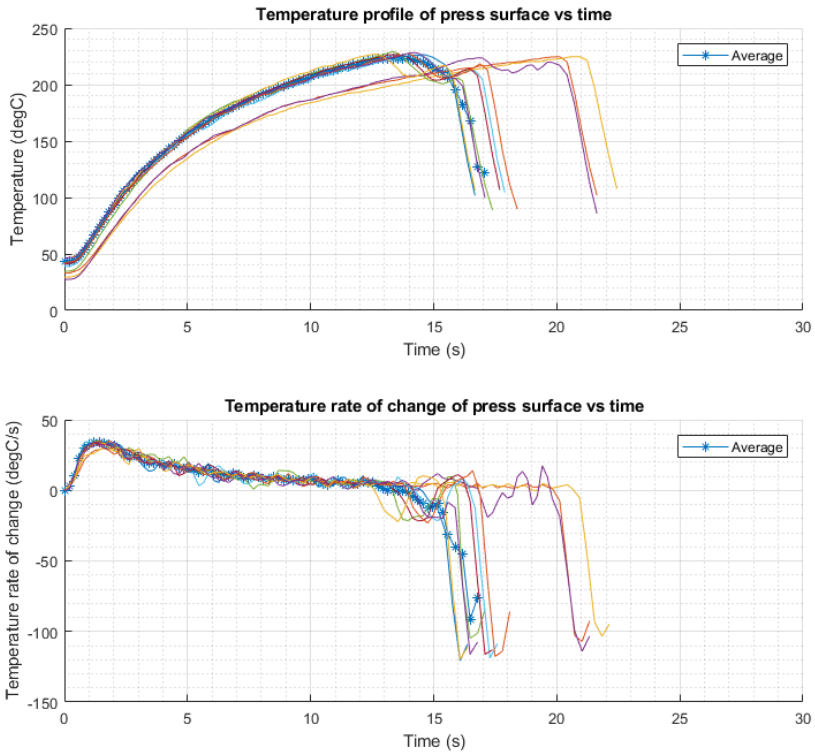

Figure 6.1: Temperature profile and temperature rate of change of the first measurement.

6.1.1. Intermediate discussion

There is no clear relation between the different starting temperatures, caused by gradual temperature buildup in the main body, and cycle time. The difference is maximum 20 °C in an area where this difference is relatively small compared to the heating rate. It can be observed that the lower starting temperature measurements catch up with the higher starting temperature measurements within a few seconds.

Both the maximum heating and cooling rates are lower than designed for, even though the cooling rate is the same as the 3D FEA result. For the cooling system it is difficult to point out why it is not up to the requirement; the leaks in the cooling channels, inaccurate fabrication and difficult flow velocity measurement add uncertainty to the results that makes it difficult to formulate a reliable conclusion. For the heating system, a hypothesis has been formulated to explain the difference with the designed performance. It can be seen that the 220 °C curing temperature is close to the equilibrium temperature of the heating system, as it flattens out. This means there is some energy leak that inhibits the heating element from storing the incoming energy. The problem lies in the adhesive between the heating element and the main body. Even though the two components do not necessarily make good thermal contact, the adhesive acts as a heat bridge that leads the energy away from the heating element.

This hypothesis is supported by measuring the main body outer surface temperature on two locations: near the heating element and higher up, where the most radiation is absorbed by the reflective wall. The temperature reading near the heating element is higher which can only mean that it obtains heat from the heating element.

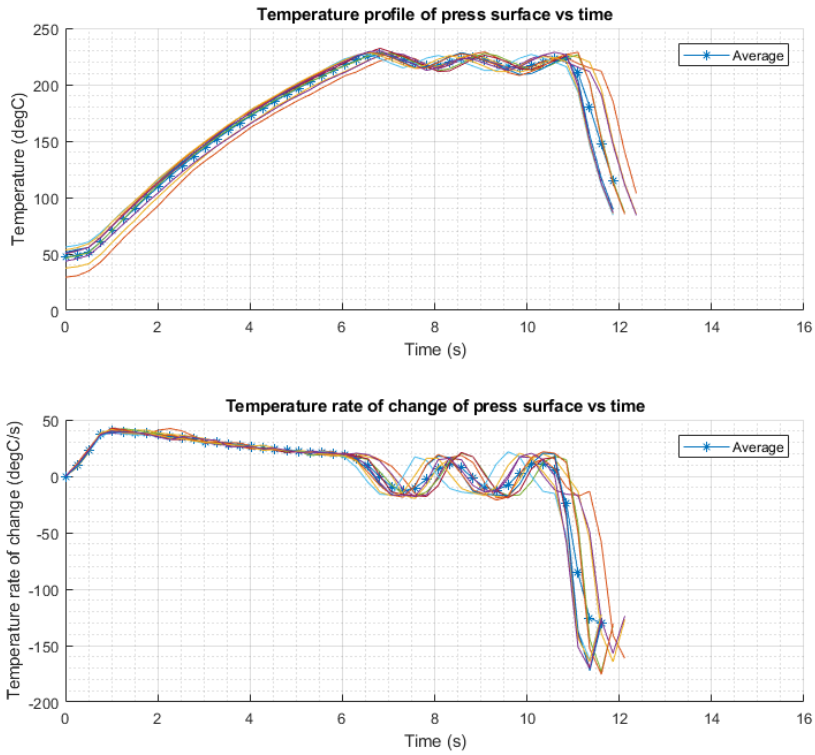

Figure 6.2: Temperature profile and temperature rate of change of the second measurement.

6.2. Improved system measurement

An improved system is made to verify the hypothesis, in which the heating element is only bonded in the corners, rather than over the full perimeter. This should reduce the heat bridge and therefore increase the thermal barrier between the heating element and main body. Strips of Kapton tape are placed between the heating element and main body during fabrication to ensure a gap of $50 - 100\mu m$. The experiment is repeated with the improved system and the results are represented in figure 6.2. The maximum heating rate is now on average $41 \pm 9.9°C/s$ and the maximum cooling rate is $-1.7 \cdot 10^2 \pm 8.7°C/s$.

6.2.1. Discussion

Contrary to the first experiment, there is now a clear relation between starting temperature and cycle time: the lower starting temperature measurements require more time. The overall temperature profile shows that the equilibrium temperature is now well above the curing temperature based on the higher heating rate at 220 °C. The oscillatory behaviour between 7 and 11 seconds is caused by the controller, which tries to keep the temperature between 210 °C and 230 °C. This was not present in the first experiment because the 5 second curing time starts counting when the temperature exceeds 200 °C and it took close to 5 seconds from there for the heating element to reach 230 °C, so it never needed to reduce the input power.

A comparison between the results of the first and second experiments is shown in figure 6.3. It confirms that increasing the thermal contact resistance between the heating element and main body improves the heating performance: the heating rate is higher within the 95% confidence band. The comparison also shows the strong influence of the heating rate on the cycle time: with a 20% higher heating rate, the cycle time is decreased by 30%.

The cooling rate is also consistently higher than in the first experiment, which is contrary to expectations. The thermal barrier was increased by creating a gap between the heating

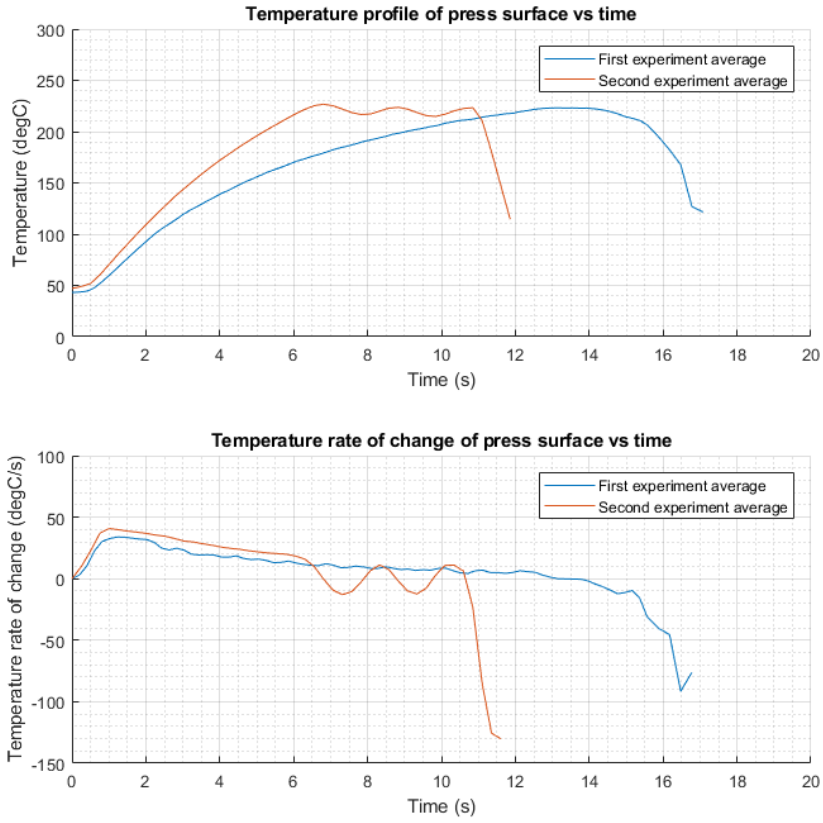

Figure 6.3: Comparison between average temperature profile and temperature rate of change of first and second measurement.

element and main body, which creates more leakage of the cooling channel and less likelihood of the air crossing the heat exchanger. Also, the adhesive heat bridge should have been advantageous for cooling, since the main body withdraws heat from the heating element. The new leaks might be more favourable for the air flow than the other leaks, which essentially means that more air flows along the heating element than before.

In the temperature rate of change graphs (second graph of figures 6.1, 6.2 and 6.3) it can be seen that there is a delay in the ability of the thermocouple to change temperature. This is partially due to the transient response investigated in section 5.1.2, which has been accounted for in figure 6.4, according to equation below.

$$mc\frac{\partial T_{TC}}{\partial t} = \frac{T_{HX}(t) - T_{TC}(t)}{R_{th}}$$

$$\rightarrow mcR_{th}\frac{\partial T_{TC}}{\partial t} = \tau\frac{\partial T_{TC}}{\partial t} = T_{HX}(t) - T_{TC}(t)$$

$$\rightarrow \tau\frac{\partial T_{TC}}{\partial t} + T_{TC}(t) = T_{HX}(t) \quad (6.2)$$

As expected, the estimated real heating and cooling rates are higher than what is measured with the thermocouple: the maximum heating rate is now on average $51 \pm 9.9°C/s$ and the maximum cooling rate is $-2.3 \cdot 10^2 \pm 12°C/s$. The cooling rate is much higher than required, which proves its working potential, but also shows that more research is needed in order to characterize the relation between flow velocity and cooling power. Also, a better attachment of the thermocouple to improve the thermal contact will make the measurements more accurate.

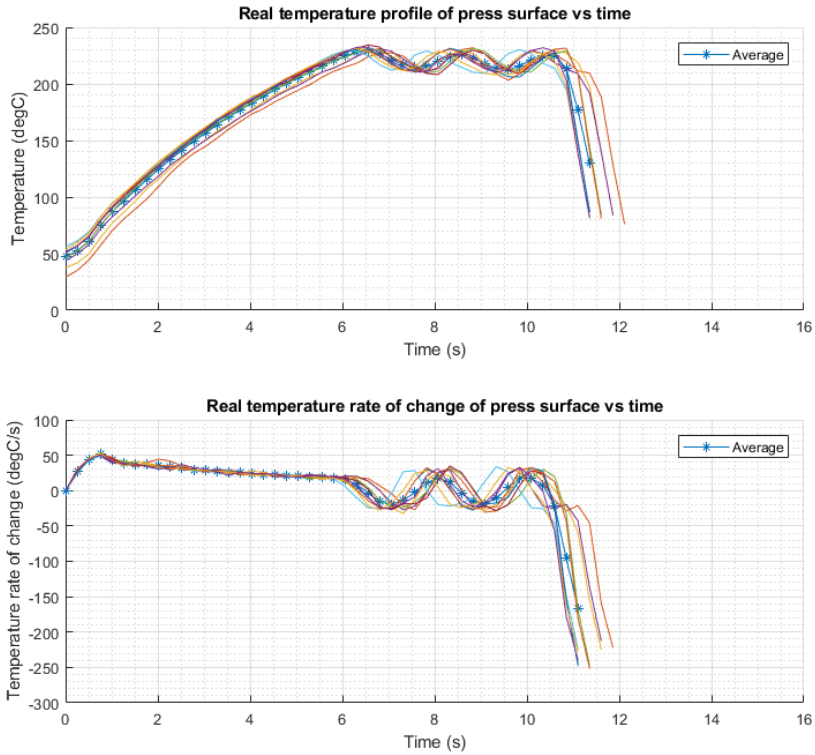

Figure 6.4: Estimated real temperature profile and temperature rate of change of second measurement considering the transient response of the thermocouple.

6.3. Comparison of experiments and simulations

To validate the measurements, they are compared to the model simulations discussed in chapter 4. The model parameters are adjusted to the realistic demonstrator properties, such as reflecting surface reflectance and heat loss through the adhesive layer.

6.3.1. Heating system

In the finite element model, a layer is inserted with epoxy adhesive in the corners and air in between. The air is relevant because the gap is so small that the layer of air also contributes to the thermal conduction. The emissivity of the reflective wall is 0.20. The simulation results correspond well to the real temperature estimation, as can be seen in figure 6.5. In the temperature rate of change graph in figure 6.5, a higher peak can be seen in the real temperature estimation, that is not present in the thermocouple measurement and simulation result. This is thought to be a result of electric start up inertia, caused by the thermocouple amplifier among others, that is not considered in the calculation of the real temperature. By better understanding of the electric circuit and more suitable components for quick rise time, the start up inertia can be reduced for a better measurement.

6.3.2. Cooling system

Due to the way of measuring the cooling system performance, the results are not well suited for validation of the finite element model. The measured velocity on the outlet has an uncertainty of ±30% and the cooling channel leaks in several places, so the mass flow changes over distance. Even though the measured cooling rate is better than the requirement, it cannot be said with certainty whether this is because of the heat exchanger or because of external flows around the heating element.

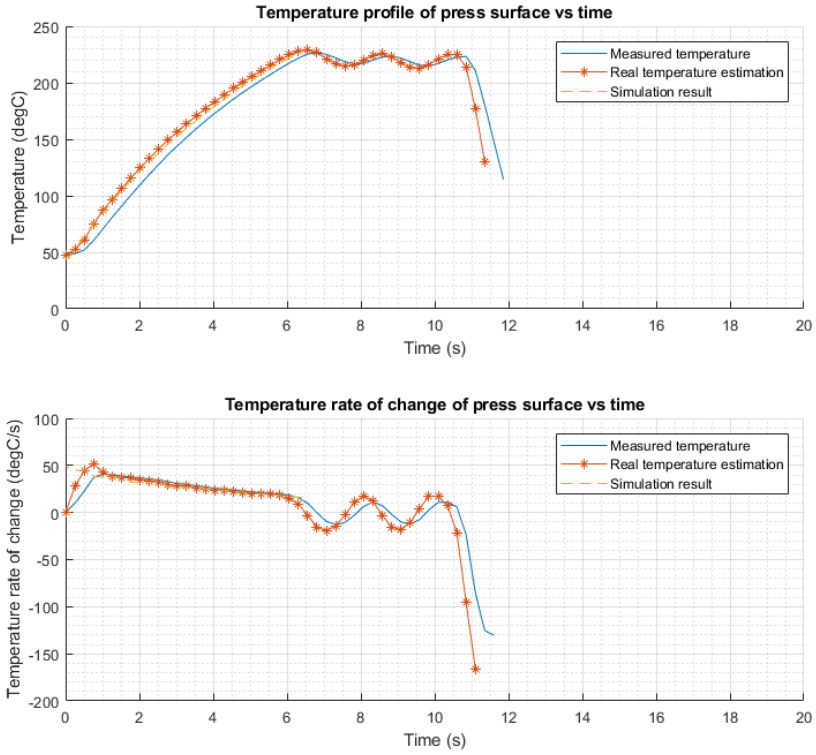

Figure 6.5: Comparison between the average measured and estimated real temperature profile and temperature rate of change of second measurement and heating model simulation.

7

Conclusions and recommendations

7.1. Conclusions

The goal of this thesis was to reduce the cycle time of flex-on-substrate assembly by designing a thermocompression bonding module with rapid heating and cooling capabilities and subsequently building and testing a proof-of-principle demonstrator thereof.

The heating concept is focused on low cost and better energy efficiency while still achieving high performance. The off-the-shelf light bulb is expected to last more than 50,000 cycles, making the cost per assembly negligible. The bulb can be easily replaced, minimizing the downtime when the bulb fails. The choice for a thin heating element reduces the energy lost as a result of the element's heat capacity by more than 90%. The heating system is designed to reach a heating rate of $300\,°C/s$, but a maximum rate of $41 \pm 9.9°C/s$ on average is measured. When taking the imperfect thermocouple contact into account, it is estimated to be $51 \pm 9.9°C/s$. It is found that the descripancy is caused by a heat bridge between the heating element and the main body, through the epoxy, and a lower reflecting surface reflectance. When these issues are addressed, the proposed concept has potential to improve the current technology in terms of cost, energy efficiency and performance.

The advanced cooling system design is a novel addition to a thermocompression bonding machine. The choice for staggered tubes makes it more complex than a flat plate heat exchanger, but this choice is justified by the large potential performance gain compared to the flat cooling surface, which creates no turbulence and has a smaller effective cooling surface area. The required maximum cooling rate is $150\,°C/s$ and the maximum measured rate is $1.7 \cdot 10^2 \pm 8.8°C/s$ on average. When taking the thermocouple contact into account, it is estimated at $2.3 \cdot 10^2 \pm 8.8°C/s$. As much as this shows the performance potential of the proposed cooling system, the flow velocity measurements were insufficiently accurate to draw conclusions on the relation between flow velocity and cooling power. Moreover, it is observed that the cooling channels leak air due to insufficient manufacturing tolerances, which makes it difficult to validate the developed simulation model.

The requirements set for heating and cooling rate have shown to be ambitious, casting a shadow over the success of this research: both the heating and cooling concepts have indeed shown their potential for decreasing the cycle time of FOS thermocompression bonding, while also keeping cost and power consumption down. While the heating system still needs some redesigning in order to reach the set requirement of $300\,°C/s$, the cooling system reaches a higher cooling rate than the current state-of-the-art machines, making it a valuable addition to the current technology.

7.2. Recommendations

Based on the observations and insights taken from this thesis, there are two categories of recommendations: design improvements and further research.

While the design proposed in this thesis shows potential for a commercially viable product, it can be improved on the following points.

1. In general, the design should be made more suitable for subtractive manufacturing. The current design can only be made with additive manufacturing or expensive subtractive methods. Higher tolerances can be achieved with subtractive manufacturing and it requires less post-processing steps. This specifically applies to the cooling channels and the staggered tube configuration.

2. The reflecting surface should be polished and coated with gold or silver, rather than aluminium foil. While aluminium foil has a reflectance of 80%, a properly fabricated gold or silver mirror can have a reflectance of up to 95% [47]. This would result in four times as much power being absorbed by the heating element.

3. A thermal barrier is needed between the heating element and the main body. In the demonstrator used in this thesis, the heat flowing through this contact and the heat from the light source are in equilibrium at low temperature, so the net heat flow is zero and the temperature cannot be further increased. A thermal barrier could be realized by either modifying the contributing contact surfaces or the main body material.

4. A solution should be found for airtight sealing of the cooling channel, including the glass plate interface. The heat exchanger is an unfavorable path to take for the airflow, since the turbulence is created by interrupting the air flow. The leaks cause air to exit the system before the heat exchanger.

To improve the understanding of thermocompression bonding and of this specific system, some experiments are recommended for further research.

1. Improve the thermal contact between the heating element and the thermocouple for more reliable measurement of the temperature and especially the temperature rate of change. This can be done by making a hole in the heating element, or by soldering or welding the thermocouple.

2. Validate the cooling system simulation model with an airtight cooling system demonstrator and a flow meter for reliable flow velocity measurement.

3. Validate the thermodynamic model of the FOS assembly and compare the temperature profile to the experiments that are presented in this thesis.

4. Bonding of FOS assemblies and testing the resulting joints on mechanical strength and electrical resistance. This allows the comparison between different heating and cooling rates and their effect on joint quality. Mechanical strength testing can be done according to IPC-TM-650 2.4.9, a so-called 90° peel test, and electrical resistance according to IPC-TM-650 2.6.24, known as four point probe measurement or Kelvin measurement [71, 72].

A

Flex-on-substrate assembly

Although solder joints and adhesive joints are quite different in nature, the assembly methods found in literature are quite similar because the important parameters are the same. This appendix gives an overview of those assembly methods and their application to both bond types.

A.1. Thermocompression bonding

Thermocompression bonding consists of a 'thermode', which is a heating element that is also stiff enough to exert a uniform pressure on the assembly. The execution of thermocompression bonding is different for solder and adhesive, so they are discussed separately.

For solder thermocompression bonding, the temperature is set slightly above the melting temperature of the solder, which accelerates the joint formation significantly [73]. The large volume fraction of Sn causes a higher melting point than the traditional Pb-rich alloys, of more than 200 °C, so the process temperature must be around 250-300 °C [13, 74]. For the common solder alloy SAC305 a successful bonding process has been designed with 1.5 MPa pressure and 240 °C for 5 seconds [75, 76]. The principle of operation can be seen in figure A.1 [77].

In ACA thermocompression bonding, there are three essential parameters: temperature, pressure and curing time. These parameters can be optimized using a Differential Scanning Calorimeter (DSC) and a 90° peel test [78, 79]. ACA thermocompression consists of one or two steps: pre-bonding is optional, where the adhesive is heated to just below the 'resin onset temperature', to slightly decrease the viscosity and let the particles flow towards the right location. Final bonding consists of much higher temperature and pressure, since the adhesive must cure as fast as possible and the particles must be kept in place while the adhesive viscosity changes [3].

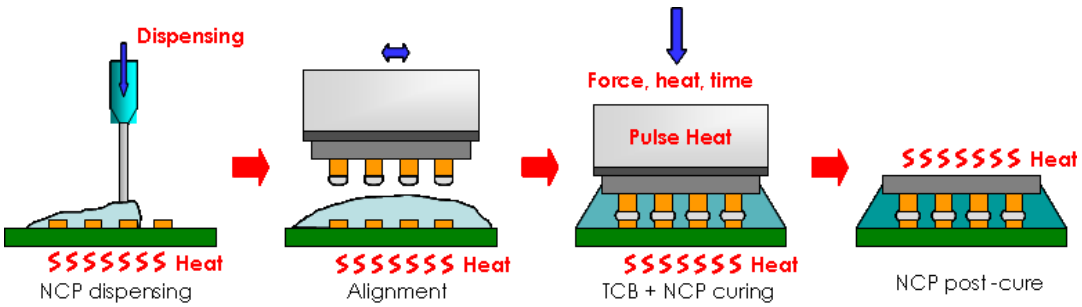

Figure A.1: Schematic explanation of thermo-compression soldering. Non-conductive underfill paste (NCP) is dispensed, the (prebumped) component is aligned, heat and pressure is applied and the NCP is post-cured [77]

For pre-bonding, the findings by Y. Lin, E. Abad and J. Lee have been compared [3, 78, 80, 81]. The applied pressure is generally around 1MPa, which is higher than for soldering, and is necessary just to keep the viscous adhesive in place, but low compared to the final bonding pressures. The pre-bonding temperature should be below the resin onset temperature to prevent pre-curing from happening and is therefore generally below 80 °C, but sometimes up to 90 °C, depending on the adhesive used [23, 81]. Lastly, the pre-bonding time varies quite a bit, which correlates with the curing strategy that is used, and thus with the final bonding parameters. Time periods between 1 and 10 seconds are used in the found literature.

The final bonding parameters found by the aforementioned researchers and many others are compared [23, 79, 82–84]. There are different noticeable trends in the parameters, dependent on the full curing process. When pre-bonding is included, the final bonding pressure is mostly between 2 and 5 MPa, except for Lin's research [78]. He used up to 80 MPa pressure, which might be because of the thicker two-layer ACF that is used, so the particles need to be pressed through a full epoxy layer before they form a contact with the other electrode. When pre-bonding is not used, the pressure is usually between 60 MPa and 100 MPa. The curing time is then around 10-15 seconds, which is faster then the two-step process.

It can be concluded that when the assembly can handle large mechanical stresses, single step curing is the quickest option, but for more delicate assemblies a pre-bonding step can significantly reduce the required pressure at the cost of extra processing time. Temperature of the final bonding step varies between the compared researches. Some use temperatures as low as 150 °C [10], others go as high as 255 °C. The curing rate increases when the temperature is increased, so less curing time is required at high temperature, but as for the high pressure, it puts the assembly in a harsh environment and not all assemblies will be able to withstand that. Lastly some researchers have attempted to speed up the process by preheating the assembly itself before applying the thermode [23, 79].

The adhesive joint quality depends on two parameters: electrical resistance and peel strength. Both parameters depend on the applied pressure and temperature of the bond process. Temperature affects electrical resistance because during pre-bonding the particles flow to the right place, and during final bonding the particles flow away from the desired location. It influences peel strength because it dictates the degree of cure, which in its turn is related to the adhesion strength. Pressure influences the resistance by pressing the conductive particles between the electrodes, increasing the contact area, which reduces the resistance. More pressure pushes out surface contamination and increases the bond strength. That being said, both parameters will always depend on the cleanliness and smoothness of the electrode pads [23, 79, 82–84].

A.2. Ultrasonic bonding

Ultrasonic bonding uses a 'sonotrode' vibrating at an ultrasonic frequency, transferring kinetic energy to the bonding material which is then dissipated into heat [85]. A big advantage of this is that heat is produced locally instead of the whole assembly being exposed to high temperatures. The process is very similar for solder and adhesive, but for solder this method also eliminates the need for flux, removing both the fluxing and flux cleaning process steps [86]. Ultrasonic vibrations can be longitudinal or lateral, i.e. orthogonal to the assembly or in-plane, respectively. Lateral vibrations induce alignment errors, longitudinal vibrations cause an effect called 'hammering' by hitting the assembly at ultrasound frequency [87]. An example of a longitudinal US bonding machine can be seen in figure A.2 [85].

When the bonding material is modeled as a viscoelastic material, the expression for volumetric heat production due to dissipation can be seen in equation A.1, where E'' is the loss modulus, ω is the excitation frequency, x is the vibration amplitude and t is the film thickness [88]. In this equation it is assumed that the bonding material is much softer than the flex and the substrate. Since this is not the case for solder, ultrasonic bonding is not

compatible with solder bonding.

$$Q_v''' = \frac{1}{2}E''V\varepsilon^2\frac{1}{V}\omega = \frac{1}{2}E''\left(\frac{x}{t}\right)^2\omega = \frac{1}{2}E''\frac{\omega x^2}{t^2} \tag{A.1}$$

From all variables in equation A.1, only the excitation frequency ω and the vibration amplitude x are process variables. They could be analytically determined by selecting a desired temperature for the bonding material and solving the heat equation [89]. The loss modulus is a complex material property, which is dependent on temperature and frequency, two important variables in this calculation. It can be seen that the heat dissipation is linearly proportional to the frequency, and proportional to the square of amplitude. Increasing the amplitude, however, has the downside of increasing the misalignment error of the interconnect. The frequency is therefore generally chosen very high, in the order of $20-40\,\text{kHz}$, so that the amplitude can be kept small (order of μm) [85, 90]. For ACAs, researchers suggest that there is an optimal ultrasonic power for every individual case, depending on all the materials used, that is the point where adding more power damages the assembly, and decreasing the power decreases the curing rate [90, 91]. For solder, ultrasonic bonding is mainly used to decrease the processing time and enhance the wetting [92]. It is therefore used in combination with temperature, in a process called thermosonic bonding.

A.3. Thermosonic bonding

Thermosonic bonding includes temperature, pressure and ultrasonic vibrations [93]. The part of the calculation in equation A.1 that changes is that the external temperature is much higher and thus the equilibrium bonding material temperature is also higher, since ΔT must be the same. This means that to achieve the same bonding material temperature, a much lower ultrasonic power can be applied, resulting in more alignment control. This is a trade-off between accuracy and speed; the ultrasonic part speeds up the process, the thermocompression part has better accuracy. The choice can be based on accuracy or speed requirements, but also on for instance the maximum pressure or temperature that the assembly can endure. It is also reported that thermosonic bonding results in higher reliability [93].

A.4. Laser bonding

Laser bonding exploits the high power density of a laser beam to heat up a specific desired location quickly [94]. Diode laser soldering applications have been demonstrated that require only 1 second of irradiation and show better joint quality than conventional reflow soldering [95–98]. The small irradiated (heated) area and high temperature gradient offer potential for fine-pitch applications. The small irradiated area also has a downside: the full bond area must be irradiated by a scanning process, which takes more time. It is therefore not possible

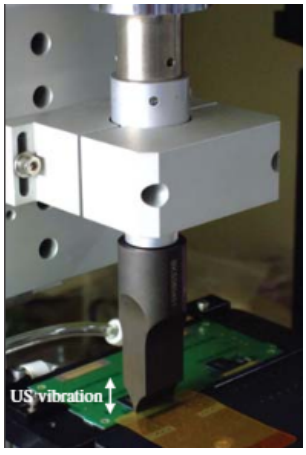

Figure A.2: Example of a longitudinal US bonding machine [85]

to assemble many ICs simultaneously [99]. Solder is only located between the electrodes, but ACA is spread across the full bond area, taking even more time to fully cure. Another issue might be obstruction of the laser beam by the bonded components that overshadow the bond areas. Lastly, safety is a more serious topic when lasers are introduced, making the process more constrained by rules and regulations.

A.5. Conclusions

An overview of the discussed assembly methods and their compatibility with solder bonding and ACA bonding is shown in table A.1. Thermocompression is the most versatile assembly method that works well for both bonding types. Thermosonic bonding is potentially faster than thermocompression bonding and requires lower temperature, but is less accurate due to the vibratory motion. Thermosonic bonding might face issues when using solder since it is much stiffer than the flex and substrate. Laser bonding is not very well documented, but shows potential for high speed reflow soldering. For ACA it will take longer because all of the adhesive film must be irradiated by the small laser spot, which is a much larger area than for soldering, which is only present between the electrodes.

Assembly Method	Solder	ACA
Thermocompression	+	++
Ultrasonic/Thermosonic	-	+
Laser bonding	++	-

Table A.1: Overview of assembly methods and their suitability to soldering and adhesive bonding

B

Concept architecture

Functional requirement	Strategy	Sub-strategy	Solution	Sub-solution	MoSCoW
Heat quickly	Energy conversion	Mechanical	Friction		Must have
			Elastic losses		
			Fluid compression		
		Electrical	Thermoelectric		
			Joule heating		
			Electrocaloric		
		Radiative	Incandescence	Exposed coil	
				Halogen lamp	
			Electroluminescence	Laser	
				LED	
		Magnetic	Thermomagnetic		
			Magnetocaloric		
			Induction heating		
		Chemical	Exothermic reaction		
			Release latent heat		
	Heat conduction	Solid	Heat source + high diffusivity		
			Righi-Leduc		
		Fluid	Heat exchanger		
			Release latent heat		
Cool quickly	Energy conversion	Mechanical	Fluid expansion		Should have
		Electrical	Thermoelectric effect		
			Pyroelectric effect		
		Radiative	Cool irradiated heat sink		
			High emissivity surface		
		Magnetic	Nernst		
			Righi-Leduc		
		Chemical	Endothermic		
			Charge latent heat		
	Heat conduction	Solid	Heat sink + high diffusivity		
			Cooling fins		
		Fluid	Heat exchanger		
			Charge latent heat		
	Convection	Increase convection surface	Detach thermode from assembly		
			Cooling fins		
		Increase heat transfer coefficient	Forced air flow		
			Fluid with high thermal inertia (k-rho-c)		

Figure B.1: (Sub-)strategies and (sub-)solutions found for the most important functional requirements: heating quickly and cooling quickly.

Functional requirement	Strategy	Sub-strategy	Solution	Sub-solution	MoSCoW
Distribute temperature evenly	Regulate evenly	Active	Independent local regulation		Should have
			Dependent local regulation	Series	
				Parallel	
		Passive	Uniform heat flux		
			Match heat flux with material thickness		
	Spread efficiently	Maximize diffusion speed	Maximize diffusivity		
			Minimize volume		
		Selective diffusion	Diffusion network/tree		
			Anisotropic conductivity		
Measure bottom temperature	Feedback	Mechanical	Bulb thermometer		Should have
		Electric	Thermocouple		
			Resistance Temperature Detector		
			Thermistor		
		Radiative	Pyrometer		
			Thermographic camera		
Distribute pressure evenly	Active	Align pressure tool	Rigid joint		Could have
			Compliant joint		
		Local strain variation	Smart materials		
			Distributed force actuation		
	Passive	Align pressure tool	Rigid joint		
			Compliant joint		
		Local strain variation	Elastic pressure surface		
			Force distribution mechanism		
Manage contamination	Disposable	Continuous	Interposer reel tape		Could have
			Absorb		
		Discrete	Interposing layer		
			No contamination layer		
	Non-disposable	Repel	Coating		
			Clean off		
		Convert	Chemical agent		
			Heating/cooling		
Measure vertical force	Feedback	Mechanical	Hydraulic		Could have
			Pneumatic		
		Electrical	Strain gauge		
			Piezo actuator		
			Capacitive		
Control collision impact	Attenuate	Full surface area	Compliant press surface		Could have
			Compliant press suspension		
		Probing	Deceleration trigger		
	Minimize		Low speed z-movement		
			Velocity profile with deceleration near impact		

Figure B.2: (Sub-)strategies and (sub-)solutions found for the additional functional requirements.

Weight	10	9	7	6	6	4	3	2	1		
Heating	P	I	Cx	C	Ct	E	D	F	N	Total	Weighted score
Joule	9	8	7	6	9	10	9	9	4	390	8,1
Laser	10	8	8	1	9	6	9	10	7	366	7,6
Halogen	9	9	9	10	10	8	7	10	8	435	9,1
Induction	9	2	8	8	8	9	9	6	7	342	7,1
Heat exchanger	7	8	7	7	10	7	9	8	10	374	7,8

Cooling	P	I	Cx	C	Ct	E	D	F	N	Total	Weighted score
Radiative cooling	7	9	8	10	3	4	10	10	10	361	7,5
Heat exchanger	10	8	7	7	10	8	9	8	8	406	8,5
Detach	6	5	7	7	1	5	9	10	10	279	5,8
Conductivity	5	8	10	10	3	3	10	9	3	333	6,9
Cooling fins	7	8	9	9	3	3	10	8	6	341	7,1

Figure B.3: Concept selection for the functions heating quickly and cooling quickly. The labels on the x-axis are respectively: (P)erformance, (I)ntegration, (C)omple(x)ity, (C)ost, (C)on(t)rollability, (E)nergy efficiency, (D)urability, (F)lexibility and (N)ovelty. The concepts are also The three best solutions for each function are selected for the concept generation phase. For heating, these are 'Joule heating', 'halogen' and 'heat exchanger'. For cooling, they are 'radiative cooling', 'heat exchanger' and 'cooling fins'.

C

Assembly process

A transient thermodynamic model of the assembly process is developed. The control volume encloses the electronic package, consisting of the flex circuit, ACA and substrate. From a thermodynamic point of view, the model is highly unsteady because of short heating and cooling times, not allowing materials to reach their steady state temperature.

$$\rho c \frac{\partial T}{\partial t} = \frac{\partial}{\partial x}\left(-k \frac{\partial T}{\partial x}\right) \tag{C.1}$$

$$\frac{\partial \theta}{\partial \tau} = Fo_i \frac{\partial^2 \theta}{\partial \xi_i^2} \tag{C.2}$$

The goal of analytically modelling the heat transfer problem is to estimate the course of temperature and use it to validate the finite element model in a later stage. Analytical derivations are bound to simplifications in order to be solvable. The model developed by Sun et al. is used [61], where the heat equation in equation C.1 is non-dimensionalized, as in equation C.2. The non-dimensional quantities are stated in equation C.3.

$$\xi_1 = \frac{x}{L_1}, \qquad \xi_2 = \frac{x - L_1}{L_2}, \qquad \xi_3 = \frac{x - (L_1 + L_2)}{L_3} \tag{C.3a}$$

$$\theta_i = \frac{T(\xi_i, t) - T_0}{T_s - T_0} \tag{C.3b}$$

$$\tau = \frac{t}{t_0}, \qquad Fo = \frac{\alpha_i t_0}{L_i^2}, \qquad \kappa_i = \frac{k_i}{L_i} \tag{C.3c}$$

$$i = 1, 2, 3 \tag{C.3d}$$

There are some assumptions that can be made to make the analytical model solvable, some of which are already applied in equations C.1 and C.2. They are listed below.

- There is no heat source or heat sink inside the control volume.
- The thermal conductivity and thermal diffusivity are time and temperature independent and uniform over each layer.
- There is perfect thermal contact between the layers, implying continuity in temperature and heat flux.
- The assembly's x and y dimensions are large compared to the layer thicknesses, therefore one-dimensional heat transfer in *z*-direction is assumed. This also implies there are no convective and radiative losses on the perimeter, which are reported to be negligible [63].

- The top surface has a temperature that is conform to the temperature of the bonding tool T_s, which is constant in time. This simulates the short time heating the ACA to 180 °C.
- The bottom surface is not affected by the top heating and stays at its initial temperature T_0.
- The ACA material properties are averaged between the conductive particles and the epoxy resin.
- There are no (well conducting) electrodes on both the flex circuit and the PCB substrate.

Now the boundary conditions, initial conditions and continuities can be specified, which are required to calculate the unknown variables. They can be seen in equation C.4.

$$\theta(\xi_1 = 0) = 1, \qquad \theta(\xi_3 = 1) = 0 \qquad \text{(Boundary conditions for top and bottom)} \quad \text{(C.4a)}$$

$$\theta(\xi_1 = 1) = \theta(\xi_2 = 0) \qquad \text{(Continuity in temperature)} \quad \text{(C.4b)}$$

$$\theta(\xi_2 = 1) = \theta(\xi_3 = 0) \qquad \text{(Continuity in temperature)} \quad \text{(C.4c)}$$

$$-\kappa_1 \frac{\partial\theta}{\partial\xi_1}(\xi_1 = 1) = -\kappa_2 \frac{\partial\theta}{\partial\xi_2}(\xi_2 = 0) \qquad \text{(Continuity in heat flux)} \quad \text{(C.4d)}$$

$$-\kappa_2 \frac{\partial\theta}{\partial\xi_2}(\xi_2 = 1) = -\kappa_3 \frac{\partial\theta}{\partial\xi_3}(\xi_3 = 0) \qquad \text{(Continuity in heat flux)} \quad \text{(C.4e)}$$

$$\theta(\tau = 0) = 0 \qquad \text{(Initial condition } T = T_0\text{)} \quad \text{(C.4f)}$$

With the constraints specified, the heat equation can be analyzed. First it is split into a steady-state term and a transient term, such that the transient term decays with time and at $t = \infty$ only the steady-state term remains. The steady-state term in a 1D heat transfer problem is simply a linear polynomial for each layer (equation C.5). From the initial condition in equation C.4f it also follows that $\phi(\xi_i, 0) = \psi(\xi_i)$. The transient term $\phi(\xi_i, \tau)$ will now be expanded.

$$\psi_1 = 1 - (\Delta\theta)_1 \xi_1 \quad \text{(C.5a)}$$

$$\psi_2 = 1 - (\Delta\theta)_1 - (\Delta\theta)_2 \xi_2 \quad \text{(C.5b)}$$

$$\psi_3 = 1 - (\Delta\theta)_1 - (\Delta\theta)_2 - (\Delta\theta)_3 \xi_3 \quad \text{(C.5c)}$$

$$(\Delta\theta)_i = \frac{1/\kappa_i}{1/\kappa_1 + 1/\kappa_2 + 1/\kappa_3} \quad \text{(C.5d)}$$

If the boundary conditions and the initial condition are filled in in the standard solution

$$\phi_i = \sum_{n=0}^{\infty} A_n e^{-\lambda_n^2 Fo_i \tau} (\alpha_n sin(\mu_{in}\xi_i) + \beta_n cos(\mu_{in}\xi_i))$$

Then the transient terms per layer are expressed in equation C.6, the parameters are defined in equation C.7

$$\phi_1 = \sum_{n=0}^{\infty} A_n e^{-\lambda_n^2 Fo_1 \tau} sin(\lambda_n \xi_1) \quad \text{(C.6a)}$$

$$\phi_2 = \Delta_1 \sum_{n=0}^{\infty} A_n e^{-\lambda_n^2 Fo_1 \tau} (\alpha_n sin(\mu_{1n}\xi_2) + \beta_n cos(\mu_{1n}\xi_2)) \quad \text{(C.6b)}$$

$$\phi_3 = \Delta_2 \sum_{n=0}^{\infty} A_n e^{-\lambda_n^2 Fo_1 \tau} (\bar{\alpha}_n sin(\mu_{2n}\xi_3) + \bar{\beta}_n cos(\mu_{2n}\xi_3)) \quad \text{(C.6c)}$$

$$\Delta_1 = \frac{\kappa_1}{\kappa_2}\sqrt{\frac{Fo_2}{Fo_1}}, \qquad \Delta_2 = \frac{\kappa_1}{\kappa_3}\sqrt{\frac{Fo_3}{Fo_1}} \tag{C.7a}$$

$$\mu_{1n} = \sqrt{\frac{Fo_1}{Fo_2}}\lambda_n, \qquad \mu_{2n} = \sqrt{\frac{Fo_1}{Fo_3}}\lambda_n \tag{C.7b}$$

$$\alpha_n = cos(\lambda_n), \qquad \beta_n = \frac{1}{\Delta_1}sin(\lambda_n) \tag{C.7c}$$

$$\bar{\alpha}_n = cos(\lambda_n)cos(\mu_{1n}) - \frac{1}{\Delta_1}sin(\lambda_n)sin(\mu_{1n}) \tag{C.7d}$$

$$\bar{\beta}_n = \frac{\Delta_1}{\Delta_2}cos(\lambda_n)sin(\mu_{1n}) + \frac{1}{\Delta_2}sin(\lambda_n)cos(\mu_{1n}) \tag{C.7e}$$

The parameters α_n, β_n, $\bar{\alpha}_n$ and $\bar{\beta}_n$ can be found by filling in the continuity equations and A_n can be found through equation C.8

$$M_n = \frac{\kappa_2\kappa_3}{2} + \frac{\kappa_1\kappa_3}{2}\left(cos^2(\lambda_n) + \frac{1}{\Delta_1^2}sin^2(\lambda_n)\right) + \frac{\kappa_1\kappa_2}{2}(\bar{\alpha}_n^2 + \bar{\beta}_n^2) \tag{C.8a}$$

$$A_n = \frac{\kappa_2\kappa_3}{\lambda_n M_n} \tag{C.8b}$$

The last unknown variables are the eigenvalues λ_n. They can be found by solving the following equation using Rolle's theorem to find all zeros, which states that when two function values have opposite signs, there must be a zero in between (equation C.9) [100]. Finally, the resulting expression for the temperature distribution per layer can be seen in equation C.10.

$$F(\lambda_n) = tan(\lambda_n) + \frac{\Delta_1 tan(\mu_{1n}) + \Delta_2 tan(\mu_{2n})}{1 - \frac{\Delta_2}{\Delta_1}tan(\mu_{1n})tan(\mu_{2n}} = 0 \tag{C.9}$$

$$\theta(\xi_1,\tau) = 1 - (\Delta\theta)_1\xi_1 - \sum_{n=0}^{\infty} A_n e^{-\lambda_n^2 Fo_1\tau} sin(\lambda_n\xi_1) \tag{C.10a}$$

$$\theta(\xi_2,\tau) = 1 - (\Delta\theta)_1 - (\Delta\theta)_2\xi_2 - \Delta_1\sum_{n=0}^{\infty} A_n e^{-\lambda_n^2 Fo_1\tau}\left(\alpha_n sin(\mu_{1n}\xi_2) + \beta_n cos(\mu_{1n}\xi_2)\right) \tag{C.10b}$$

$$\theta(\xi_3,\tau) = 1 - (\Delta\theta)_1 - (\Delta\theta)_2 - (\Delta\theta)_3\xi_3 - \Delta_2\sum_{n=0}^{\infty} A_n e^{-\lambda_n^2 Fo_1\tau}\left(\bar{\alpha}_n sin(\mu_{2n}\xi_3) + \bar{\beta}_n cos(\mu_{2n}\xi_3)\right) \tag{C.10c}$$

D

Circuit diagram

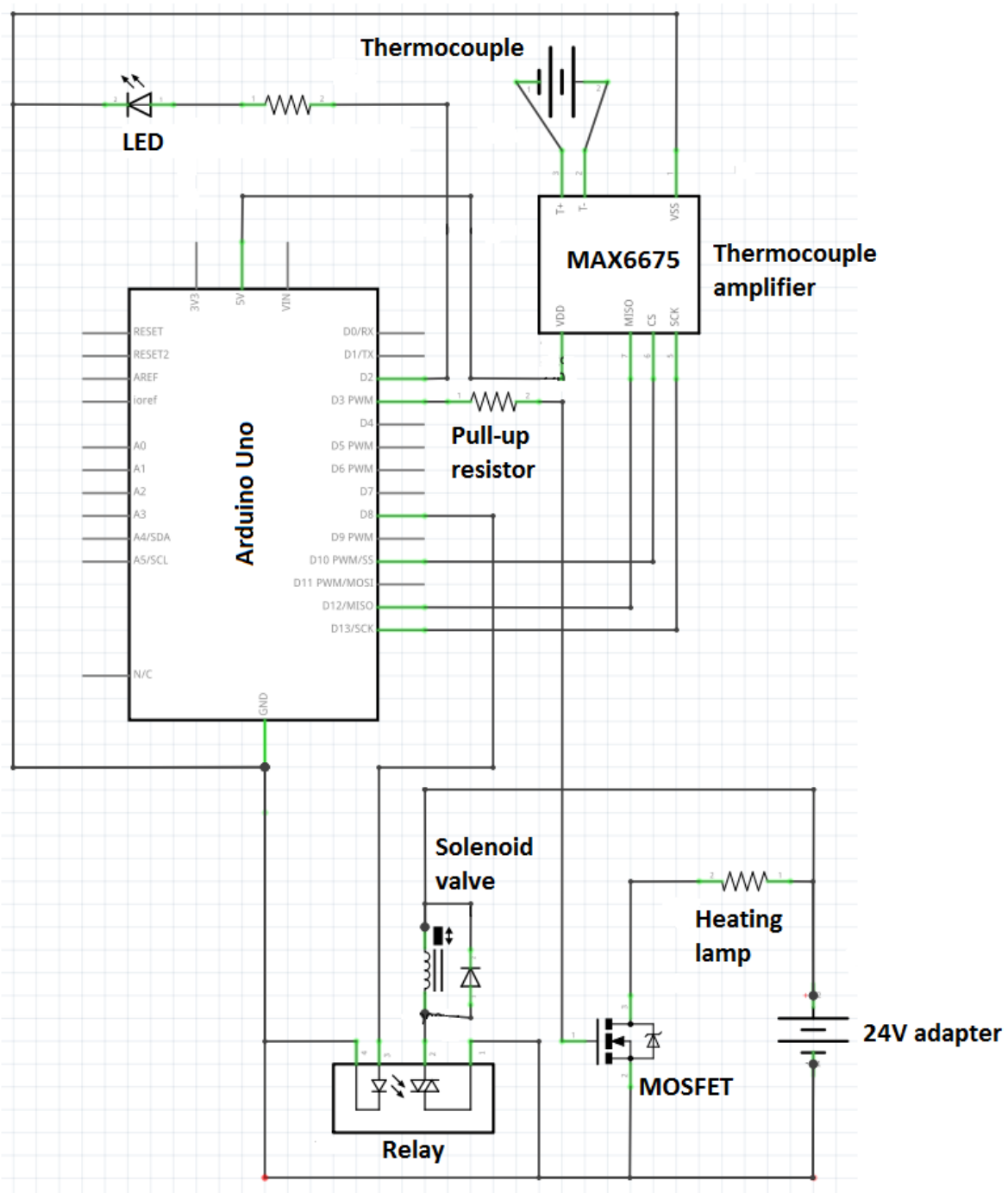

Figure D.1: Circuit diagram of the electronic circuit for Arduino control of the demonstrator. It contains a subsystem for the lamp, which also includes a 24V adapter, MOSFET and pull-up resistor, a subsystem for the solenoid valve, which also includes a relay, diode, LED and the same 24V adapter, and a subsystem for the thermocouple, which also includes a thermocouple amplifier.

Bibliography

[1] Peter Macleod et al. *A review of flexible circuit technology and its applications*. PRIME Faraday Partnership, 2002.

[2] J. Liu. Aca bonding technology for low cost electronics packaging applications-current status and remaining challenges. *4th International Conference on Adhesive Joining and Coating Technology in Electronics Manufacturing. Proceedings. Presented at Adhesives in Electronics 2001 (Cat. No.00EX431)*, Mar 2001. doi: 10.1109/adhes.2000.860564.

[3] J. Lee, D. Geiger, and D. Shangguan. Process development and reliability study with anisotropic conductive film bonding on multiple types of pcb surface finishes. pages 1758–1763, 2011. doi: 10.1109/ECTC.2011.5898750.

[4] J. Kiilunen, L. Frisk, and M. Hoikkanen. The effect of bonding temperature and curing time on peel strength of anisotropically conductive film flex-on-board samples. *IEEE Transactions on Device and Materials Reliability*, 12(2):455–461, June 2012. ISSN 1530-4388. doi: 10.1109/TDMR.2012.2190413.

[5] A. Eitan and K. Hung. Thermo-compression bonding for fine-pitch copper-pillar flip-chip interconnect - tool features as enablers of unique technology. In *2015 IEEE 65th Electronic Components and Technology Conference (ECTC)*, pages 460–464, May 2015. doi: 10.1109/ECTC.2015.7159631.

[6] H. Clauberg, A. Rezvani, D. Buergi, T. Colosimo, G. Frick, O. Yauw, T. Strothmann, and B. Chylak. Thermocompression flip chip bonding optimization for pre-applied underfill. In *2015 IEEE 17th Electronics Packaging and Technology Conference (EPTC)*, pages 1–4, Dec 2015. doi: 10.1109/EPTC.2015.7412343.

[7] K. Jang and K. Paik. Effects of heating rate on material properties of anisotropic conductive film (acf) and thermal cycling reliability of acf flip chip assembly. *IEEE Transactions on Components and Packaging Technologies*, 32(2):339–346, June 2009. ISSN 1557-9972. doi: 10.1109/TCAPT.2008.2001701.

[8] Trendforce. Global smartphone production volume, Nov 2019. URL `https://press.trendforce.com/node/view/3313.html`.

[9] Jin Zhang, Qipeng Guo, and Bronwyn L. Fox. Study on thermoplastic-modified multifunctional epoxies: Influence of heating rate on cure behaviour and phase separation. *Composites Science and Technology*, 69(7):1172 – 1179, 2009. ISSN 0266-3538. doi: https://doi.org/10.1016/j.compscitech.2009.02.016. URL `http://www.sciencedirect.com/science/article/pii/S0266353809000761`.

[10] Tae-Kyu Lee, Thomas R. Bieler, Choong-Un Kim, and Hongtao Ma. *Fundamentals of lead-free solder interconnect technology: from microstructures to reliability*. Springer, 2015.

[11] Amada Miyachi. Hot bar reflow soldering fundamentals, Mar 2016. URL `https://www.amadamiyachi.eu/sites/default/files/documents/whitepapers/AMYEHotBarReflowSolderingTechnology03-2016.pdf`.

[12] Ning-Cheng Lee. *Reflow soldering processes and troubleshooting: SMT, BGA, CSP, and flip chip technologies*. Butterworth-Heinemann Newnes, 2002.

[13] Shunfeng Cheng, Chien-Ming Huang, and Michael Pecht. A review of lead-free solders for electronics applications. *Microelectronics Reliability*, 75:77 – 95, 2017. ISSN 0026-2714. doi: https://doi.org/10.1016/j.microrel.2017.06.016. URL http://www.sciencedirect.com/science/article/pii/S0026271417302044.

[14] Rainer Dohle, Florian Schussler, Thomas Friedrich, Jorg Gossler, Thomas Oppert, and Jorg Franke. Adapted assembly processes for flip-chip technology with solder bumps of 50 µm or 40 µm diameter. *3rd Electronics System Integration Technology Conference ESTC*, 2010. doi: 10.1109/estc.2010.5643014.

[15] A. Lofti and Martin Howarth. Industrial application of fuzzy systems: Adaptive fuzzy control of solder paste stencil printing. *Information Sciences*, 107:273–285, 06 1998. doi: 10.1016/S0020-0255(97)10053-6.

[16] J. Keck and N. Lee. Assessment of solder paste technology limitation at miniaturization for sip and smt application. In *2017 12th International Microsystems, Packaging, Assembly and Circuits Technology Conference (IMPACT)*, pages 89–96, Oct 2017. doi: 10.1109/IMPACT.2017.8255961.

[17] Myung Jin Yim and Kyung-Wook Paik. Review of electrically conductive adhesive technologies for electronic packaging. *Electron Mater Lett*, 2, 01 2006.

[18] Afsar Uddin, M Ali, and Hau Ping Chan. Achieving optimum adhesion of conductive adhesive bonded flip-chip on flex packages. *Rev.Adv.Mater.Sci*, 21:165–172, 11 2009.

[19] A. Franck. Thermosets and structural adhesives. URL http://www.tainstruments.com/pdf/literature/RH007.pdf.

[20] Bo Tao, Zhouping Yin, and Youlun Xiong. Acf curing process optimization based on degree of cure considering contact resistance degradation of joints. *Soldering & Surface Mount Technology*, 22(4):4–12, 2010. doi: 10.1108/09540911011076835.

[21] Sun-Chul Kim and Young-Ho Kim. Review paper: Flip chip bonding with anisotropic conductive film (acf) and nonconductive adhesive (nca). *Current Applied Physics*, 13:S14 – S25, 2013. ISSN 1567-1739. doi: https://doi.org/10.1016/j.cap.2013.05.009. URL http://www.sciencedirect.com/science/article/pii/S1567173913002010. Special Issue: ENGE 2012.

[22] M.J. Rizvi, Y.C. Chan, Chris Bailey, Hua Lu, and Ahmed Sharif. The effect of curing on the performance of acf bonded chip-on-flex assemblies after thermal ageing. *Soldering & Surface Mount Technology*, 17, 06 2005. doi: 10.1108/09540910510597492.

[23] Kyoung-Lim Suk, Kyosung Choo, Sung Jin Kim, Jong-Soo Kim, and Kyung-Wook Paik. Studies on various chip-on-film (cof) packages using ultra fine pitch two-metal layer flexible printed circuits (two-metal layer fpcs). *Microelectronics Reliability*, 52(6):1182 – 1188, 2012. ISSN 0026-2714. doi: https://doi.org/10.1016/j.microrel.2011.12.020. URL http://www.sciencedirect.com/science/article/pii/S0026271411005531.

[24] S. M. Ramkumar, H. Venugopalan, and K. Khanna. Novel anisotropic conductive adhesive for 3d stacking and lead-free pcb packaging — a review. In *2011 IEEE 61st Electronic Components and Technology Conference (ECTC)*, pages 246–254, May 2011. doi: 10.1109/ECTC.2011.5898521.

[25] C.-W. Ha, K.-R. Kim, K.-S. Kim, and S. Kim. Sliding mechanism of lateral thermosonic process with anisotropic conductive film for high productivity and high reliability. *IEEE Transactions on Components, Packaging and Manufacturing Technology*, 3(2):205–212, 2013. doi: 10.1109/TCPMT.2012.2234829. URL https://www.scopus.com/inward/record.uri?eid=2-s2.0-84873473606&doi=10.1109%2fTCPMT.2012.2234829&partnerID=40&md5=74f98b27cf655a638c77973074a5d30d.

[26] 3m™ anisotropic conductive film 5363, Nov 2013. URL http://multimedia.3m.com/mws/media/4075900/3mtm-anisotropic-conductive-film-5363.pdf.

[27] Ed Briggs, Indium Corporation Lasky, Ron, and Dartmouth College. Best practices reflow profiling for lead-free smt assembly. *SMTA International*, Oct 2009.

[28] Xin Wu and Hongqi Hao. The effect of adhesive curing condition on bonding strength in auto body assembly. *Journal of Manufacturing Science and Engineering*, 127(2):411–419, 04 2005. ISSN 1087-1357. doi: 10.1115/1.1870014.

[29] R.A. Islam, B.Y. Wu, M.O. Alam, Y.C. Chan, and W. Jillek. Investigations on microhardness of sn–zn based lead-free solder alloys as replacement of sn–pb solder. *Journal of Alloys and Compounds*, 392(1):149 – 158, 2005. ISSN 0925-8388. doi: https://doi.org/10.1016/j.jallcom.2004.08.079. URL http://www.sciencedirect.com/science/article/pii/S0925838804012022.

[30] Jun SHEN, Yong chang LIU, Ya jing HAN, Hou xiu GAO, Chen WEI, and Yu qin YANG. Effects of cooling rates on microstructure and microhardness of lead-free sn-3.5 *Transactions of Nonferrous Metals Society of China*, 16(1):59 – 64, 2006. ISSN 1003-6326. doi: https://doi.org/10.1016/S1003-6326(06)60011-3. URL http://www.sciencedirect.com/science/article/pii/S1003632606600113.

[31] Hwa-Teng Lee and Kuo-Chen Huang. Effects of cooling rate on the microstructure and morphology of sn-3.0ag-0.5cu solder. *Journal of Electronic Materials*, 45(1):182–190, 2015. doi: 10.1007/s11664-015-4189-3.

[32] G.C. Stevens and M.J. Richardson. Factors influencing the glass transition of dgeba-anhydride epoxy resins. *Polymer*, 24(7):851 – 858, 1983. ISSN 0032-3861. doi: https://doi.org/10.1016/0032-3861(83)90203-3. URL http://www.sciencedirect.com/science/article/pii/0032386183902033.

[33] H. Clauberg, A. Rezvani, E. Galipeau, M. Wasserman, T. Colosimo, G. Frick, D. Buergi, and B. Chylak. Advanced thermocompression flip chip bonding. In *2014 IEEE 16th Electronics Packaging Technology Conference (EPTC)*, pages 492–495, Dec 2014. doi: 10.1109/EPTC.2014.7028380.

[34] H. Clauberg, A. Rezvani, V. Venkatesan, G. Frick, B. Chylak, and T. Strothmann. Chip-to-chip and chip-to-wafer thermocompression flip chip bonding. In *2016 IEEE 66th Electronic Components and Technology Conference (ECTC)*, pages 600–605, May 2016. doi: 10.1109/ECTC.2016.329.

[35] Hot bar bonding. https://www.amadamiyachi.eu/nl/kennisbank/hot-bar-bonding. Accessed: 29-03-2019.

[36] Nova plus - die bonder and flip chip bonder. http://amicra.com/products/die-flip-chip-bonder/nova-plus-die-bonder-and-flip-chip-bonder. Accessed: 29-03-2019.

[37] Datacon 8800 tc. https://www.besi.com/products-technology/product-details/product/datacon-8800-tcnbspadvanced/. Accessed: 29-03-2019.

[38] Kulicke & soffa apama c2s. https://www.kns.com/Products/Equipment/Advanced-Packaging-(TCB)/APAMA-C2S. Accessed: 29-03-2019.

[39] Hot bar reflow soldering systems. https://www.nordson.com/en/divisions/dima/processes/hot-bar-reflow-soldering-systems. Accessed: 29-03-2019.

[40] Hotbar automation equipment made in the usa. https://toddco.com/. Accessed: 29-03-2019.

[41] Jennifer Stapelton. *DSDM, business focused development*. Pearson Education, 2003.

[42] D. Copeland. Optimization of parallel plate heatsinks for forced convection. In *Sixteenth Annual IEEE Semiconductor Thermal Measurement and Management Symposium (Cat. No.00CH37068)*, pages 266–272, March 2000. doi: 10.1109/STHERM.2000.837093.

[43] Dry air properties. URL https://www.engineeringtoolbox.com/dry-air-properties-d_973.html.

[44] Theodore L. Bergman and Adrienne S. Lavine. *Fundamentals of Heat and Mass Transfer*. John Wiley & Sons, 2017.

[45] *150W G6.35 24V Quartz-Halogen Lamp*. Philips Lighting, 2019. URL https://www.assets.signify.com/is/content/PhilipsLighting/fp924031720503-pss-nl_nl.

[46] Zeiss Davidson, Michael W. Tungsten-halogen incandescent lamps. URL zeiss-campus.magnet.fsu.edu/articles/lightsources/tungstenhalogen.html.

[47] Edmund Optics Worldwide. Metallic mirror coatings: Edmund optics. URL https://www.edmundoptics.com/knowledge-center/application-notes/optics/metallic-mirror-coatings/.

[48] John H Henninger. Solar absorptance and thermal emittance of some common spacecraft thermal-control coatings. Technical report, NATIONAL AERONAUTICS AND SPACE ADMINISTRATION WASHINGTON DC, 1984.

[49] Thermtest Inc. Materials database - thermal properties. URL https://thermtest.com/materials-database#.

[50] Ushio Lighting. Halogen lamps technical specifications. URL https://www.ushio.com/files/manual/halogentechnicalspecs.pdf.

[51] Frank M. White. *Fluid mechanics*. McGraw-Hill, 2016.

[52] A. Žukauskas. Heat transfer from tubes in crossflow. volume 8 of *Advances in Heat Transfer*, pages 93 – 160. Elsevier, 1972. doi: https://doi.org/10.1016/S0065-2717(08)70038-8. URL http://www.sciencedirect.com/science/article/pii/S0065271708700388.

[53] Edmund Optics Worldwide. The correct material for infrared (ir) applications. URL https://www.edmundoptics.com/knowledge-center/application-notes/optics/the-correct-material-for-infrared-applications/.

[54] Schott Advanced Optics. D 263 t eco-friendly thin glass. URL https://www.schott.com/advanced_optics/english/products/optical-materials/thin-glass/thin-glass-d-263-t-eco/index.html.

[55] Max Born and Emil Wolf. *Principles of optics: electromagnetic theory of propagation, interference and diffraction of light*. Elsevier, 1974.

[56] Michael Ashby. *CES Edupack*.

[57] Richard Jenkins, Barry Aldwell, Shuo Yin, Morten Meyer, A.J. Robinson, and Rocco Lupoi. Energy efficiency of a quartz tungsten halogen lamp: Experimental and numerical approach. *Thermal Science and Engineering Progress*, 13:100385, 2019. ISSN 2451-9049. doi: https://doi.org/10.1016/j.tsep.2019.100385. URL http://www.sciencedirect.com/science/article/pii/S2451904919302057.

[58] J. R. Ehlert and T. F. Smith. View factors for perpendicular and parallel rectangular plates. *Journal of Thermophysics and Heat Transfer*, 7(1):173–175, 1993. doi: 10.2514/3.11587. URL https://doi.org/10.2514/3.11587.

[59] T.w. Tong, D.l. Mcelroy, and D.w. Yarbrough. Transient conduction and radiation heat transfer in porous thermal insulations. *Journal of Thermal Insulation*, 9(1):13–29, Jul 1985. doi: 10.1177/109719638500900103.

[60] GPI Prototype. Eos aluminium alsi10mg material data sheet, 2014. URL https://gpiprototype.com/pdf/EOS_Aluminium_AlSi10Mg_en.pdf.

[61] Yuzhi Sun and Indrek S. Wichman. On transient heat conduction in a one-dimensional composite slab. *International Journal of Heat and Mass Transfer*, 47(6):1555 – 1559, 2004. ISSN 0017-9310. doi: https://doi.org/10.1016/j.ijheatmasstransfer.2003.09.011. URL http://www.sciencedirect.com/science/article/pii/S0017931003005337.

[62] Dupont. Dupont kapton material properties. URL https://www.dupont.com/content/dam/dupont/products-and-services/membranes-and-films/polyimde-films/documents/DEC-Kapton-summary-of-properties.pdf.

[63] V. A. Chiriac and T. Y. T. Lee. Transient thermal analysis of an acf package assembly process. *IEEE Transactions on Components and Packaging Technologies*, 24(4):673–681, Dec 2001. ISSN 1521-3331. doi: 10.1109/6144.974960.

[64] LLC. Engineers Edge. Thermal properties of non-metals, Mar 2017. URL https://www.engineersedge.com/heat_transfer/thermal_properties_of_nonmetals_13967.htm.

[65] COMSOL. The heat transfer module user's guide, 2018. URL https://doc.comsol.com/5.4/doc/com.comsol.help.heat/HeatTransferModuleUsersGuide.pdf.

[66] COMSOL. Which turbulence model should i choose for my cfd application? URL https://www.comsol.com/blogs/which-turbulence-model-should-choose-cfd-application/.

[67] COMSOL. The cfd module user's guide, 2018. URL https://doc.comsol.com/5.4/doc/com.comsol.help.cfd/CFDModuleUsersGuide.pdf.

[68] Ltd Hitachi Chemical Co. Development of new anisotropic conductive films enabling reduction in thickness and achieving finer pitch in displays, Dec 2014. URL http://www.hitachi-chem.co.jp/english/information/2014/n_141216.html.

[69] tesa. tesa® 60670. URL https://www.tesa.com/en/industry/tesa-60670.html.

[70] David R. Lide. *CRC handbook of chemistry and physics: a ready-reference book of chemical and phyical data*. CRC Press, 1992.

[71] IPC. Ipc-tm-650 test methods manual, Apr 2014. URL https://www.ipc.org/TM/2.4.9e.pdf.

[72] IPC. Ipc-tm-650 test methods manual, Nov 1998. URL https://www.ipc.org/TM/2-6-24.pdf.

[73] Ji Fan and Chuan Seng. Low temperature wafer-level metal thermo-compression bonding technology for 3d integration. *Metallurgy - Advances in Materials and Processes*, 2012. doi: 10.5772/48216.

[74] Ho-Ming Tong. *Advanced flip chip packaging*. Springer, 2013.

[75] Jeong-Won Yoon, Jong-Gun Lee, Jong-Bum Lee, Bo-In Noh, and Seung-Boo Jung. Thermo-compression bonding of electrodes between fpcb and rpcb by using pb-free solders. *Journal of Materials Science: Materials in Electronics*, 23(1):41–47, Jan 2012. ISSN 1573-482X. doi: 10.1007/s10854-011-0402-1. URL https://doi.org/10.1007/s10854-011-0402-1.

[76] Haksun Lee, Kwang-Seong Choi, Yong-Sung Eom, Hyun-Cheol Bae, and Jin Ho Lee. Sn58bi solder interconnection for low-temperature flex-on-flex bonding. *ETRI Journal*, 38(6):1163–1171, 2016. doi: 10.4218/etrij.16.0115.0945. URL https://onlinelibrary.wiley.com/doi/abs/10.4218/etrij.16.0115.0945.

[77] Yiu Ming Cheung, Dewen Tian, Giuseppe Mak, and Ming Li. Solder joint integrity of tc-ncp thermo-compression bonding process. 10 2013.

[78] Yao-Sheng Lin, Tsung-Fu Yang, Wen-Chi Chen, Tai-Hung Chen, Chun-Cheng Cheng, and Yung-Hui Yeh. Fine pitch compliant bump interconnection for flip chip on flexible display packaging by anisotropic conductive film. pages 501 – 506, 01 2007. ISBN 1-4244-0985-3. doi: 10.1109/ECTC.2007.373844.

[79] Su-Tsai Lu, Yu-Min Lin, Chun-Chih Chuang, Tai-Hong Chen, and Wen-Hwa Chen. Development of a novel compliant-bump structure for aca-bonded chip-on-flex (cof) interconnects with ultra-fine pitch. *IEEE Transactions on Components, Packaging and Manufacturing Technology*, 1(1):33–42, 2011. doi: 10.1109/tcpmt.2010.2101431.

[80] Estefania Abad, Barbara Mazzolai, Aritz Juarros, Alessio Mondini, Angelika Krenkow, and Thomas Becker. Fabrication and encapsulation processes for flexible smart rfid tags. In Cristina Turcu, editor, *Radio Frequency Identification Fundamentals and Applications*, chapter 14. IntechOpen, Rijeka, 2010. doi: 10.5772/7981. URL https://doi.org/10.5772/7981.

[81] J.-S. Lee, J.-H. Kim, and K.-W. Paik. Effects of flux activator addition in nanofiber/solder anisotropic conductive films (acfs) on the solder wettability of flex-on-flex (fof) assembly. *IEEE Transactions on Components, Packaging and Manufacturing Technology*, 8(7):1316–1322, 2018. doi: 10.1109/TCPMT.2018.2836982.

[82] K.W. Paik. Recent progress in anisotropic conductive adhesives (acas) technology: Materials and processing. pages 20–22, 2012. URL https://www.scopus.com/inward/record.uri?eid=2-s2.0-84871733485&partnerID=40&md5=9c33dab0dff02dc69a84617850ae6011.

[83] H. G. Lee, J. Shin, Y. Choi, and K. Paik. Effects of thermocompression bonding parameters on cu pillar/sn-ag microbump solder joint morphology using nonconductive films. *IEEE Transactions on Components, Packaging and Manufacturing Technology*, 7 (3):450–455, March 2017. ISSN 2156-3985. doi: 10.1109/TCPMT.2016.2641040.

[84] Kyung-Wook Paik and Dal-Jin Yoon. A study on the novel anchoring polymer layer(apl) anisotropic conductive films(acfs) for ultra fine pitch assembly applications. *2018 Pan Pacific Microelectronics Symposium (Pan Pacific)*, 2018. doi: 10.23919/panpacific.2018.8318988.

[85] Kiwon Lee, Ilkka J. Saarinen, Lasse Pykari, and Kyung Wook Paik. High power and high reliability flex-on-board assembly using solder anisotropic conductive films combined with ultrasonic bonding technique. *IEEE Transactions on Components, Packaging and Manufacturing Technology*, 1(12):1901–1907, 2011. doi: 10.1109/tcpmt.2011.2169965.

[86] V.L. Lanin. Ultrasonic soldering in electronics. *Ultrasonics Sonochemistry*, 8(4):379 – 385, 2001. ISSN 1350-4177. doi: https://doi.org/10.1016/S1350-4177(01)00065-7. URL http://www.sciencedirect.com/science/article/pii/S1350417701000657.

[87] Q. Tan, W. Zhang, B. Schaible, L. J. Bond, T.H. Ju, and Y.C. Lee. Thermosonic flip-chip bonding using longitudinal ultrasonic vibration. *IEEE Transactions on Components, Packaging, and Manufacturing Technology: Part B*, 21(1):53–58, Feb 1998. ISSN 1070-9894. doi: 10.1109/96.659506.

[88] M. N. Tolunay, P. R. Dawson, and K. K. Wang. Heating and bonding mechanisms in ultrasonic welding of thermoplastics. *Polymer Engineering & Science*, 23(13):726–733, 9 1983. ISSN 1548-2634. doi: 10.1002/pen.760231307. URL https://doi.org/10.1002/pen.760231307.

[89] Anthony F. Mills. *Basic heat and mass transfer*. Prentice Hall, 1999.

[90] Y.C. Lin, Hao Jin, and Xiao-Nan Fang. Effects of ultrasonic bonding process on polymer-based anisotropic conductive film joints in chip-on-glass assemblies. *Polymer Testing*, 30(3):318 – 323, 2011. ISSN 0142-9418. doi: https://doi.org/10.1016/j.polymertesting.2010.12.006. URL http://www.sciencedirect.com/science/article/pii/S0142941811000043.

[91] Y.C. Lin, Xiao-Nan Fang, Yu-Qiang Jiang, and Hao Jin. Ultrasonic bond process for polymer-based anisotropic conductive film joints. part 2: Application in chip-on-fr4 board assemblies. *Polymer Testing*, 30(4):449 – 456, 2011. ISSN 0142-9418. doi: https://doi.org/10.1016/j.polymertesting.2011.03.003. URL http://www.sciencedirect.com/science/article/pii/S0142941811000419.

[92] Y. Xiao, Q. Wang, L. Wang, X. Zeng, M. Li, Z. Wang, X. Zhang, and X. Zhu. Ultrasonic soldering of cu alloy using ni-foam/sn composite interlayer. *Ultrasonics Sonochemistry*, 45:223–230, 2018. doi: 10.1016/j.ultsonch.2018.03.005.

[93] Kyung-Soo Kim, Chang-Wan Ha, Tae-Young Jang, Sang Won Joung, and Won-Soo Yun. Using lateral vibration for thermosonic flip-chip interconnection with anisotropic conductive film. *Journal of Micromechanics and Microengineering*, 20(10):105015, sep 2010. doi: 10.1088/0960-1317/20/10/105015. URL https://doi.org/10.1088%2F0960-1317%2F20%2F10%2F105015.

[94] G. Goldberg. Diode laser soldering technology: The next generation in non-contact soldering. *SMT Surface Mount Technology Magazine*, 18(9), 2004. URL https://www.scopus.com/inward/record.uri?eid=2-s2.0-54849434836&partnerID=40&md5=8d5906a5f9f3de6c10e768a34a7d5c21.

[95] Z.-j. HAN, S.-b. XUE, J.-x. WANG, X. ZHANG, L. ZHANG, S.-l. YU, and H. WANG. Mechanical properties of qfp micro-joints soldered with lead-free solders using diode laser soldering technology. *Transactions of Nonferrous Metals Society of China (English Edition)*, 18(4):814–818, 2008. doi: 10.1016/S1003-6326(08)60141-7.

[96] P. Xue, S.-B. Xue, L. Zhang, Y.-F. Shen, L.-L. Gao, S.-L. Yu, H. Zhu, Z. Han, and Y. Chen. Tensile strength of fine pitch qfp lead-free soldered joints with diode laser soldering. *Soldering and Surface Mount Technology*, 23(3):177–183, 2011. doi: 10.1108/09540911111146935.

[97] H. Nishikawa and N. Iwata. Improvement of joint reliability of sn-ag-cu solder bumps on cu by a laser process. *Materials Transactions*, 56(7):1025–1029, 2015. doi: 10.2320/matertrans.MI201421.

[98] H. Nishikawa and R. Matsunobu. Interfacial reaction of sn-ag-cu-ni solder/cu joints by laser process. In *2018 7th Electronic System-Integration Technology Conference (ESTC)*, pages 1–4, Sep. 2018. doi: 10.1109/ESTC.2018.8546406.

[99] Y.H. Tian and C.Q. Wang. 12 - laser soldering. In Y. Zhou, editor, *Microjoining and Nanojoining*, Woodhead Publishing Series in Welding and Other Joining Technologies, pages 299 – 326. Woodhead Publishing, 2008. ISBN 978-1-84569-179-0. doi: https://doi.org/10.1533/9781845694043.2.299. URL http://www.sciencedirect.com/science/article/pii/B9781845691790500128.

[100] Michiel Hazewinkel. *Encyclopaedia of mathematics: an updated and annotated translation of the Soviet "Mathematical encyclopaedia"*. Kluwer Academic Publishers, 1995.